Fundamental Surface Properties of Simple Fatty Acid Model Systems of Sea Spray Aerosols and the Sea Surface Microlayer

Dissertation

Presented in Partial Fulfillment of the Requirements for the Degree Doctor of Philosophy in the Graduate School of The Ohio State University

By

Bethany A. Rudd

Graduate Program in Chemistry

The Ohio State University

2018

Dissertation Committee

Prof. Heather C. Allen, Advisor

Prof. L. Robert Baker

Prof. Terry L. Gustafson

Prof. Andrew A. May

Abstract

Upon wind action on the ocean surface, sea spray aerosols (SSA) are generated and released to the atmosphere. SSA are enriched in the organics and ions present in the sea surface microlayer (SSML) due to the selective transfer of these species to the aerosol phase, and can impact the climate through multiple mechanisms. Aerosols and clouds contribute the largest uncertainty in the prediction of climate change, so an understanding of SSA chemistry is of importance. The organic coatings identified on SSA contain a diverse array of surface-active molecules such as fatty acids. These coatings impact the reactivity, reflectivity, lifetime, and nucleating abilities of the aerosol particles. As these organic films impact the climate-relevant properties of SSA, an understanding of the fundamental physical chemistry phenomena of lipids and ions at these interfaces warrants investigation. In this dissertation, surface sensitive techniques were utilized to probe the structure and properties of fatty acid model systems under various pH and ion conditions.

In the first part of this study, the surface-pK_a values of medium-chain (C_8-C_{10}) fatty acids were quantified through the use of surface tension titration. Our simple surface tension titration technique quantified the surface-pK_a of medium-chain octanoic (C_8), nonanoic (C_9), and decanoic (C_{10}) fatty acids as 4.9, 5.8, and 6.4, respectively. The surface-pK_a determined with surface tension differs from the bulk value obtained during a standard acid-base titration, and differences between surface- and bulk-pK_a are observed starting at chain lengths of nine carbon atoms. In the titration curves of the C_8 and C_9 acids, surface tension minima are observed near the surface-pK_a as a result of the formation of highly

surface active acid-soap complexes. The direction of the titration was shown to affect the measured surface-pK_a of the C_9 system due to differences in Na^+ concentration in the solution at pH values near the pK_a.

Palmitic acid (PA, C_{16}) is one of the most abundant fatty acids observed in SSA and the SSML. In the second part of this study, the effect of protonation state on the surface structure of PA monolayers is evaluated under two pH regimes (in the presence of a 100 mM NaCl background electrolyte) corresponding to monolayers that are fully and 50% protonated. The protonation state, surface structure and stability of the monolayers was measured using infrared reflection-absorption spectroscopy (IRRAS) and surface tension equilibrium spreading pressure (ESP) measurements. Both PA and PA/PA^- monolayers pack in a 2D hexagonal lattice structure, and the deprotonation in the PA/PA^- system causes an elevation in the ESP. Vibrational sum frequency generation (VSFG) spectroscopy and surface potential measurements were used to determine the interfacial water structure and organization at the interface. Both monolayers changed the interfacial water structure, relative to the bare air-water surface, with the PA/PA^- system inducing a greater ordering due to the presence of charged surfactant species.

Of the major cations in seawater, Ca^{2+} has been identified as the most enriched in the aerosol phase. In the final part of this work, the binding of Ca^{2+} to the carboxylic acid headgroup of PA, and the impact such binding has on the stability of PA monolayers, was investigated in both equilibrium and non-equilibrium systems. IRRAS measurements of spread monolayers on aqueous $CaCl_2$ subphases ($10\ \mu M \leq [Ca^{2+}] \leq 300$ mM) reveal ion-induced deprotonation of the PA carboxylic acid headgroup with varying degrees of

hydration. Surface tensiometry was used to determine the thermodynamic ESP of PA on the aqueous $CaCl_2$ subphases. Up to concentrations of 1 mM Ca^{2+}, each system reached equilibrium, and Ca^{2+}:PA surface complexation gave rise to lower energy states revealed by elevated surface pressures relative to water. However, PA films are not thermodynamically stable at marine aerosol-relevant Ca^{2+} concentrations ($[Ca^{2+}] \geq 10$ mM). Non-equilibrium relaxation (NER) experiments were conducted and monitored by Brewster angle microscopy (BAM) to determine the effect of the Ca^{2+} ions on PA stability. At high surface pressures, the relaxation mechanisms of PA varied among the systems and were dependent on Ca^{2+} concentration in the subphase. Differences in ESP and NER trends reveal the intricacies in evaluating monolayer stability from thermodynamic and non-equilibrium measurements.

In recent years, climate models have advanced to include the properties of insoluble surfactants within their descriptions of SSA, which at one time were modelled simply as sea salt particles. As the reactivity and climate-relevant properties of SSA are partially dictated by the charge, surface activity and stability of these organics at the aerosol-atmosphere interface, the findings presented here, though evaluated for simple fatty acid model systems, have great impact on the understanding of complex atmospheric interfaces and will lead to better predictions of the effects of surface structure and composition on aerosol climate impacts.

Dedication

This dissertation is dedicated to my parents.

Acknowledgments

First, and foremost, I would like to thank my advisor, Dr. Heather Allen, for her mentorship and guidance through my graduate career at Ohio State. The opportunities provided to me through research in her lab have been invaluable. She has always believed in my potential and encouraged my best work every day. I would also like to thank my other mentors, particularly Dr. Terry Gustafson, Dr. Anne McCoy, and my collaborators in CAICE, who have helped me to grow as a scientist, and more importantly as a person, over the course of my undergraduate and graduate careers. I am greatly appreciative of my team of undergraduate researchers, Evan Lach and Andrew Vidalis, who assisted me in data collection for the various projects in this dissertation. I would also like to acknowledge past and present colleagues in the Allen lab, particularly Dr. Dominique Verreault and Dr. Ellen Adams, for their collaboration and assistance. Finally, I would like to extend my endless appreciation to my husband, family, and friends for their patience, support, kindness, and love throughout this process.

Vita

2013……..	B.S. Chemistry, The Ohio State University, Columbus, OH
2013-present…….....	Graduate Teaching Assistant, Department of Chemistry & Biochemistry, The Ohio State University, Columbus, OH
2014-present…….	Graduate Research Assistant, Department of Chemistry & Biochemistry, The Ohio State University, Columbus, OH

Publications

- B. A. Wellen Rudd, A. S. Vidalis, H.C. Allen; Thermodynamic versus Non-Equilibrium Stability of Palmitic Acid Monolayers in Calcium-Enriched Sea Spray Aerosol Proxy Systems, *Phys. Chem. Chem. Phys*., **2018**, DOI: 10.1039/C8CP01188E.
- S. K. Reddy, R. Thiraux, B. A. Wellen Rudd, L. Lin, T. Adel, F. M. Geiger, H. C. Allen, A. Morita, F. Paesani; Bulk Contributions Modulate the Sum-Frequency Generation Spectra of Interfacial Water of Model Sea-Spray Aerosols, *Chem.,* **2018** [submitted]

- B. A. Wellen, E. A. Lach, H. C. Allen; Surface pK_a of Octanoic, Nonanoic, and Decanoic Fatty Acids at the Air-Water Interface: Applications to Atmospheric Aerosol Chemistry, *Phys. Chem. Chem. Phys*., **2017**, 19, 26551-26558. [Inside Cover, "Hot Article"]
- E. M. Adams, B. A. Wellen, R. Thiraux, S. K. Reddy, A. S. Vidalis, F. Paesani, H. C. Allen; Sodium-Carboxylate Contact Ion Pair Formation Induces Stabilization of Palmitic Acid Monolayers at High pH, *Phys. Chem. Chem. Phys*., **2017**, 19, 10481-10490.
- A. S. Petit, B. A. Wellen, A. B. McCoy; Using Fixed-Node Diffusion Monte Carlo to Investigate the Effects of Rotation-Vibration Coupling in Highly Fluxional Asymmetric Top Molecules: Application to H_2D^+, *J. Chem. Phys*., **2013** 138, 034105.
- A. S. Petit, B. A. Wellen, A. B. McCoy; Unraveling Rotation-Vibration Mixing in Highly Fluxional Molecules Using Diffusion Monte Carlo: Applications to H_3^+ and H_3O^+, *J. Chem. Phys.*, **2012**, 136, 074101.

Fields of Study

Major Field: Chemistry

Table of Contents

List of Figures

List of Tables

List of Abbreviations

SSA	Sea spray aerosols
SSML	Sea surface microlayer
CAICE	Center for Aerosol Impacts on Chemistry of the Environment
PA	Palmitic acid
CCN	Cloud condensation nuclei
INP	Ice nucleating particle
EF	Enrichment factor
ESP	Equilibrium spreading pressure
NER	Non-equilibrium relaxation
BAM	Brewster angle microscopy
IRRAS	Infrared reflection-absorption spectroscopy
VSFG	Vibrational sum frequency generation
MMA	Mean molecular area
RA	Reflectance-absorbance
CMC	Critical micelle concentration
SRH	Separation relative humidity
PA^-	Palmitate
d_{31}-PA	Deuterated palmitic acid
SDS	Sodium dodecyl sulfate
CTAB	Cetyltrimethylammonium bromide
ΔV	Surface potential
DPPA	Dipalmitoyl phosphatidic acid

Chapter 1: Introduction

1.1 Motivation

The studies in this dissertation were conducted to gain insight into the fundamental physical chemistry of atmospherically relevant interfaces. Here, the interfaces of primary interest are those of sea spray aerosols (SSA) and the sea surface microlayer (SSML), where lipids and ions are prevalent at high concentrations. Through the work presented here, a further understanding of surface ionization state, ion-carboxylate interactions, and monolayer stability has been gained for simple SSA and SSML model systems.

This work is motivated and supported through the Center for Aerosol Impacts on Chemistry of the Environment (CAICE), an NSF Center for Chemical Innovation. The goal of this collaborative center is to be able to understand, interpret, and predict the complex chemistry of SSA; from stages of aerosol production, to reactivity in the atmosphere, to the eventual formation of ice and clouds via nucleation of aerosol particles. Through analysis of SSA production, the molecules and ions transferred from bulk seawater and the SSML to the aerosol phase can be quantified. From here, fundamental physical chemistry can be investigated from the systematic analysis of proxy systems modelled after the composition of complex SSA. These results, like those presented in this dissertation, can be used to interpret the enrichment of these molecules and ions in the aerosol phase. Additionally, model systems of SSA can be further studied to understand the impact that chemically

complex aerosol particles have on environmental processes (i.e. cloud and ice nucleation, multiphase reactivity).

1.2 SSA Production, Composition, and Environmental Impact

Aerosols and clouds constitute the largest uncertainty in the prediction of global climate change.[1] As a large fraction of the Earth (approximately 71%) is covered by water, marine sources contribute largely to the population of naturally produced aerosols.[2] On all of these water surfaces exists the sea surface microlayer. The SSML is the region at the surface of all ocean waters that is in direct contact with the atmosphere; its precise thickness and depth is a matter of debate, ~50-400 μm.[3-5] This layer is characterized by its relatively high concentration of organic material relative to bulk seawater (i.e. fatty acids, proteins, sterols, alcohols, phospholipids, etc.).[6,7] The presence of these materials at the air-sea interface is due to the cellular degradation of living organisms like phytoplankton, and can vary with biological activity.[3] By wind action on the ocean surface, SSA are generated from the SSML and released to the atmosphere.[8]

The size and composition of SSA vary by their production method,[9,10] and upon their generation, molecules and ions from the SSML are selectively transferred to the aerosol phase.[11] The bubble-bursting process produces two chemically distinct types of aerosol (film drops and jet drops).[9] Film drops are produced from the bursting of the thin water film at the bubble-atmosphere interface, and are smaller and contain a larger organic fraction than jet drops.[12] Jet drops are generated from the collapse of the bubble cavity after the bubble burst. The general composition of organic-enriched SSA can be described as an inverted micelle, where an aqueous core is surrounded by a layer of surfactants; the

hydrophobic portions of the surfactant molecules are oriented toward the atmosphere, and the hydrophilic polar headgroups are anchored in the aqueous phase.[13]

Fatty acids have widely been identified in this organic fraction of SSA. Of these fatty acids, those with chain lengths of sixteen and eighteen carbons are the most abundant.[12,14,15] Biological activity (i.e. high/low phytoplankton/bacteria) has been shown to influence the fatty acid composition in SSA.[16] Fatty acid composition also exhibits a dependence on aerosol size, with more diverse populations observed in smaller aerosol sizes (diameter < 2.5 μm), including more significant fractions of medium-chain (C_8-C_{10}) acids.[12] The studies presented here focus primarily on palmitic acid (C_{16}, PA) monolayers, but also explore the nature of semi-soluble C_8-C_{10} acids at the interface.

Organic films at the surface of SSA have been shown to impact the chemical and physical properties of the aerosol particles.[17,18] These molecules can participate in, or prevent, the reaction of gas phase species with the molecules present in the aqueous core of SSA.[19-21] Additionally, through changes in surface tension and surface activity, molecules at the interface will alter the hygroscopicity (ability to uptake water) and phase state[22] of SSA thus impacting their ability to act as cloud condensation nuclei (CCN).[23] Interestingly, the impact of SSA surface films on water uptake is debated in the literature.[24-26] The presence of molecules at the interface can also affect the ability of the aerosol to act as an efficient ice nucleating particle (INP), depending on the identity and packing structure of the interfacial species.[27,28] Therefore, in-depth studies of the fundamental surface chemistry of film-forming molecules is important to further understand the complex chemistry and environmental impacts of SSA.

The surface activity of fatty acids, especially those with shorter hydrocarbon chains, will be largely influenced by pH as deprotonated fatty acids can solubilize into the bulk. Upon release from the ocean surface, SSA should have a pH close to that of seawater (pH ~ 8.1).[29] This pH will eventually decrease upon aging in the atmosphere.[30-32] As a result, the ionization state of the fatty acid constituents of the SSA organic film will be affected, leading to more protonated (surface active) species. In this dissertation, changes in the interfacial structure of PA monolayers as a function of pH, and the surface-pK_a values of medium-chain C_8-C_{10} fatty acids at the interface are evaluated and quantified. Such investigations lead to better understanding of the dynamic aerosol interface.

Of the major cations in seawater (Na^+, Mg^{2+}, Ca^{2+}, K^+), Ca^{2+} has been found to be the most enriched in fine SSA.[33,34] In this context, enrichment is defined as the concentration of the species in the aerosol phase relative to bulk seawater, normalized to Na^+ concentration (eqn. (1.1)).[33]

$$EF_{x(SSA)} = \frac{[x]_{SSA} / [Na^+]_{SSA}}{[x]_{seawater} / [Na^+]_{seawater}} \quad (1.1)$$

In the aerosol phase, the enrichment factor (EF) of Ca^{2+} increases with decreasing aerosol diameter.[34] The mechanism of such enrichment is still debated as it is not agreed upon whether organic complexation of the ion to SSML-prevalent lipids is responsible for the efficient transfer of calcium to the aerosol phase.[10,33,34] The binding mechanism of Ca^{2+} to carboxylic acid headgroups of PA monolayers is explored in this dissertation.

One particular focus of this dissertation is that of the stability of model monolayers at the interface. As organic films on SSA have been demonstrated to affect their climate-

relevant properties, an understanding of the time-dependent stability of the films is necessary. Monolayers can be evaluated in terms of their stability at the interface under both equilibrium and non-equilibrium conditions. The determination of the equilibrium spreading pressure (ESP) of a monolayer provides insight to the thermodynamic equilibrium of the surfactant molecules at the interface. In these experiments, an excess of 3D lipid material is deposited onto the aqueous surface and a monolayer is allowed to spontaneously form at the interface. As the molecules elute into the 2D space of the interface, the surface pressure of the system increases and, if thermodynamic equilibrium is attained, the surface pressure of the system no longer changes. This is the point at which there exists a thermodynamic equilibrium between the 2D monolayer and the 3D bulk state of the lipid.[35]

An additional measure of monolayer stability involves the compression of a spread monolayer to a target surface pressure followed by a mechanical maintenance of that surface pressure through motion of compression barriers in a Langmuir trough. In these studies, the change in molecular area as a function of time is evaluated to determine non-equilibrium relaxation (NER) mechanisms. The three most common NER mechanisms are structural rearrangement, the desorption of molecules from the interface into the bulk, and the transformation of 2D monolayer material into 3D collapse-type structures at the surface.[36] The measurement of ESP and NER in monolayer systems provides insight into the stability of the organic films of SSA under various atmospheric conditions.

1.3 Dissertation Highlights

Chapter 2 of this dissertation provides a summary of the techniques and instrumentation utilized to conduct surface-sensitive measurements. These include surface tensiometry methods, Brewster angle microscopy (BAM), infrared reflection-absorption spectroscopy (IRRAS), and vibrational sum frequency generation (VSFG) spectroscopy.

Chapter 3 reports on the work conducted to determine the surface-pK_a of medium-chain (C_8-C_{10}) fatty acids with surface tension titration. It was found that surface-pK_a increases with chain length due to increased van der Waals interactions between hydrophobic surfactant tails. Deviations in the surface-pK_a from the bulk pK_a value began at chain lengths of nine carbons. In the C_8 and C_9 fatty acid systems, surface tension minima were observed in the titration curves near the surface-pK_a indicating the presence of highly surface active acid-soap complexes. The direction of the titration was also shown to affect the measured surface-pK_a.

Chapter 4 takes another approach to investigating fatty acids at various ionization states. Here, the interfacial properties of palmitic acid are evaluated as a function of protonation state (100% and 50%). We investigate the protonation state, packing structure, and equilibrium stability of these monolayers with IRRAS and surface tensiometry. The interfacial water structure associated with these monolayers was evaluated with surface potential measurements and VSFG spectroscopy in the OH stretching region. Some insights into Fresnel factor corrections to the VSFG data are also presented. Appendix A outlines the calculation of Fresnel factors in detail for both OH and CH stretching regions for the analysis of VSFG spectra.

In Chapter 5, a thorough analysis of thermodynamic and non-equilibrium stability of PA monolayers on aqueous calcium chloride subphases is presented. Thermodynamic (ESP) and non-equilibrium relaxation measurements reveal differing stability phenomena with Ca^{2+} concentration. It is shown that at high Ca^{2+} concentrations, PA monolayers do not achieve thermodynamic equilibrium, but exhibit high stability against area loss in NER measurements. BAM, IRRAS, and VSFG are used to characterize the PA monolayer films during a variety of measurements to understand relaxation phenomena at the interface.

Chapter 5 also evaluates the binding signatures of Ca^{2+} ions to the carboxylic acid headgroup of PA under a range of Ca^{2+} concentrations in the aqueous subphase. D_2O subphases can be used to remove the water bending mode in IRRAS spectra at ~1650 cm^{-1} to provide more clear insight into the vibrational spectrum of the CO_2^- modes of PA at the interface. In Appendix B, a discussion is provided on the use of D_2O in surface spectroscopies as well as the results obtained for IRRAS measurements of PA monolayers on 300 mM $CaCl_2$, $MgCl_2$, and $ZnCl_2$ D_2O subphases, which reveal differences in the binding motifs of the ions to the carboxylate group. Finally, chapter 6 summarizes the findings presented in this dissertation as well as the implications this work has for the field of atmospheric chemistry.

Chapter 2: Theoretical Background and Instrumentation

In this chapter, a brief overview of the theory and instrumentation of the techniques used in this dissertation is presented. These techniques include surface tensiometry, BAM, IRRAS, and VSFG spectroscopy.

2.1 Surface Tensiometry Theory

Full derivations of the equations relating to surface tension have been presented elsewhere, so only a brief introduction will be presented here.[37-39] The air-water interface can be expressed, simply, as a three phase system composed of two bulk phases (vapor (v) and liquid (l)), and a surface phase. The change in the internal energy (U) of a two-phase system, ignoring non-expansion work, can be expressed as

$$dU = TdS - PdV + \sum \mu_i dN_i + \gamma dA. \tag{2.1}$$

Knowing that the Gibbs free energy is defined as $G = U + PV - TS$, we can express the change in the total Gibbs free energy of the interfacial system as

$$dG = -SdT + V^v dP^v + V^l dP^l + \sum \mu_i dN_i + \gamma dA. \tag{2.2}$$

For a planar interface, when temperature (T), pressure (P, where $P^v = P^l$), and the number of molecules (N_i) are constant, the surface tension (γ) is defined as

$$\gamma \equiv \left.\frac{\partial G}{\partial A}\right|_{T,P,N_i}. \tag{2.3}$$

2.2 Surface Tensiometry Instrumentation

The following sections outline the specific surface tension instrumentation and techniques utilized throughout the projects composing this dissertation. For all methods, the Wilhelmy plate technique was used to measure surface tension.

2.2.1 Wilhelmy Plate Method

This technique involves measuring the forces acting on a small plate suspended at the surface of a liquid sample. Materials commonly used for these plates are roughened platinum or filter paper.[39] Filter paper plates are disposed of after each individual use, and platinum plates are cleaned by heating in a flame until glowing red to remove organic contaminants from the surface. Regardless of the material, one must ensure complete wetting of the plate such that the contact angle between the liquid and the plate is 0 degrees.[40] The forces acting are the plate are a sum of the forces due to gravity, buoyancy, and the force from the surface itself (i.e. surface tension). Surface tension is calculated from these forces by[38,41]

$$\gamma = \frac{F}{2(L+d)\cos\theta} \tag{2.4}$$

where F is the total force, L is the length of the Wilhelmy plate, d is the plate thickness, and θ is the contact angle. When the two assumptions are made that 1) $\theta = 0$ (i.e. the plate is completely wetted), and 2) the plate is assumed to be infinitely thin ($d \rightarrow 0$), this expression can be simplified to

$$\gamma = \frac{F}{2L} = \frac{g(m_s - m_p)}{2L} \tag{2.5}$$

where g is gravity, m_p is the mass of the plate, and m_s is the mass associated with the surface force.

2.2.2 Surface Tension Titration

One application of the Wilhelmy plate technique, new to use in our laboratory, is hereafter referred to as the surface tension titration. This application was utilized to determine the surface-pK_a of short-chain fatty acids at the air-water interface (Chapter 3).[42] For these experiments, a single aliquot (50 mL) of 1 mM fatty acid solution was added to an empty, large glass Petri dish. The starting solution either had a pH of 12 or 2, depending on the direction of the titration. The titrant, 0.10 M HCl or 0.10 M NaOH, was added to the solution via a 25-mL buret and mixed into the solution with a magnetic stir bar, and surface tension is measured and recorded when stable (± 2 mg). The pH of the solution was also recorded by a pH probe (Accumet AB15 pH meter, Fisher Scientific) immersed in the solution throughout the titration. As the height of the Wilhelmy plate in contact with the solution should remain constant, the Wilhelmy plate height was manually adjusted with the addition of large amounts of titrant. This adjustment was usually at the beginning of the experiment when surface tension, and pH, remained relatively constant with titrant addition. Once surface tension began to decrease, only small amounts of titrant were necessary for pH and surface tension changes, and the change in solution height was negligible. A schematic of the surface tension titration setup is shown in Fig. 2.1.

2.2.3 Langmuir Trough Compression, Non-Equilibrium Monolayer Relaxation, and Equilibrium Spreading Pressure Measurements

The surface tension-related properties of insoluble monolayers are commonly studied with Langmuir troughs. Langmuir troughs use moveable barriers to change the available two-dimensional surface area. In standard surface pressure-area isotherms, where surface pressure is defined as the difference in surface tension between the bare aqueous interface (γ_0) and the monolayer-covered surface (γ_m),

$$\Pi = \gamma_0 - \gamma_m \tag{2.6a}$$

changes in surface pressure are evaluated from a decrease in the mean molecular area (MMA) of the amphiphiles at the surface. However, it is very important to note that in a compression isotherm, the measured surface pressure is actually the sum of two components. The first is the surface tension difference between the bare and monolayer-covered surfaces (eqn. (2.6a)). The second contribution is that of a two-dimensional compression force which forces the interfacial molecules together.[35]

$$\Pi = (\gamma_0 - \gamma_m) + F_{2Dcomp} \tag{2.6b}$$

Above the monolayer stability limit, one must consider a compression isotherm to be the result of metastable states due to this forcing.

The work presented here utilizes the Langmuir trough (KSV MiniMicro, Biolin Scientific, 145 cm^2 area) to evaluate monolayer stability. In mechanically-controlled, NER experiments, the monolayer is compressed to a target surface pressure at a constant rate of 5 mm/min/barrier. Once that surface pressure is achieved, it is maintained by motion of the barriers at a maximum rate forward/backward of 1 mm/min/barrier. Analysis of the change

in MMA under these conditions allows one to determine the relaxation mechanism of the monolayer. Monolayer relaxation can also be tracked with changes in surface pressure at constant MMA, but these experiments are more difficult to interpret.

ESP experiments are conducted by measuring the time evolution of surface pressure from spontaneously formed monolayers.[43-46] Langmuir troughs were used for these studies so that the surface could be swept to check for contamination prior to surfactant addition. For ESP, as well as all other Langmuir trough measurements, the barriers are quickly compressed, as one monitors the surface pressure of the surface, prior to the start of the experiment. If a Π value greater than 0.20 mN/m is obtained during compression, the surface is aspirated to remove any surface-active contaminants. Once the surface is deemed clean, in ESP measurements, solid crystals of lipid material (~1-3 mg) are added to the surface with a microspatula. Once molecules elute from the crystal face, a monolayer is spontaneously formed. ESP, by our definition, is achieved when the change in surface pressure is $\leq$ 0.10 mN/m over the course of 15 minutes. At this surface pressure, there exists thermodynamic equilibrium between the 2D monolayer and 3D bulk phases.[35] Because this is an equilibrium process, the surface pressure measured is only dependent on the difference in surface tension of the bare and monolayer-covered surfaces (eqn. (2.6a)). While not the case for the studies presented here, if the bulk phase of the lipid is liquid (oleic acid for example), then pure droplets of the liquid would be added to the surface to create a visible lens for ESP measurements.

2.3 Brewster Angle Microscopy Theory

BAM is a non-invasive imaging technique which can reveal the surface morphology of lipid-covered interfaces. This technique relies on the minimal reflectance of *p*-polarized light at the Brewster angle (θ_B) of the bare surface.[38] Water, for example, has a Brewster angle of approximately 53.1°, relative to the surface normal. One can calculate θ_B through the use of the equations for reflectance. In a simplified system of two media, reflectance (R) can be defined, for *s*- and *p*-polarizations, as the ratio of the reflected and incident beam intensities (I_r and I_i, respectively) and can be calculated from the Fresnel reflection coefficients as a function of the incident angle (θ_i) and refracted angle (θ_t), as shown below.[41,47,48]

$$R = \frac{I_r}{I_i} = |r|^2 \tag{2.7}$$

$$r_s = \frac{\sin(\theta_i - \theta_t)}{\sin(\theta_i + \theta_t)} \tag{2.8}$$

$$r_p = \frac{\tan(\theta_i - \theta_t)}{\tan(\theta_i + \theta_t)} \tag{2.9}$$

From eqn. (2.9), r_p approaches zero when the denominator approaches infinity. This occurs when $\theta_i + \theta_t = \frac{\pi}{2}$. Using Snell's law,

$$n_1 \sin\theta_i = n_2 \sin\theta_t \tag{2.10}$$

the incident and refracted angles are related to the refractive indices of the media, where n_1 and n_2 are the refractive indices of the air and subphase, respectively. In the case of no reflection, $\theta_i = \theta_B$, and $\theta_t = \frac{\pi}{2} - \theta_B$, the Brewster angle can be determined to be

$$\theta_B = \tan^{-1}\left(\frac{n_2}{n_1}\right). \quad (2.11)$$

When a Langmuir monolayer is present on the surface, because its refractive index is different than that of the aqueous subphase,[39] *p*-polarized light is reflected from the surface (Fig. 2.2). This creates a contrast between lipid-rich (bright) and lipid-poor (dark) regions in the captured image of the surface. Ideally, on a bare surface, where the change from medium 1 to medium 2 is abrupt, r_p is equal to zero at θ_B, but on a real interface, there still exists a minimal amount of reflected light. Reasons for this remaining reflectance include the finite thickness of the interface, surface roughness, and the optical anisotropy of the interface.[47]

2.4 Brewster Angle Microscopy Instrumentation

The BAM images presented here were collected with a custom-built setup (Fig. 2.3) housed within a black Plexiglas box to minimize outside light and dust interferences. This setup has been described elsewhere, but its components will be outlined here.[49-52] A HeNe laser (Model 30528, Research Electro-Optics) emits linearly-polarized light at a wavelength of 543 nm and at a maximum power of 0.5 mW. The emitted light is attenuated by a half wave plate (Ekspla) and then further filtered by a Glan prism (Ekspla) before impinging the sample surface at the Brewster angle of the subphase (i.e. $\theta_{B,water} \approx 53.1^{\circ}$). The reflected light is collected by a 10x infinity-corrected super-long working distance objective lens (CFI60 TU Plan EPI, Nikon) and then collimated by a tube lens (MXA22018, Nikon) onto a back-illuminated EM-CCD camera (DV887-BV, 512×512 active pixels, 16×16 μm pixel size, Andor). Images were cropped from their original size of 8.2×8.2 mm to show only the most resolved portion.

2.5 Infrared Reflection-Absorption Spectroscopy Theory

IRRAS is a surface-sensitive spectroscopic technique which produces a vibrational spectrum of the interface. In the work presented here, IRRAS is utilized to investigate ion binding to carboxylic acid headgroups, and to determine the two-dimensional packing of Langmuir and Gibbs monolayers at the interface under various pH and salt conditions in the subphase.

IRRAS spectra are plotted in terms of reflectance-absorbance (*RA*), defined as

$$RA = -\log\left(\frac{R}{R_0}\right) \tag{2.12}$$

where R_0 is the reflectance of the bare aqueous solution and R is the reflectance of the monolayer at the interface.[48] For Langmuir monolayers, R_0 is collected prior to lipid deposition at the surface. For Gibbs monolayers, R_0 is collected from a solution free from surfactant material which is aspirated from the sample container (i.e. Petri dish) prior to the collection of the surfactant solution spectrum.

The reflectance observed in the spectra depends partly on the experimental geometry and properties of the media, which one can approximate as a system of three layers, one of which is the thin layer of the surfactant. For the *s*- and *p*-polarizations, the Fresnel reflection coefficients for a three-layer model can be written as[48,53]

$$r_s = -\frac{\sin(\theta_i - \theta_t) - i\frac{2\pi}{\lambda}\tilde{n}_2^{-1}\sin\theta_i\,\tilde{I}_1}{\sin(\theta_i + \theta_t) - i\frac{2\pi}{\lambda}\tilde{n}_2^{-1}\sin\theta_i\,\tilde{I}_1} \tag{2.13}$$

$$r_p = \frac{\sin(\theta_i - \theta_t)\cos(\theta_i + \theta_t) - i\frac{2\pi}{\lambda}\tilde{n}_2^{-1}\sin\theta_i\,(\tilde{I}_1\cos\theta_i\cos\theta_t - \tilde{I}_2\sin\theta_i\sin\theta_t)}{\sin(\theta_i + \theta_t)\cos(\theta_i - \theta_t) - i\frac{2\pi}{\lambda}\tilde{n}_2^{-1}\sin\theta_i\,(\tilde{I}_1\cos\theta_i\cos\theta_t + \tilde{I}_2\sin\theta_i\sin\theta_t)} \quad (2.14)$$

where

$$\tilde{I}_1 = \int (\tilde{n}_x^2(z) - \tilde{n}_2^2)dz \quad (2.15)$$

$$\tilde{I}_2 = \int \frac{(\tilde{n}_z^2(z) - \tilde{n}_2^2)}{\tilde{n}_z^2(z)}dz \quad (2.16)$$

and $\tilde{n}$ is the complex refractive index for the subphase ($\tilde{n}_2$) and the monolayer ($\tilde{n}_x = \tilde{n}_y$ and $\tilde{n}_z$),

$$\tilde{n}_i = n_i + ik_i \quad (2.17)$$

comprised of the real refractive index (n) and the extinction coefficient (k).

As shown by the equations above, the reflectance at the interface will depend on the polarization and angle of the incoming beam, as well as the properties of the media of the system (i.e. refractive index). The effects of such parameters have been discussed in the literature,[54,55] but it is worth noting that in particular, the angle and polarization of the beam will affect whether the absorption bands observed in IRRAS are positive or negative. For *s*-polarized light, at all angles, the absorption bands are negative. However, for *p*-polarized light, bands are negative at angles up to the θ_B, and become positive at angles greater than θ_B.[55,56] For the spectra shown here, unpolarized light was used and, as all angles of incidence are less than θ_B, only negative bands are considered.

2.6 Infrared Reflection-Absorption Spectroscopy Instrumentation

IRRAS spectra were collected using a custom-built setup (Fig. 2.4) housed in an FT-IR Spectrometer (Spectrum 100, Perkin Elmer). The unpolarized IR beam is directed to the sample surface with a 2-inch gold mirror at an angle of incidence of 46° for H_2O aqueous subphases and 45° for D_2O subphases. The reflected beam is directed, with a second gold mirror, to a liquid nitrogen-cooled MCT detector. All spectra are collected in single beam mode and are the result of coaveraging 300 scans at a 4 cm^{-1} resolution.

2.7 Vibrational Sum Frequency Generation Spectroscopy Theory

VSFG is a surface-specific, nonlinear spectroscopic technique that produces a vibrational spectrum of the interface. The technique is inherently surface-specific because it requires a lack of centrosymmetry, and therefore it is forbidden in bulk media.[57] To achieve sum frequency generation, two pulsed laser beams, one a fixed-frequency visible and the other a tunable broadband infrared, are overlapped spatially and temporally to produce a third beam at a frequency which is the sum of the two incoming beams ($\omega_{SFG} = \omega_{vis} + \omega_{IR}$).[58] The intensity of this SFG signal (I_{SFG}) is proportional to the square of the effective second-order nonlinear susceptibility ($\chi^{(2)}_{eff}$), and the intensities of the incident visible and IR beams (I_{vis} and I_{IR}, respectively).[59]

$$I_{SFG} \propto \left|\chi^{(2)}_{eff}\right|^2 I_{vis} I_{IR} \tag{2.18}$$

The $\chi^{(2)}_{eff}$ response is a combination of non-resonant (from electronic transitions) and resonant contributions.[60]

$$\chi_{eff}^{(2)} = \chi_{NR}^{(2)} + \sum_{q} \chi_{q}^{(2)} \tag{2.19}$$

The resonant terms come from the vibrational modes, and are enhanced when the IR frequency is in resonance with a vibrational mode (ω_q) at the interface. Additionally, $\chi_q^{(2)}$ is the macroscopic average of the molecular hyperpolarizabilities ($\beta_q^{(2)}$). The hyperpolarizability is proportional to the product of the Raman and the IR transition moments from ground to excited states, thereby giving rise to one of the SFG selection rules that the vibrational mode must be both IR and Raman active to be observed.[57]

The $\chi_{eff}^{(2)}$ intensity measured in a VSFG experiment is dependent on the experimental geometry (i.e. incident and outgoing angles) and the polarization of the beams (commonly *ssp*, *ppp, sps*, *pss* in the order of SFG, visible, and IR beams).[57] For *ssp* and *ppp* polarizations, used in the work presented in this dissertation, $\chi_{eff}^{(2)}$ can be expressed as the following (eqns. (2.20-2.21)), where L_{ii} are the frequency-dependent nonlinear Fresnel factors and β_i is the incident (visible, IR) or outgoing (SFG) angle of the beams relative to surface normal.[61] More detailed discussion on the calculation of the Fresnel factors can be found in Appendix A.

$$\chi_{eff,ssp}^{(2)} = L_{yy}(\omega_{SFG}) L_{yy}(\omega_{vis}) L_{zz}(\omega_{IR}) \sin\beta_{IR} \chi_{yyz}^{(2)} \tag{2.20}$$

$$\begin{aligned} \chi_{eff,ppp}^{(2)} = & -L_{xx}(\omega_{SFG}) L_{xx}(\omega_{vis}) L_{zz}(\omega_{IR}) \cos\beta_{SFG} \cos\beta_{vis} \sin\beta_{IR} \chi_{xxz}^{(2)} \\ & - L_{xx}(\omega_{SFG}) L_{zz}(\omega_{vis}) L_{xx}(\omega_{IR}) \cos\beta_{SFG} \sin\beta_{vis} \cos\beta_{IR} \chi_{xzx}^{(2)} \\ & + L_{zz}(\omega_{SFG}) L_{xx}(\omega_{vis}) L_{xx}(\omega_{IR}) \sin\beta_{SFG} \cos\beta_{vis} \cos\beta_{IR} \chi_{zxx}^{(2)} \end{aligned} \tag{2.21}$$

$$+ L_{zz}(\omega_{SFG})L_{zz}(\omega_{vis})L_{zz}(\omega_{IR}) \sin\beta_{SFG} \sin\beta_{vis} \sin\beta_{IR} \chi^{(2)}_{zzz}$$

2.8 Vibrational Sum Frequency Generation Spectroscopy Instrumentation

The visible-infrared broadband VSFG system used here has been described previously in the literature, but will be briefly outlined here.[51,62,63] The ~4 W output of a Ti:sapphire regenerative amplifier (Spitfire Ace, Spectra Physics) was split to produce visible and tunable IR beams. To produce the IR beam, half of this output was directed to an optical parametric amplifier (TOPAS-C, Light Conversion) coupled to a non-collinear difference frequency generator (NDFG, Light Conversion). The remaining portion of the amplifier output, used as the visible beam, was directed to an etalon (SLS Optics) to create asymmetric picosecond pulses with a FWHM of 12 cm^{-1}. The IR (68°) and visible (800 nm, 52°) beams were incident in a co-propagating geometry and the reflected sum frequency signal was collected by a spectrometer (Spectra Pro-500i, Princeton Instruments, 1200 grooves/mm grating) and a liquid nitrogen-cooled CCD (Spec-10:400B, 1340×400 pixels, Princeton Instruments). For the CH stretching region, the energy of the IR and visible beams were 15 μJ and 90 μJ, respectively. In the OH region, beams were incident at the same angles as for CH region spectra, and had energies 10 μJ (IR) and 70 μJ (visible). Spectra of monolayer-covered surfaces had an exposure time of 5 minutes. All spectra were background-subtracted and normalized to the non-resonant profile of a z-cut quartz crystal.

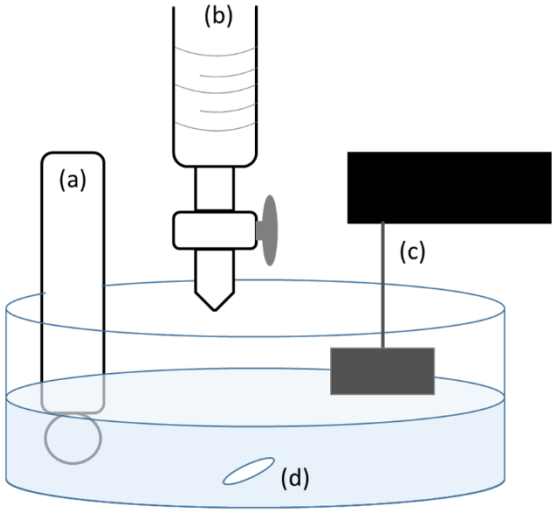

Figure 2.1. Schematic of the surface tension titration setup. (a) pH probe, (b) 25-mL buret, (c) KSV tensiometer head with platinum Wilhelmy plate, and (d) magnetic stir bar. The entire experiment is conducted within the Petri dish which is situated atop a stirring apparatus.

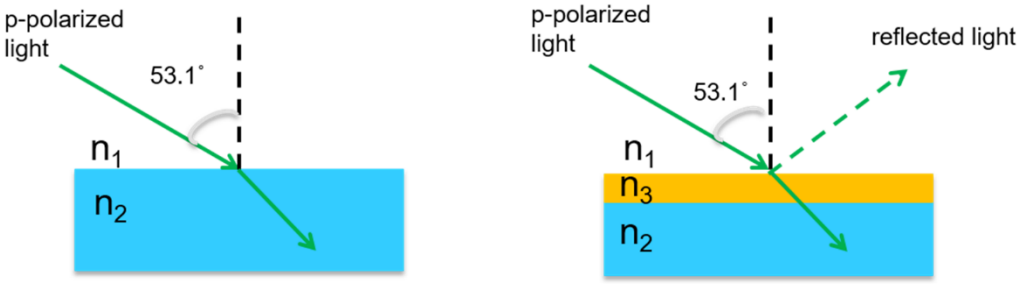

Figure 2.2. Schematic that illustrates the principle of a BAM measurement. At the Brewster angle, *p*-polarized light is not reflected. The presence of a monolayer (represented by the thin layer with refractive index n_3), changes the condition of the interface and *p*-polarized light is reflected.

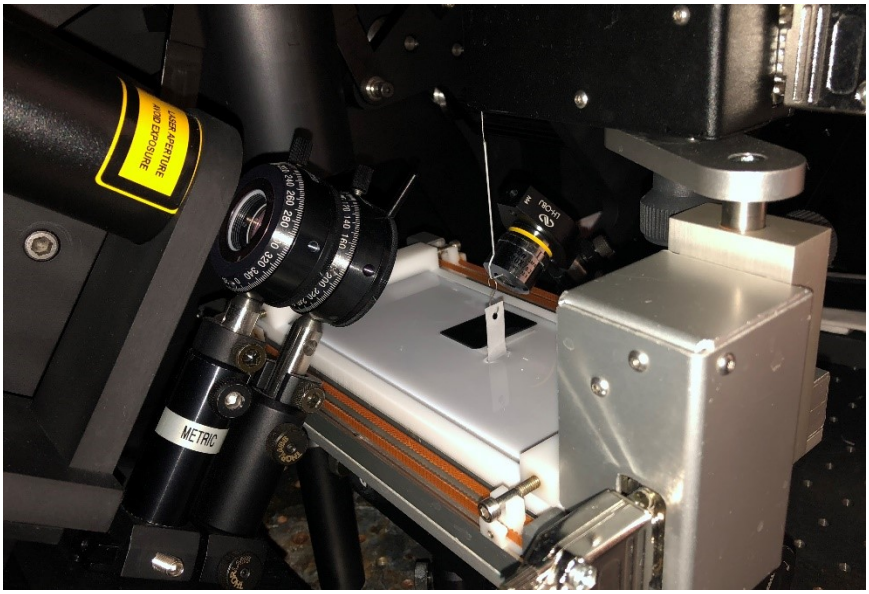

Figure 2.3. The BAM setup consists of (from left to right) a green HeNe laser (543 nm), half-wave plate for attenuation, Glan prism, objective lens, tube lens, and CCD camera for image collection. A black density filter is placed in the Langmuir trough to absorb scattered radiation from the beam. The tube lens and CCD camera are not shown in this image.

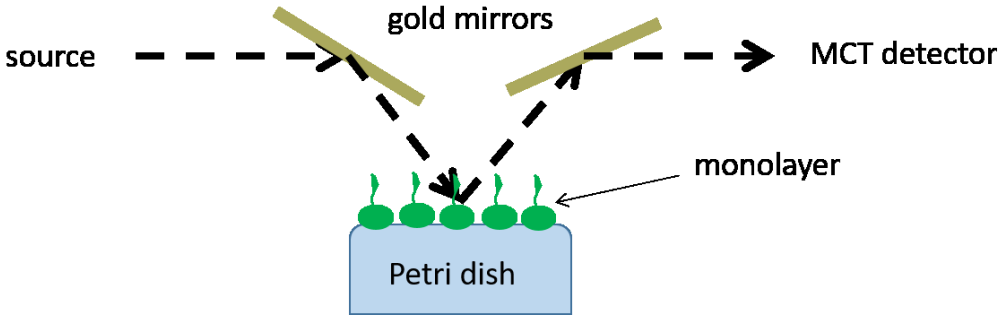

Figure 2.4. Schematic of the IRRAS setup used in this dissertation. The breadboard containing the gold mirrors is situated in a Spectrum 100 Perkin Elmer FTIR spectrometer equipped with an HgCdTe (MCT) detector.

Chapter 3: Surface-pK_a of Octanoic, Nonanoic, and Decanoic Fatty Acids at the Air-Water Interface: Applications to Atmospheric Aerosol Chemistry

Reproduced in part with permission from the PCCP Owner Societies: B. A. Wellen, E. A. Lach, and H. C. Allen "Surface pK_a of octanoic, nonanoic, and decanoic fatty acids at the air-water interface: Applications to atmospheric aerosol chemistry" *Phys. Chem. Chem. Phys.*, 2017, 19, 26551-26558.

3.1 Introduction

The air-water interface provides a unique environment for chemistry due to its asymmetry and 2D intermolecular interactions.[38,64] As the local environment at the interface is different from the bulk, one would expect the pK_a (an expression of acidity) of surface-active molecules to deviate from bulk values. This deviation can be attributed to increased interactions between molecular groups as a result of van der Waals forces between longer hydrocarbon chains,[65] a change in the local pH at the surface due to the charge density of the surface film,[66-68] or a change in the effective dielectric constant of the medium surrounding the headgroups of molecules at the interface.[69-72]

Fatty acids constitute a common class of surface-active molecules which are studied at the air-water interface. Some studies have shown that as the hydrophobic chain length of the acid increases, and the molecules become more surface active, the pK_a also increases.[65,73] However, it has been commonly, and incorrectly, reported in literature that

the pK_a of medium-chained fatty acids (C_8-C_{10}) at the interface is the same as that of their bulk counterpart.[10,74,75] As the surface-pK_a of these medium-chain fatty acids seem ill-defined, one might be inclined to examine the trends of other physical properties (solubility and critical micelle concentration (CMC)) against carbon chain length for these saturated compounds (Fig. 3.1).[76,77] Between two and six carbons, the acids are very soluble (from ∞ to 0.97 g/100 g H_2O) and have higher CMC values (indicating that a large concentration is necessary for the required molecular associations to form micelles). For acids with chain lengths of 12 or more carbon atoms, solubility and CMC remain relatively constant at low values. Between these two regimes lies the class of medium-chain fatty acids, which are on the cusp of being considered in the same context as their insoluble, surface-active ($C_n \geq 12$) counterparts as opposed to predominantly bulk species ($C_n \leq 6$).

While fatty acids have implications in many fields such as biological membranes,[78-80] mineral flotation,[81,82] and food science,[83-85] of particular interest is aerosol chemistry. Breaking waves at the ocean surface generate and release SSA to the neighboring atmosphere. During this process, the organic molecules enriched in the SSML are transferred to the atmosphere as coatings on SSA. Although C_{16} and C_{18} fatty acids are found to be the most abundant in these organic films,[12,14,15] C_8-C_{10} saturated fatty acids have also been identified in significant concentrations.[12] Moreover, the concentrations of these shorter acids are likely to become more prevalent as the aerosol ages due to the oxidation of longer-chain fatty acids.[86-89]

SSA reactivity,[19-21,90] lifetime,[24,91] light-scattering[92,93] and nucleating abilities[23] are affected by the organic coatings at the aerosol-atmosphere interface. Surface tension is one

of the governing parameters of several of these properties, and can be affected by the pH of the aerosol, and in turn, the surface-pK_a of the molecules at the interface. Upon entering the atmosphere, SSA will be at a pH close to that of the ocean (8.1),[29] and any short- or medium-chain fatty acids have been thought to exist in their deprotonated state, and therefore would have low surface activity. However, upon aging in the atmosphere, reactions with gas phase acidic species (i.e. HCl, HNO_3) will cause these aerosols to become acidified,[31] thus increasing the surface activity of the fatty acids and decreasing the surface tension at the interface. The pH at which this transformation (deprotonated to protonated) occurs is dictated by the surface-pK_a of the species at the interface, and will affect the surface tension-dependent properties of the aerosol. For example, separation relative humidity (SRH) is a metric that can be used to determine the phase state of an aerosol, and is affected by pH and the pK_a of the organic fraction of SSA. The SRH of model SSA particles decreases at high pH as a result of the increased solubility of the organic components.[22] As particle phase state has a large influence on the chemical and physical properties of an aerosol, an understanding of the pH at which the organic components become deprotonated is crucial.[94]

The primary goal of this work is to determine the surface-pK_a of medium-chain fatty acids at the air-water interface, which we expect to differ from their commonly used bulk values (~4.8). We utilize a surface tension titration technique to determine these values, and evaluate our results within the context of similar, yet controversial, studies in the literature.

3.2 Experimental Materials and Methods

3.2.1 Materials

Octanoic acid (C_8, ≥ 99%, M_w 144.21 g/mol), nonanoic acid (C_9, ≥ 97%, M_w 158.24 g/mol), and decanoic acid (C_{10}, ≥ 98%, M_w 172.26 g/mol) were purchased from Sigma Aldrich and used without further purification. HCl (Trace Metal Grade) was purchased from Fisher Scientific, and NaOH pellets (99%) were purchased from Mallinckrodt. A Barnstead Nanopure filtration system (D4741, Thermolyne Corporation) with additional cartridges to remove organic material (D5026 Type I ORGANIC-free Cartridge Kit, Pretreat Feed) provided ultrapure water with a resistivity of at least 18.0 MΩ•cm. Solutions of the C_8-C_{10} acids were prepared at concentrations of 1 mM at pH 12 for surface tension (γ) versus pH titrations with a 0.10 M HCl titrant. The C_9 system was also prepared at 1 mM in a pH 2 solution for titration with 0.10 M NaOH. 1 mM C_9 solutions were prepared in ultrapure water for standard acid-base titrations with 0.005 M NaOH. All experiments were conducted at 21 ± 1 °C and at a measured relative humidity of 43 ± 2%.

3.2.2 Methods

Surface Tension Measurements

Surface tension was probed with a platinum Wilhelmy plate and calculated via

$$\gamma = \frac{F}{2L\cos\theta} \tag{3.1}$$

where the force (F) is obtained from the measured difference in mass of the plate, θ is the contact angle between the plate and solution (assumed to be 0°),[40] and $2L$ is the perimeter of the wetted surface (39.24 mm). Readings were obtained with a KSV NIMA (Biolin

Scientific) tensiometer and interface unit equipped with LayerBuilder software. The plate was heated by flame prior to measurements to remove any organic residue from the surface.

Surface Tension Titration

The use of surface tension to determine surface-pK_a was inspired by the work Dickhaus & Priefer and Sugawara *et al*.[95,96] For the C_8-C_{10} acids, surface tension versus pH data was obtained via titration of a 50 mL aliquot of the C_n solution with either acid or base while monitoring γ and pH (Accumet AB15 pH meter, Fisher Scientific). The pH probe was calibrated before the measurements with pH 1, 4, 6, 7, and 10 buffer solutions. The γ measurements were taken continuously as titrant was added to a 1 mM aliquot of fatty acid solution, allowing for the mass reading to stabilize before a measurement was recorded. Stirring was used to ensure efficient mixing of the added titrant. For titrant additions after which the mass reading did not change significantly, a wait time of 2 minutes was allotted prior to recording the surface tension mass reading. Along more dynamic areas of the titration curves, an equilibration time of at least 10 minutes was required for the mass readings to stabilize. A reading was deemed stable when the mass only changed by approximately 2 mg around a central value. Dilution effects[97] on the measured γ of the Gibbs monolayer were minimized with only a ~10% increase in volume from titrant addition. To compensate for the rising height of solution due to the addition of titrant, the plate was periodically raised to maintain a constant depth in solution. The error bars reported are dominated by the uncertainties from the pH meter measurements and the error of the surface tension data fits. Errors reported represent one standard deviation from the average of triplicate measurements.

Infrared Reflection Absorption Spectroscopy

To probe the structure and ordering of the surfactant films at the interface, IRRAS spectra of the C_9 systems were collected using a custom built setup housed in an FTIR spectrometer (Spectrum 100, Perkin Elmer). The setup consists of two gold mirrors. The first mirror directs the incoming IR beam to the sample surface at an incidence angle of 46° relative to surface normal. The second mirror directs the reflected beam to a liquid nitrogen-cooled MCT detector. As IRRAS spectra are plotted in terms of reflectance-absorbance ($RA = -log(R/R_0)$), a background spectrum was collected of a bare pH 2, 5.6 (water), or 12 surface and used as R_0. This background solution was aspirated from the Petri dish and replaced with a 1 mM C_9 solution at the appropriate pH. The spectrum of this solution was used as R. Spectra of the C_9 systems were compared to that of a stearic acid (C_{18}) monolayer. Each spectrum is the result of coaveraging 300 scans over the full range (4000-450 cm^{-1}) at a resolution of 4 cm^{-1}. Spectra shown have been baseline-subtracted by a third order polynomial and are the average of at least 3 individual spectra.

3.3 Results and Discussion

3.3.1 C_n Titration with 0.10 M HCl

To experimentally determine the surface-pK_a of the C_8-C_{10} medium-chain fatty acids, 1 mM solutions were titrated with 0.10 M HCl from a pH of 12 to a pH of 2. Representative surface tension vs. pH titration curves for the three acids are shown in Fig. 3.2. At a pH of 12, the C_n acids are fully deprotonated, and thus relatively surface inactive. The surface tension curves begin at pH 12 and at surface tensions of approximately 70 mN/m, slightly depressed relative to pure water. As 0.10 M HCl is titrated into the

solutions, the surface tension decreases, indicative of the formation of the more surface-active protonated species. The C_8 and C_9 curves develop an interesting feature from pH 6 to 4.5, hereafter referred to as the surface tension dip, where the surface tension decreases to a minimum value then rises to reach a plateau. The physical interpretation of this dip is discussed later.

Upon titration to pH < 4, the surface tension curves approach constant values. The values of surface tension at this point reflect the relative surface activity of each C_n acid. C_{10} approaches a surface tension value of 33.1 ± 0.3 mN/m (the most surface active), followed by C_9 at 34.3 ± 1.6 mN/m, and C_8 at 52.9 ± 2.7 mN/m. The greater surface activity with chain length can be attributed to increasing van der Waals forces between the longer hydrocarbon chains.

3.3.2 The Surface Activity Model

A surface activity mathematical model is applied to the collected surface tension titration data to calculate the surface-pK_a ($pK_{a(s)}$) of the selected C_n fatty acids. This model is adapted from that of Cratin[98] in his work on the interfacial pK_a of stearic acid (C_{18}) at the oil-water interface, and is expressed in terms of the change in surface tension with pH.

If one considers the equilibrium between the protonated (LH) and deprotonated (L^-) forms of a C_n acid at the surface,

$$LH \leftrightarrow L^- + H^+(aq) \tag{3.2}$$

the following expression for the surface equilibrium constant, $K_{a(s)}$, is obtained.

$$K_{a(s)} = \frac{[L^-]_s[H^+]_s}{[LH]_s} \tag{3.3}$$

From the equilibrium, the fraction of protonated (f_{LH}) and deprotonated (f_{L^-}) species can be written as

$$f_{LH} = \frac{[LH]_s}{[L^-]_s + [LH]_s} \tag{3.4a}$$

$$f_{L^-} = \frac{[L^-]_s}{[L^-]_s + [LH]_s} \tag{3.4b}$$

and rearranged to be expressed in terms of $K_{a(s)}$ and $[H^+]_s$.

$$f_{LH} = \frac{1}{1 + K_{a(s)}[H^+]_s^{-1}} \tag{3.5a}$$

$$f_{L^-} = \frac{K_{a(s)}[H^+]_s^{-1}}{1 + K_{a(s)}[H^+]_s^{-1}} \tag{3.5b}$$

Or, using the mathematical definitions of pH and pK_a, eqns. (3.5a) and (3.5b) can be rewritten as

$$f_{LH} = \frac{1}{1 + 10^{(pH_s - pK_{a(s)})}} \tag{3.6a}$$

$$f_{L^-} = \frac{10^{(pH_s - pK_{a(s)})}}{1 + 10^{(pH_s - pK_{a(s)})}} \tag{3.6b}$$

It is important to note that in order to apply Cratin's surface activity model[98] (originally developed to describe stearic acid dissociation at the oil-water interface where a completely dissociated acid would result in an interfacial tension of ~0 mN/m) to these

systems, a simple difference must be taken within the data such that at high pH, the surface tension is associated with a value of 0 mN/m (Fig. 3.3). As such, the surface tension data collected during the titration is presented as $\Delta\gamma$ against pH, where $\Delta\gamma = \gamma_{max} - \gamma$, and γ_{max} is the surface tension of the C_n system at a pH of 12. The surface activity (a) for these medium-chain fatty acids at the air-water interface is then expressed in terms of the lowering of this surface tension difference relative to a maximum value ($\Delta\gamma_{max}$, obtained at low pH).

$$a = \frac{(\Delta\gamma_{max} - \Delta\gamma)}{\Delta\gamma_{max}} \tag{3.7}$$

One of the bounds of this model is that all species, protonated or deprotonated, must coexist independently with only weak interactions in order to express their total activity as a simple summation. Under this assumption, the total activity (a_t) of the system can be expressed as the sum of the activity and fraction of the protonated and deprotonated species.

$$a_t = \sum_i a_i f_i = a_{L-} f_{L-} + a_{LH} f_{LH} \tag{3.8}$$

Equating eqns. (3.7) and (3.8) yields

$$\frac{(\Delta\gamma_{\max} - \Delta\gamma)}{\Delta\gamma_{\max}} = a_{L-} f_{L-} + a_{LH} f_{LH} \tag{3.9a}$$

From examination of a $\Delta\gamma$ vs. pH plot for these systems, one can deduce that $a_{LH} = 0$, and $a_{L^-} = 1$. Under the two pH regimes indicated in Fig. 3.3, and by using eqn. (3.9a), the

following can be deduced. At low pH, $\Delta\gamma \sim \Delta\gamma_{max}$. At low pH, it is assumed that the majority of the fatty acid molecules exist in their protonated state ($f_{LH} = 1$).

$$0 = a_{L-}(0) + a_{LH}(1) \tag{3.9b}$$

$$a_{LH} = 0$$

The same approach can be taken for the high pH regime where $\Delta\gamma \sim 0$ mN/m, and $f_{LH} = 0$.

$$1 = a_{L-}(1) + a_{LH}(0) \tag{3.9c}$$

$$a_{L-} = 1$$

From this, eqn. (3.9a) can be written as

$$\frac{(\Delta\gamma_{\max} - \Delta\gamma)}{\Delta\gamma_{\max}} = f_{\mathrm{L}^-} \tag{3.10}$$

which can be arranged and expressed as eqn. (3.11).

$$\Delta\gamma = \Delta\gamma_{\max}(1 - f_{\mathrm{L}^-}) \tag{3.11}$$

Inserting the equation for f_{L^-} from eqn. (3.6b), the above equation can be written in terms of the surface pH (pH_s) and $pK_{a(s)}$ of the system.

$$\Delta\gamma = \Delta\gamma_{\max}\left(1 - \frac{10^{(\mathrm{pH}_s - \mathrm{p}K_{\mathrm{a}(s)})}}{1 + 10^{(\mathrm{pH}_s - \mathrm{p}K_{\mathrm{a}(s)})}}\right) \tag{3.12}$$

Finally, eqn. (3.12) can be simplified to yield

$$\Delta\gamma = \frac{\Delta\gamma_{\max}}{1 + 10^{(\mathrm{pH}_s - \mathrm{p}K_{\mathrm{a}(s)})}} \tag{3.13}$$

If one assumes that pH_s is equal to the bulk pH (pH_b), eqn. (3.13) becomes

$$\Delta\gamma = \frac{\Delta\gamma_{\max}}{1 + 10^{(\mathrm{pH}_b - \mathrm{p}K_{\mathrm{a}(s)})}} \tag{3.14}$$

While charged monolayers at the interface can create an electrical double layer with hydrogen ion concentrations enhanced relative to the bulk, a 1 mM C_9 solution, for example, represents a very loosely packed sub-monolayer system. Fig. 3.4 shows IRRAS spectra of 1 mM C_9 solutions at pH 2, 12, and of samples extracted from the titration experiment at the surface tension dip. No CH stretching modes are observed at pH 12 indicating that the C_9 molecules are not found, above the detection limit, at the interface. CH stretching modes are present for the 1 mM C_9 solution at pH 2 and in the extracted dip region sample. However, the intensities of the modes are very weak, and the CH_2 stretching frequencies are blue shifted compared to more ordered and surface-active monolayer of stearic acid (Fig. 3.5), indicating that the C_9 system is loosely packed and exhibits significant gauche defects. Therefore, the assumption that pH_s is approximately equal to pH_b holds for the calculation of the surface-pK_a of the medium-chain fatty acids.[99]

When this surface activity model is applied to the systems studied here, a trend is observed between the surface-pK_a and chain length. The fits of the data are shown in Fig. 3.6 and the surface-pK_a values of the C_n systems are presented in Table 3.1. As can be seen from the values in Table 3.1, the surface-pK_a of the fatty acid increases with chain length from 4.9 to 6.4. This trend can be understood to be an additional consequence of increased van der Waals forces between fatty acid molecules with longer chains. Greater forces between the hydrophobic groups at the interface result in increased interactions between the carboxylate headgroups, thus making the acidic hydrogen more difficult to remove.[65]

However, the surface-pK_a for the C_8 system (4.9 ± 0.2) is within the range of the accepted value of its bulk pK_a (4.89).[75]

When a 1 mM C_9 system, prepared in water, is titrated with NaOH in a standard weak acid-strong base titration, a bulk pK_a of 4.97 ± 0.05 is determined from the pH at the half-way point, which also is in close agreement with its literature pK_a value of 4.96 (Fig. 3.7).[75] The significant deviation of surface-pK_a from the C_9 bulk value demonstrates that our surface tension titration is actually probing the surface-pK_a at the air-aqueous interface. The surface-pK_a values presented here should be used when discussing surface speciation.

Although the trend observed with chain length is in accordance with accepted trends in the literature,[65,73] the surface-pK_a values obtained via our surface tension titration are lower than those which have been reported for the C_8 and C_{10} acids by Kanicky *et al*.[65] Throughout the literature, there are many values reported for the pK_a of both medium- and long-chain fatty acids, although less have been reported for the former. A summary of these results, in addition to those determined here, are represented in Fig. 3.8. These values have been determined using a variety of techniques, cover a wide range, and are only sometimes specifically designated as the surface-pK_a. Acid-base titration techniques, not including surface tension, were utilized by Kanicky,[65] McLean,[73] and Cistola[70] to determine the pK_a of fatty acids with chain lengths up to eighteen carbons. McLean studied high concentrations of fatty acids to determine "colloidal pK_a," and obtained values that are significantly lower than those obtained by Kanicky, particularly at shorter carbon chain lengths. However, a linear trend of increasing pK_a with chain length is consistent between the works.

Other techniques for determining the protonation state of surface-active fatty acids can also be applied to calculate surface-pK_a. For example, using X-ray photoelectron spectroscopy, Prisle *et al*.[100] found the fraction of 0.03 M decanoic acid in a decanoic acid/decanoate system to be only ~10% at a bulk pH of 7.1. When the Henderson-Hasselbalch equation is applied to the published data, a surface-pK_a value of 6.1 is calculated for their C_{10} system, which agrees well with the value reported here. Monolayer relaxation data and surface potential-area isotherms were used by Aveyard *et al* and Glazer *et al*. to calculate the surface-pK_a of stearic acid as 9.5 and 8.0, respectively.[101,102] Overall, these results suggest inconsistencies in the determination of surface-pK_a between measurement techniques.

The work of Kanicky, McLean, and Prisle also imply that concentration can impact the determination of surface-pK_a, as concentrations of the systems vary amongst the experiments and sometimes are not specified in the literature. Additionally, in those experiments in which acid-base titration is used to determine pK_a, concentration variations between the studies may affect the activity coefficient of the ionized species in such a way that could potentially account for discrepancies in the reported pK_a values.[71,103] It has been shown that upon dilution of medium-chain fatty acid systems, and subsequent extrapolation of the data to an extremely dilute limit, the pK_a of these acids approach a value of approximately 5.0.[104] The 1 mM concentrations used in the experiments presented here lie at the solubility limit for the C_8-C_{10} acids in water.[76] Therefore, the values reported in Table 3.1 represent the upper limit to the surface-pK_a of these systems.

In Fig. 3.6, it can be seen that the surface-pK_a of the C_8 and C_9 systems are near the pH values where the surface tension dips are observed during the titrations. Similar surface tension dip features with oleic acid/sodium oleate systems have been observed elsewhere in the literature, and are important in the field of mineral flotation.[105-107] Surface tension minima were observed at pH values of approximately 9-10 in the various reports, corresponding to the surface-pK_a of oleic acid.[108] This minimum in surface tension is caused by maximum interactions between the acid (RCOOH) and dissociated soap ($RCOO^{--}$) species, resulting in highly surface active acid-soap complexes ($RCOOH:RCOO^-$) at the interface.[104,107,109] The surface tension dip results obtained here for the C_8 and C_9 systems agree with these reports in that the surface tension minima are observed near pH values associated with, but not at, the respective surface-pK_a of the acid systems. From knowledge of the oleic acid systems, we also assume that the cause of the minima in the C_8 and C_9 systems is the presence of $RCOOH:RCOO^-$ complexes at the interface. Interestingly, a dip was not observed for the C_{10} system. It is plausible that in this system, acid-soap complexes exist, but are not necessarily more surface active than the acid alone. It is important to note that the data points along the titration curve that are associated with the surface tension dip for the C_8 and C_9 systems were removed prior to fitting the data with eqn. (3.14). This is due to an assumption within the surface activity model that all species, protonated or deprotonated, exist ideally in solution or at the interface with only weak interactions.[98] As it is assumed that this dip is due to the strong interaction of acid-soap species, the deviation from the fit of the data with eqn. (3.14) is further evidence of the formation of $RCOOH:RCOO^-$ complexes near the surface-pK_a.

3.3.3 C_9 Titration with 0.10 M NaOH

The titration curves obtained in this work are not the result of measuring several solutions made at discrete pH values. Therefore, the impact of the direction of the titration was considered by titrating a 1 mM C_9 solution at pH 2 with 0.10 M NaOH to approach pH 12. A representative titration of this kind is depicted in Fig. 3.9. The fully protonated C_9 solution has a surface tension of 31.4 ± 2.0 mN/m prior to the titration. The similarity between this starting value and the final value around pH 2 of C_9 in Fig. 3.2 supports the claim that dilution of the C_n solutions over the course of the HCl titration has a minimal impact on the overall results. As the solution becomes more basic during the titration, the surface tension rises as the C_9 species become deprotonated and are removed from the interface. At high pH values, the surface tension approaches a value of approximately 69 mN/m, in agreement with the starting point of the titration of C_9 with 0.10 M HCl.

Noticeably absent from Fig. 3.9a is the surface tension dip observed in the C_9 titration curve in Fig. 3.2. As stated previously, this dip in surface tension is due to the formation of $RCOOH:RCOO^-$ complexes near the surface-pK_a. However, as a pH 2 solution of C_9 is titrated with 0.10 M NaOH, the concentration of Na^+ ions in the resulting solution is much greater than the concentration of Na^+ that is diluted in the titration of a pH 12 solution with 0.10 M HCl. For example, the concentration of Na^+ at pH ~5 is roughly double in the titration with 0.10 M NaOH compared to that with 0.10 M HCl, respectively 18.5 ± 0.3 mM and 9.1 ± 0.1 mM. The increase in Na^+ concentration leads to a disruption in the hydrogen bonding network between protonated and deprotonated fatty acids, similar to a recent study of the effect of sodium on palmitic acid monolayers at varying degrees of

deprotonation.[62] This change in bonding environment prevents the complexation, thus eliminating the observed dip.

When eqn. (3.14) is applied to the C_9 titration with 0.10 M NaOH (Fig. 3.9b), a surface-pK_a value of 5.21 ± 0.02 is determined. When compared to the surface-pK_a obtained using the acidic titrant, the results have a ΔpK_a of -0.6. The likely cause for such a change in the surface-pK_a is the higher concentration of Na^+ in solution. While the Gouy-Chapman model[110-112] was not used to calculate the surface-pK_a of these weakly packed (Fig. 3.4,3.5) Gibbs monolayer systems,[99] the Poisson-Boltzmann description of ion distribution at the interface sheds light on the reduced surface-pK_a in the presence of additional Na^+. According to Gouy-Chapman theory, at a given pH, the addition of competing monovalent ions to a system will result in a decreased amount of H^+ ions accumulating at the interface. Therefore, there will be an increased tendency for the acidic groups at the interface to deprotonate.[112] As there is a greater concentration of Na^+ in this direction of titration at pH values near the surface-pK_a, the shift of the surface-pK_a to a lower value is to be expected. This effect of ions on surface-pK_a has been observed elsewhere in the literature. In the work of Aveyard *et al*., the surface-pK_a of stearic acid was found to decrease by 2 pH units upon the addition of 10 mM NaCl[101] (roughly the same amount as the difference between the acidic and basic titrant systems here). By tracking changes in the vibrational modes associated with the hydrogen-bonded carbonyl (C=O) and the deprotonated carboxylate (CO_2^-) headgroup of acid and deprotonated forms, respectively, spectroscopic investigations, utilizing IRRAS and vibrational sum frequency generation (VSFG), have also revealed that ions (Na^+, Ca^{2+}, Mg^{2+}, Zn^{2+}, etc.) can affect the

protonation state of fatty acid monolayers at the air-aqueous interface.[111,113-115] This is, again, due to a reduction in the surface-pK_a as a result of ion affinity for the negative electron density of the carboxylate headgroups at the surface. Therefore, it is important to acknowledge that the concentration of ions in solution will have an effect on the surface-pK_a determined via surface tension titration and other methods.

3.4 Conclusions

We have used surface tension titration to determine the surface-pK_a of C_8-C_{10} medium-chain fatty acids at the air-water interface. The surface tension versus pH data was fit to a surface activity model[98] which determined surface-pK_a values of 4.9 for octanoic acid, 5.8 for nonanoic acid, and 6.4 for decanoic acid. Due to the solubility limit of the acids in water, these values represent the upper limit to the surface-pK_a. The octanoic and nonanoic acid systems exhibited a surface tension dip near the surface-pK_a due to the formation of acid-soap complexes, which have greater surface activity than the pure acid form. Additionally, it was shown that even small amounts of Na^+ can lower the surface-pK_a of the C_9 acid system (5.2), and disrupt the bonding network between acid and soap species. This general result is consistent with the ion-induced deprotonation of various fatty acid systems due to the distribution of ions at a charged interface.[111,113-115] Upon comparison of the results presented here with those currently in the literature,[65,70,73,100] there still exists controversy.

The surface-pK_a of fatty acids deviates significantly from the bulk value of acetic acid starting at a chain length of nine carbon atoms. Moreover, the surface-pK_a of these fatty acids are not equivalent to their values in the bulk, as evidenced by the weak acid-

strong base titration of nonanoic acid which resulted in a bulk pK_a value of 4.97, consistent with what has been reported in the literature.[75] Therefore, the values of the surface-pK_a of the SSA-prevalent soluble fatty acids determined here should be utilized for aerosol reactivity and CCN models to more accurately assign the speciation, and surface activity, of organic components at the surface of SSA.[23,116,117] Such advances in the understanding of the fundamental properties of these interfacial systems will help to improve certainty in the impacts of aerosols on the climate.

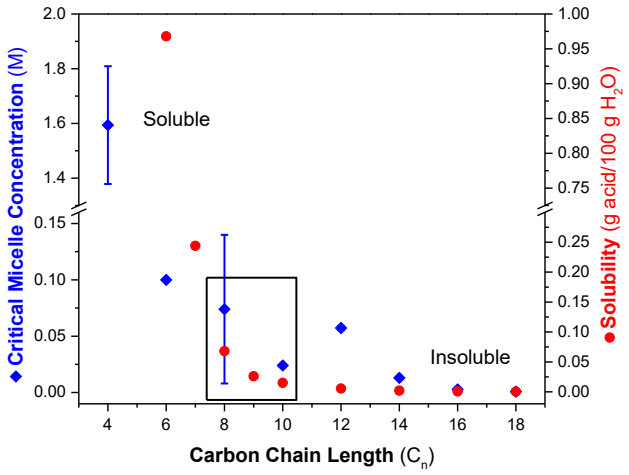

Figure 3.1. Trends of CMC (blue diamonds)[77] and solubility (red circles)[76] with carbon chain length of saturated fatty acids. C_8-C_{10} fatty acids fall between the soluble and insoluble groups of this molecular class.

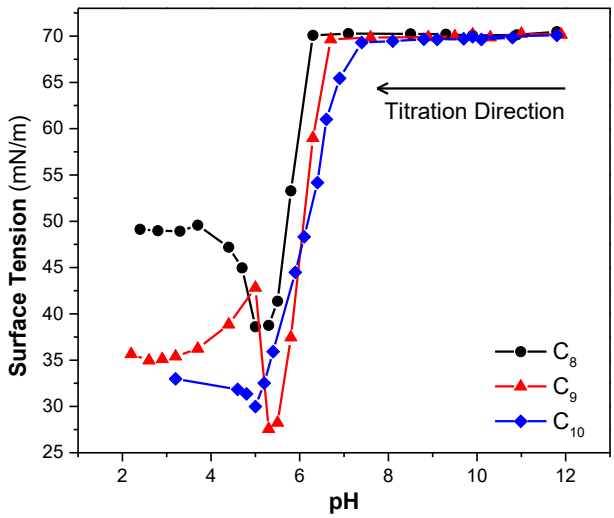

Figure 3.2. Surface tension vs. pH titration curves for 1 mM C_8 (black circles), C_9 (red triangles), and C_{10} (blue diamonds) fatty acid solutions. The titration is conducted from high pH to low pH via the addition of 0.10 M HCl to the 1 mM C_n solutions originally at pH 12. Lines between data points are drawn to guide the eye.

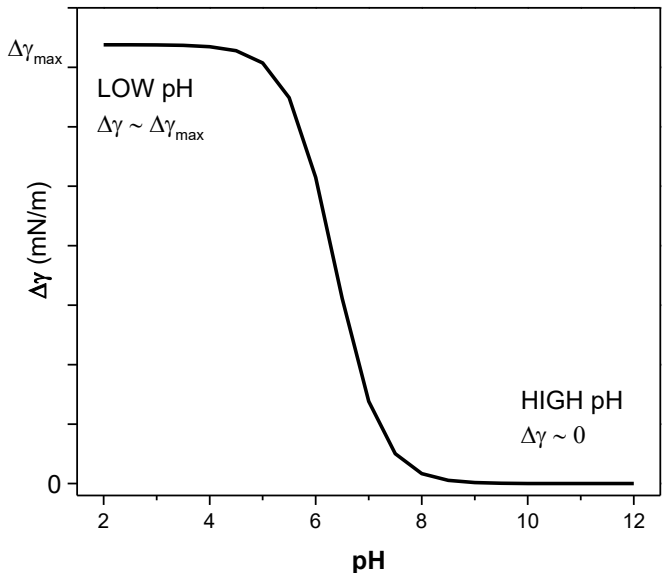

Figure 3.3. Generalized Δγ vs pH curve from the surface activity model.

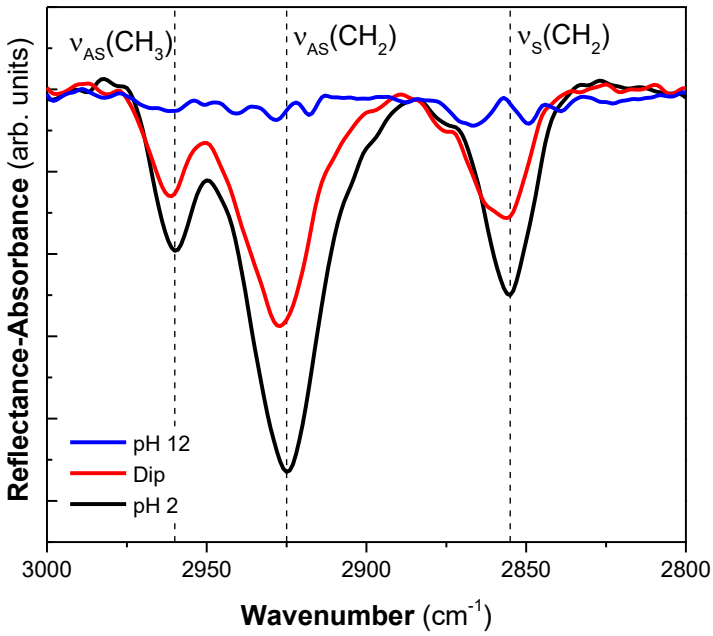

Figure 3.4. IRRAS spectra in the CH stretching region of 1 mM solutions of C_9 at pH 12 (blue, top), solution extracted from the surface tension dip of a titration with 0.10 M HCl (red), and at pH 2 (black).

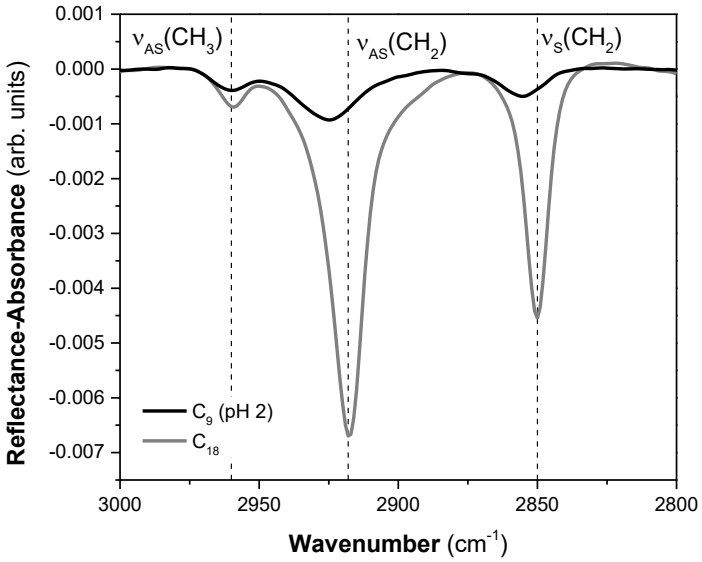

Figure 3.5. IRRAS spectra of 1 mM C_9 at pH 2 compared against a C_{18} monolayer spread to the untilted condensed phase (18.5 $Å^2$/molecule).

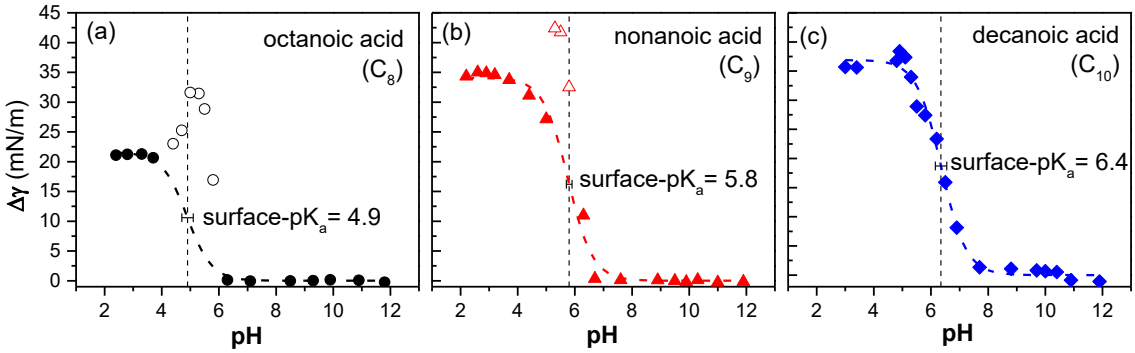

Figure 3.6. The surface activity model (dashed line along data points) applied to C_8 (a), C_9 (b), and C_{10} (c) systems. The vertical dashed line is the average surface-pK_a and includes an error bar of ± one standard deviation based on the calculation of surface-pK_a for three separate trials. Surface tension data has been transformed to $\Delta\gamma = \gamma_{max}-\gamma$.

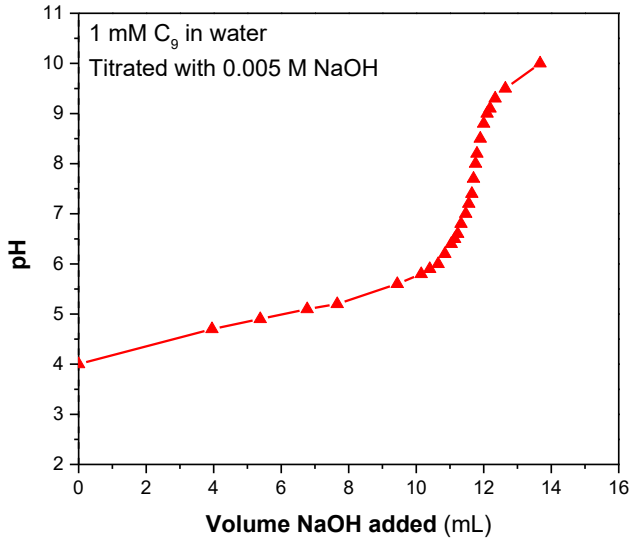

Figure 3.7. Standard bulk weak acid-strong base titration of 1 mM C_9 in water. The pK_a revealed from the pH halfway to the equivalence point is 4.97.

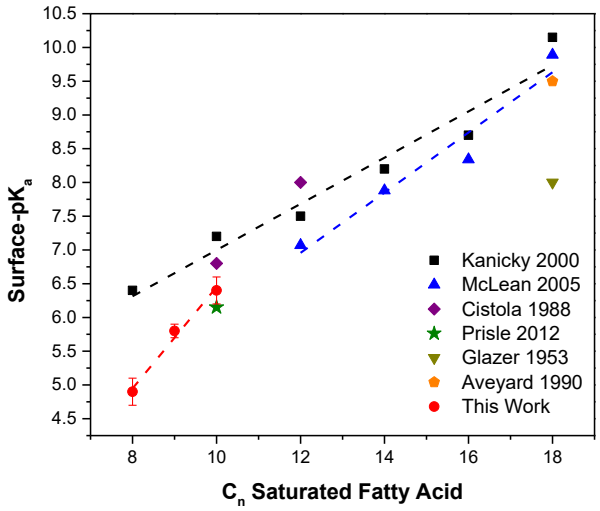

Figure 3.8. Survey of surface-pK_a from the literature.[42,65,70,73,100-102] Dashed lines are drawn to guide the eye.

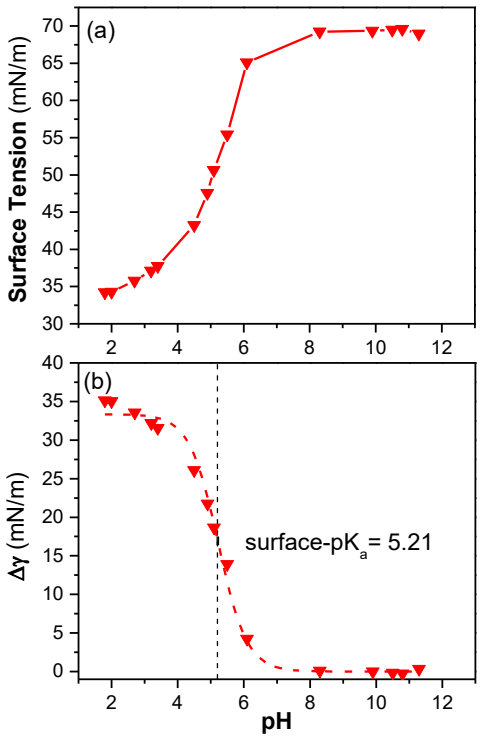

Figure 3.9. Surface tension vs. pH titration curve of 1 mM C_9 solution at pH 2 with 0.10 M NaOH. The solid line in (a) is to guide the eye. The dashed line through the data points in (b) is the curve generated by fitting the data to eqn. (2). The vertical dashed line is the calculated average surface-pK_a.

Table 3.1. Surface-pK_a of C_8-C_{10} fatty acids titrated from pH 12 with 0.10 M HCl.

C_n	Surface-pK_a (p$K_{a(s)}$)
C_8	4.9 ± 0.2
C_9	5.8 ± 0.1
C_{10}	6.4 ± 0.2

Chapter 4: The Effect of Protonation State on the Structure of Palmitic Acid Monolayer Interfaces

Reproduced in part with permission from the PCCP Owner Societies: E. M. Adams, B. A. Wellen, R. Thiraux, S. K. Reddy, A. S. Vidalis, F. Paesani, H. C. Allen "Sodium–carboxylate contact ion pair formation induces stabilization of palmitic acid monolayers at high pH" *Phys. Chem. Chem. Phys.,* 2017, 19, 10481-10490.

4.1 Introduction

Upon release into the atmosphere, SSA likely exhibit a pH close to that of bulk seawater.[29] However, upon aging in the atmosphere, these aerosols will acidify to lower pH values.[30-32] As the organic films on SSA surfaces have demonstrated an influence on the physical and chemical properties of the aerosol (i.e. water uptake, reaction with gas-phase species, surface tension, etc.), understanding how these films respond to changes in pH is of importance. Palmitic acid has been identified as a major component of the organic films on SSA and therefore has been chosen as a simplified model system for this study.[12,14,16] The surface-pK_a of PA lies near that of the ocean pH, at a value of ~8.7. This is the pH at which there exists equal fractions of PA and its dissociated form, palmitate (PA^-). As SSA age in the atmosphere, they will acidify and any PA^- should transform to PA. Of course, this is a simplified view wherein other factors such as ions, complexity in films, etc. are not considered. But, such simple models are necessary to understand the

fundamental physical chemistry of interfaces as researchers continue to build more chemically complex proxy systems to study real SSA.

In addition to the properties of the molecules within the organic films at the surface (i.e. ionization state, packing, stability), the structure of the underlying interfacial water is also of interest in the physical chemistry community. When in the presence of a charged, or neutral, surfactant film, water will reorient at the interface.[118] For example, in the presence of a negatively charged lipid film, water molecules will have a net orientation such that their hydrogens are directed "up" toward the surfactant at the surface; the opposite will occur in the presence of a positively charged surface.

In this chapter, we investigate the effects of protonation state (100% and 50%) on the structure of palmitic acid monolayers at the air-water interface. Using surface tensiometry, we quantify the ESP of PA as a function of pH for these two scenarios. We utilize IRRAS to determine the lattice packing of the monolayers and confirm the ionization of the headgroup at high pH. IRRAS data was collected in collaboration with Dr. Ellen Adams.[62,119] Finally, we investigate the interfacial water structure associated with these monolayers using VSFG and surface potential measurements. This project was conducted as part of an ongoing collaboration with, primarily, the Francesco Paesani group at UCSD.[62,63] In this collaboration, the Paesani group used molecular dynamics simulations to deduce sodium-carboxylate interactions, the various hydrogen-bonding environments that exist at the interface, and the molecular-level details which give rise to the VSFG spectrum of water in the presence of PA and PA/PA^- monolayers.

4.2 Materials and Methods

4.2.1 Materials

For the IRRAS measurements, deuterated palmitic acid (d_{31}-PA, >98%, Cambridge Isotope Laboratories) was dissolved in chloroform to a concentration of approximately 2 mM. VSFG and surface potential measurements were performed with non-deuterated palmitic acid (PA, >99%, Sigma Aldrich). Solutions of approximately 2 mM PA in chloroform were utilized for the VSFG and surface potential measurements. All monolayers were spread to an MMA of 20.5 $Å^2$/molecule in Petri dishes, and a 10-minute period was allotted for chloroform evaporation prior to data acquisition for the IRRAS, VSFG, and surface potential measurements. Surface potential measurements were calibrated with data acquired from 10 mM sodium dodecyl sufate (SDS, ≥98%) and 1 mM cetyltrimethylammonium bromide (CTAB, ≥98%) solutions. These concentrations are above the CMC of the respective compounds.[120]

Both subphase solutions contained a background electrolyte concentration of 100 mM NaCl to stabilize the pH 8.7 solution against acidification from the surrounding environment (measured pH between 8.7 and 8.9). The NaCl crystals were first baked at 650°C for at least 8 hours to remove organic contaminants.[121,122] The pH 8.7 solution was made via was addition of NaOH (99%, Mallinckrodt) to the 100 mM NaCl solution in water (≥ 18.0 MΩ•cm). For the VSFG and surface potential measurements, no pH adjustments were made to the fully protonated system (pH 5.6 and pH 6.7 solutions both produce a fully protonated PA film).

4.2.2 Methods

Infrared Reflection-Absorption Spectroscopy

A custom-built setup used for IRRAS measurements was placed in the chamber of an FTIR spectrometer (Spectrum 100, Perkin Elmer), and consists of two gold mirrors. The first mirror directs the incoming unpolarized IR beam to the sample surface at a 46° angle of incidence, relative to the surface normal. Each spectrum presented here is the average of at least three individual trials which have been baseline-subtracted by a third order polynomial.

Equilibrium Spreading Pressure

In a Langmuir MiniMicro trough (Biolin Scientific), ground PA crystals (~1-3 mg) were sprinkled on the aqueous pH subphase of interest with a microspatula after the subphase had been swept with barriers to check for organic contamination ($\Pi \leq 0.20$ mN/m). Surface pressure was measured with a filter paper Wilhelmy plate. ESP was determined when the surface pressure of the system changed by ≤ 0.10 mN/m over a period of fifteen minutes.

Surface Potential

Surface potential (ΔV) was measured with a custom-built setup, designed and implemented by Tehseen Adel, using an ionizing ^{241}Am source situated 5 mm above a Petri dish with a platinum counter electrode immersed in the solution subphase.[123] The surface potential system was housed in a Plexiglas box inside of a Faraday cage (ThorLabs) to prevent electrical interference. Measurements were obtained from the output of Keithley

6517B electrometer (Tektronix/Keithley). At least three individual measurements were taken for each system and averaged to produce the values reported here.

Vibrational Sum Frequency Generation Spectroscopy

The ~4 W output of a Ti:sapphire regenerative amplifier (Spitfire Ace, Spectra Physics) was split to produce visible and tunable IR beams. The IR beam was produced by directing half of the output to an optical parametric amplifier (TOPAS-C, Light Conversion) coupled to a non-collinear difference frequency generator (NDFG, Light Conversion). The visible beam (800 nm) was produced by directing the remaining portion of the amplifier output to an etalon (SLS Optics) to create asymmetric picosecond pulses. The IR (10 μJ, 68°) and visible (70 μJ, 52°) beams were incident in a co-propagating geometry and the reflected sum frequency signal was collected by a spectrometer (Spectra Pro-500i, Princeton Instruments) and a liquid nitrogen-cooled CCD (Spec-10:400B, Princeton Instruments). Spectra were background-subtracted and normalized to the non-resonant profile of a z-cut quartz crystal.

4.3 Results and Discussion

4.3.1 Protonation State and 2D Lattice Packing of PA Monolayers

The surface-pK_a of PA has been reported to be ~8.7.[65,73] At the interface, this is confirmed by the presence of markers of protonated and ionized carboxylate groups in the IRRAS spectra of the PA/PA^- system on a pH 8.7/100 mM NaCl subphase. As seen in Fig. 4.1, the IRRAS spectrum of the PA/PA^- monolayer exhibits vibrational modes corresponding to the C-OH stretch at 1275 cm^{-1}, as well as the CO_2^- asymmetric stretch (ν_{AS} CO_2^- at approximately 1534 cm^{-1}). Due to interference from water vapor bands in the

region, the weaker CO_2^- symmetric stretch (ν_S CO_2^-, typically around 1410 cm^{-1}) was not observed. The spectrum of the fully protonated PA monolayer on 100 mM NaCl did not exhibit any CO_2^- modes, but does include both the C-OH and the carbonyl (ν C=O, 1722 cm^{-1}) stretches.

Also observed in Fig. 4.1 are the vibrational modes associated with the CD_2 scissoring mode (δ CD_2) of the alkyl chains of the deuterated PA monolayers. Monolayers typically can pack in three different lattice patterns (hexagonal, triclinic, orthorhombic), as illustrated in Fig. 4.2. Each lattice packing structure results in a unique scissoring mode frequency due to differences in the interchain vibrational interactions of the lipid molecules.[124,125] At a frequency of 1089 cm^{-1}, it is determined that the PA molecules comprising the monolayers are packed in hexagonal arrangements on both subphases. Changes in ionization state do not affect the 2D lattice packing structure of the PA monolayers.

4.3.2 Equilibrium Spreading Pressure of PA and PA/PA^- Monolayers

The equilibrium spreading pressure is defined as the surface pressure at which there exists a thermodynamic equilibrium between the 2D monolayer and the 3D bulk phase of lipid material. Upon spontaneous spreading of PA molecules from crystals on the aqueous surface, thermodynamic equilibrium is achieved for both the PA and the PA/PA^- systems at 17.8 ± 0.9 mN/m and 21.1 ± 0.3 mN/m, respectively. These ESP values are elevated from the value obtained on pure water, ~7.5 mN/m. Molecular dynamics simulations conducted by the Paesani group (UCSD) reveal that Na^+ ions in the 100 mM NaCl background electrolyte form contact ion pairs with both oxygens of PA^- (with a 1:1 ratio

of O:Na) and with the carbonyl oxygen of PA.[62] The interaction of the Na^+ ion with PA or PA^- increases its surface propensity.[21] This effect becomes evident in the measured ESP values relative to pure water as the presence of the ion may increase the adhesion force of the surfactant to the surface.[126] There is precedent for this observation as other lipid films have shown elevated ESPs in the presence of NaCl.[127]

The increased ESP of the PA/PA^- system, relative to the PA system, can be attributed to changes in the forces between the surfactant molecules at the interface. The 50% protonation state of the lipid headgroups increases hydrogen bonding between PA and PA^- headgroups as well as repulsive forces between neighboring charged PA^- groups. Similar results have been reported for the ESP of monolayers of oleic acid as the pH of the subphase is increased.[128] The increased charge-induced interactions can lead to elevated surface pressures in ESP, and have also been observed in compression isotherm measurements.[129]

4.3.3 Interfacial Organization Determined by Surface Potential

The surface potential was determined for the PA and PA/PA^- monolayer systems, as well as for Gibbs monolayer SDS and CTAB control systems. The ΔV data is presented in Fig. 4.3 for SDS, CTAB, PA, and the PA/PA^- systems. These values were utilized by Paesani and coworkers, to calculate the VSFG spectra of the PA and PA/PA^- monolayers in the OH stretching region.[63] The absolute difference between the ΔV values for CTAB and SDS found here is 716 ± 134 mV. Nakahara *et al.* found this difference to be 562 mV, which agrees fairly well with our results.[120] CTAB and SDS serve as calibration points for our PA and PA/PA^- systems as they represent full monolayer coverage of positive and

negative surfactant systems, respectively. The PA/PA^- system produces a measured ΔV value of -306 ± 13 mV, which lies closer to the end marked by SDS. One would expect this result as half of the molecules in the monolayer system are negatively charged. The fully protonated PA monolayer yields ΔV = -208 ± 25 mV, which, along the trend, is more positive than the PA/PA^- system.

4.3.4 Interfacial Water Structure

VSFG spectra of the PA and PA/PA^- monolayers in the OH stretching region reveal the interfacial water structure associated with these lipid systems. Before discussing interfacial water associated with the lipid systems, one must first understand the water structure associated with the bare surface. The VSFG spectrum of the bare water surface is presented in Fig. 4.4 and contains a broad band from 3000 to 3600 cm^{-1} and a sharp feature at ~3700 cm^{-1}. This sharp feature is the stretch associated with what is referred to as the "dangling-" or "free-OH" at the interface, where one of the O-H bonds of water is directed out of the bulk and into the air. It has been reported that approximately 20% of the molecules in the surface water layer contribute to this free-OH signal.[130]

The spectrum of a 1 mM SDS solution was also collected in this vibrational region as a spectral control for a negatively-charged, highly ordered interface. Additionally, this system was used to test the effect of acquisition time on the intensity of the SFG signal collected by the detector used in the setup. A two-minute spectral acquisition period was sufficient to collect a high S/N spectrum of the OH region associated with 1 mM SDS. Ideally, if one were to shorten this acquisition period by a factor, then the intensity of the spectrum should also be divided by that factor. A comparison of absolute counts acquired

for SDS for 2-minute versus 30-second collection periods are shown in Fig. 4.5. The intensity of the spectra differs by a factor of four, confirming the additive intensity of our detector. Interfacial water structure spectra for the PA and PA/PA^- monolayer systems were collected with an acquisition time of 5 minutes, and an acquisition time of 10 minutes was required for the bare water surface to achieve decent S/N. Therefore, to compare spectral intensity of bare water and the monolayer systems, the intensity of the water spectrum was divided by 2. All three spectra (PA, PA/PA^-, and bare H_2O) are shown in Fig. 4.6.

The presence of both monolayers at the interface results in the disappearance of the free-OH mode at ~3700 cm^{-1}. The PA spectrum exhibits two broad bands, one centered at ~3215 cm^{-1}, and the other centered at ~3500 cm^{-1}. The more intense, higher frequency band at 3500 cm^{-1} is composed of two separate modes, one centered at ~3450 cm^{-1} and the other at 3575 cm^{-1}. These features have been previously reported by others in the literature,[122,131,132] and the resolution of these modes may be impacted by the broadness of the IR profile in each individual SFG setup, which can affect the shape of the water spectra. The 3200 cm^{-1} and 3450 cm^{-1} bands are due to the collective stretching vibrations of the interfacial water molecules. However, through collaboration with the Paesani (UCSD), Geiger (Northwestern), and Morita (Tohoku) groups, it was determined that the low frequency spectral feature at ~3200 cm^{-1} is predominantly modulated by the bulk, third-order ($\chi^{(3)}$) contribution to the VSFG response.[63] The highest frequency mode of the spectrum at 3575 cm^{-1} is attributed to the more weakly hydrogen-bonded OH groups of the fully protonated carboxylic acid groups of PA and neighboring water molecules.[122,131]

The PA/PA$^-$ monolayer system produces a different spectrum in the OH stretching region than the fully protonated PA monolayer. The overall intensity of the VSFG response is greater for the 50% deprotonated monolayer. As the VSFG response requires a lack of inversion symmetry, the presence of a charged surfactant layer at the interface will induce ordering of water molecules further into the bulk. This increased probe depth available to SFG will include more water molecules, and therefore, the spectral intensity of the VSFG signal will be greater. Here, the intensities of the 3200 cm^{-1} and the 3450 cm^{-1} bands are roughly equivalent. However, the mode at 3575 cm^{-1} contributes far less to the overall intensity of the high frequency band. This is to be expected as there exist fewer protonated carboxylic acid groups with hydrogen-bonded OH groups in the monolayer system at pH values near the pK$_a$ of PA.

The spectra shown in Fig. 4.6 are those of the effective second-order nonlinear susceptibility, $\chi^{(2)}_{eff}$.

$$\chi^{(2)}_{eff,ssp} = L_{yy}(\omega_{SFG})L_{yy}(\omega_{vis})L_{zz}(\omega_{IR})\sin\beta_{IR}\chi^{(2)}_{yyz}. \quad (4.1)$$

As the VSFG intensity is proportional to the square of the effective nonlinear susceptibility, upon calculation of the Fresnel factors (L_{ii}) allows one to correct the spectra and express $\left|\chi^{(2)}_{yyz}\right|^2$. Following the formalism of Hong-fei Wang,[61] we calculate these spectra in Fig. 4.7 for pure water, PA, and PA/PA$^-$ monolayers. It is important to make such corrections when comparing spectra obtained with experiment and theory as the spectra collected in an experiment exhibit a dependence on the beam geometry in the VSFG setup.

It is important to note that the formalism of the Fresnel factors still conjures much debate in the SFG community. Those used here (see Chapter 2 and Appendix A) follow the formalism of Yuen-Ron Shen[133] and Hong-Fei Wang.[61] Here, we also calculated the Fresnel-corrected spectra using the formalism of Shultz *et al*.[134] and Wolfrum *et al*.[135] Upon examination of the equations presented by the various authors, one can deduce that the primary differences in the formalisms lie in the expressions for the SFG beam. The VSFG spectrum, expressed as $\chi^{(2)}_{yyz}$, for the bare water surface is shown in Fig. 4.8 after being corrected for the Fresnel coefficients with the three formalisms. The low-frequency side of the spectrum exhibits the greatest differences when normalized to the various Fresnel factor formulas. A similar result was also obtained by Wang *et al.*[136] in his 2011 paper where he reported on these inconsistencies using various examples of water SFG spectra in the literature. A thorough discussion of the formulas and the workbooks used to properly calculate the Fresnel factors is presented in Appendix A.

4.4 Conclusions

In this study, the effect of ionization state on the interfacial properties of PA monolayers was investigated under two scenarios, 100% protonated and 50% protonated. IRRAS spectra reveal the presence of both protonated and deprotonated molecules at pH 8.7, thereby confirming its surface-pK_a value. Although the headgroup signatures of PA change with pH, the lattice packing of the monolayers remains the same, with both systems packing in a 2D hexagonal lattice. While both monolayer systems achieve thermodynamic equilibrium states, deprotonation in the PA/PA^- system leads to an elevated ESP relative to the fully protonated PA system due to increased repulsive forces between the surfactant

molecules at the interface. It was also demonstrated that the background electrolyte (100 mM NaCl) elevated the ESP of the fully protonated system relative to pure water due to contact ion pair formation of the Na^+ ion to the carbonyl and carboxylate groups of PA and PA^-, respectively.

Both PA and PA/PA^- monolayer systems induce a change in the interfacial water organization when compared to the bare water surface. The deprotonated PA^- molecules in the PA/PA^- system induce more order of the interfacial water molecules due to the increased charge at the interface, and contribute to differences in the various hydrogen-bonding motifs of water than the PA monolayer system. Normalization of the VSFG spectra to Fresnel factors does not greatly change the shape of the spectra when following the formalisms of Hong-Fei Wang. However, using other mathematical formalisms in the literature induces large changes in the spectra. Surface potential values were determined such that the VSFG spectrum of water associated with these monolayers can be calculated with molecular dynamics simulations by our collaborators in the Paesani group. These simple model systems of low salt concentration and a single-component lipid films represent a necessary first step in understanding the complex interfacial structure of SSA, particularly under changing pH environments.

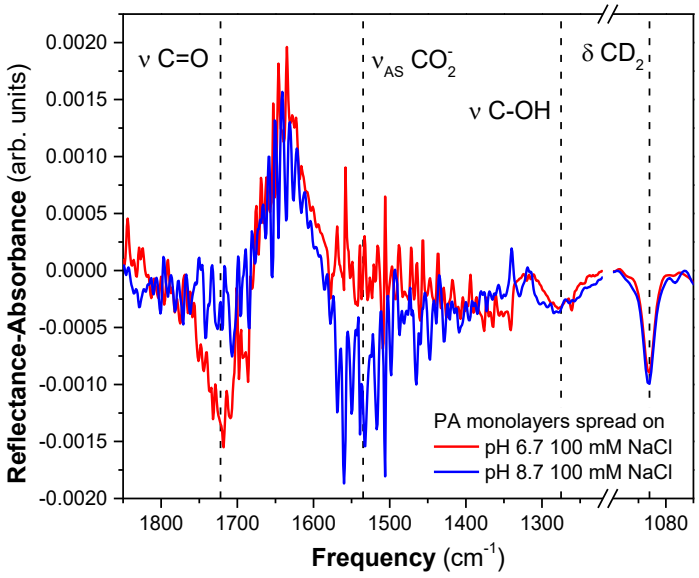

Figure 4.1. IRRAS spectra of the headgroup and scissoring mode regions of d_{31}-PA on NaCl salt-buffered pH 6.7 (fully protonated) and pH 8.7 (50% protonated) subphases (both with 100 mM NaCl). The C=O and C-OH stretches (~1720 cm^{-1}, 1275 cm^{-1}) and the asymmetric stretch of the CO_2^- mode (~1535 cm^{-1}) are markers of the protonation state of the d_{31}-PA molecules in the monolayer. The scissoring mode at 1089 cm^{-1} indicates the 2D lattice packing of the monolayer.

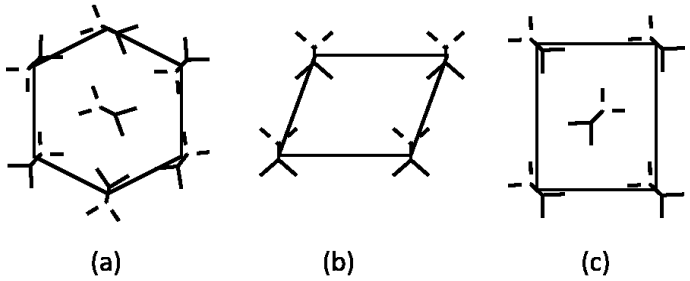

Figure 4.2. Schematics of the three possible lattice packing structures identified by the frequency of the CH_2 or CD_2 scissoring modes. (a) hexagonal, δCH_2 1468 cm^{-1}, δCD_2 1089 cm^{-1}; (b) triclinic, δCH_2 1471 cm^{-1}, δCD_2 1092 cm^{-1}; (c) orthorhombic, δCH_2 1462/1474 cm^{-1} doublet, δCD_2 1086/1094 cm^{-1} doublet.[48]

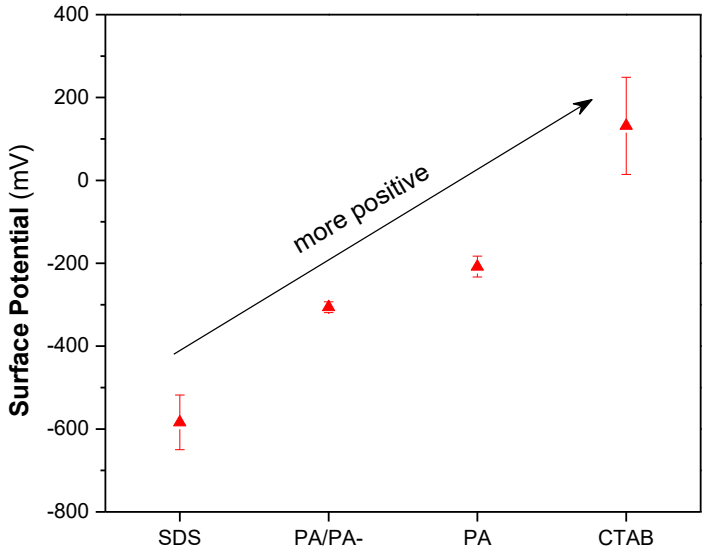

Figure 4.3. Surface potential measurements for SDS, PA/PA$^-$ (pH ~8.7), PA, and CTAB monolayer systems. SDS and CTAB are used as controls, and the values of ΔV become less negative (more positive) when the PA monolayer is fully protonated.

*CTAB and SDS have been reported to have limiting molecular areas of 32 Å^2/molecule and 24 Å^2/molecule, respectively.[137] If the ΔV value for each system is normalized by these molecular areas (+131.7 mV/32 = +4.1 mV for CTAB, and -583.9 mV/24 = -24.3 mV for SDS), then the midpoint of the systems lies at -10.1 mV. If we normalize the ΔV measurement for PA to the spread MMA (20.5 Å^2/molecule), we calculate a normalized ΔV of -10.1 mV, indicating an electrically neutral monolayer system. Assuming no change in molecular area upon deprotonation, the PA/PA$^-$ system produces a normalized ΔV measurement of -14.9 mV. The measured surface potential is the sum of dipole contributions from oriented water molecules, lipid headgroups, and the alkyl chains.[52] While normalization to molecular area is likely an oversimplification, such normalizations should be considered as at least a first approximation when evaluating surface potentials relative to other lipid species which occupy more or less of the available surface area in the measurement.

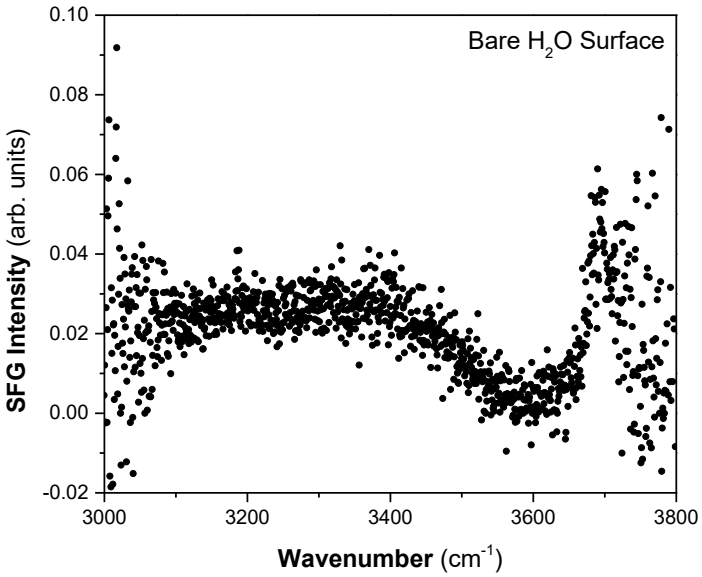

Figure 4.4. VSFG spectrum of the bare air-water interface. This spectrum is the average of three individual spectra, each acquired for 10 minutes.

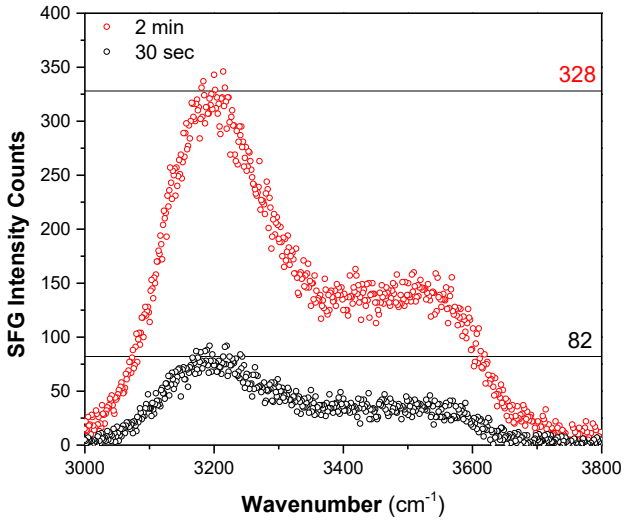

Figure 4.5. VSFG Intensity counts of SDS (not normalized by a quartz profile) acquired for 30 seconds (black) and 2 minutes (red) to demonstrate the additivity of intensity with time.

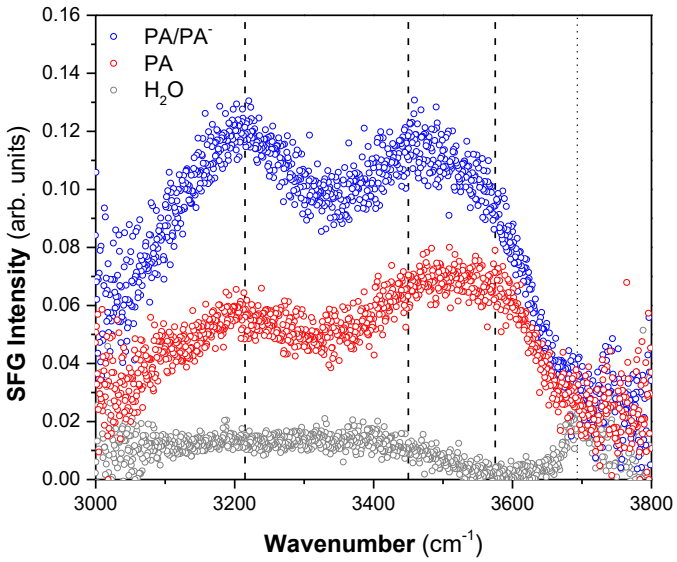

Figure 4.6. VSFG spectra of the OH stretching region associated with PA (red) and PA/PA$^-$ (blue) monolayers and that of the bare air-water interface (gray). Lines are drawn to guide the eye at 3215 cm^{-1}, 3450 cm^{-1}, 3575 cm^{-1}, and 3700 cm^{-1}.

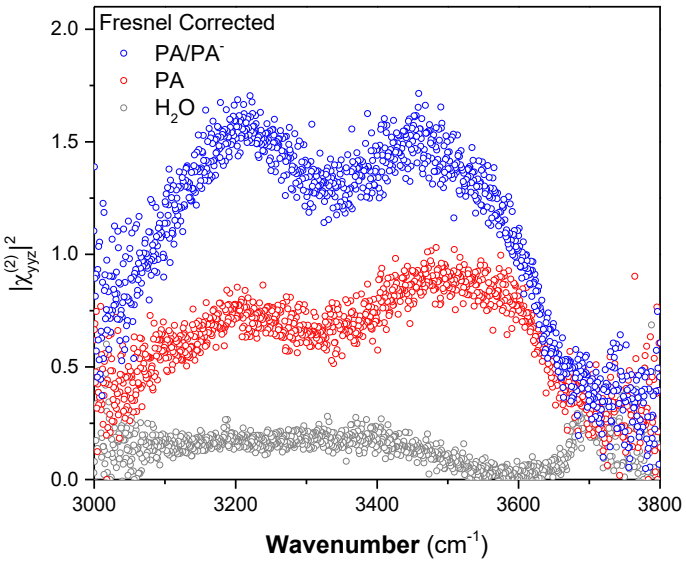

Figure 4.7. Fresnel-corrected VSFG spectra of the PA, PA/PA$^-$ monolayers and the bare water interface following the formalisms of Hong-Fei Wang.

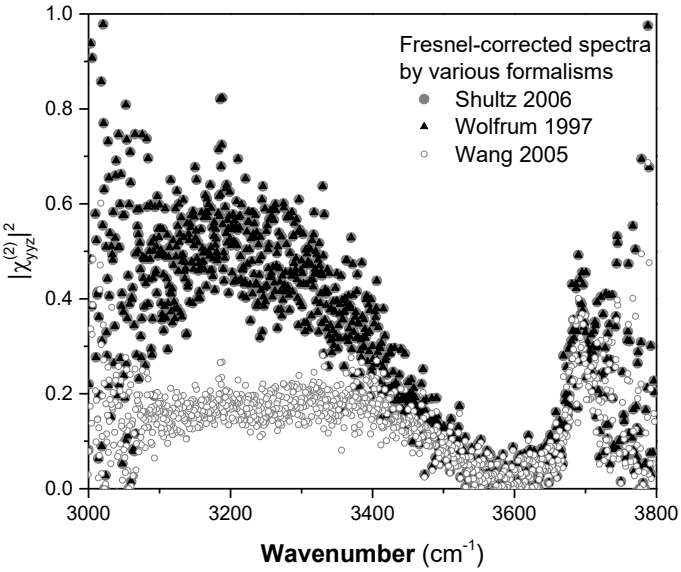

Figure 4.8. Comparison of Fresnel-corrected VSFG spectra of the bare air-water interface.

Chapter 5: Thermodynamic versus Non-Equilibrium Stability of Palmitic Acid Monolayers in Calcium-Enriched Sea Spray Aerosol Proxy Systems

Reproduced in part with permission from the PCCP Owner Societies: B. A. Wellen Rudd, A. S. Vidalis, and H. C. Allen "Thermodynamic versus Non-Equilibrium Stability of Palmitic Acid Monolayers in Calcium-Enriched Sea Spray Aerosol Proxy Systems" *Phys. Chem. Chem. Phys.,* 2018, DOI: 10.1039/C8CP01188E.

5.1 Introduction

The structure of organically enriched SSA can be described as an aqueous core surrounded by an organic layer of a complex mixture of surface active molecules, such as fatty acids.[12-15] Of these fatty acids, those with chain lengths of sixteen and eighteen carbons are the most abundant, and the distribution of the fatty acids in the aerosol can vary with stages of biological activity.[12,15,16] In both field and controlled laboratory studies, enrichment of Ca^{2+} ions, defined as the ratio of the concentration of Ca^{2+} relative to Na^{+} ions in the aerosol phase and in bulk seawater (10 mM Ca^{2+}, 0.47 M Na^{+}), was observed for a range of aerosol sizes.[29,33,34] Additionally, calcium was found to be more enriched when compared to the other major seawater ions (K^{+}, Mg^{2+}, Cl^{-}, SO_4^{2-}). Interestingly, the mechanism of calcium enrichment in the aerosol phase is not agreed upon. Jayarathne *et al*[33] and Cochran *et al*[10,12] argue that the enrichment is due to the association of Ca^{2+} ions with organic complexing agents, and the enrichment of the ion will depend on the production mechanism of SSA. However, Salter *et al*[34] posed a possible pathway to

calcium enrichment via the formation of ionic clusters of carbonate at the water surface, without organic complexation. Their result suggests that organics may not drive ion enrichment, or are only required in small amounts.

Because the climate-relevant effects of SSA (light scattering, lifetime, reactivity, etc.) are influenced by their organic coatings,[20,21,24,25,89,91,93] the study of the impact of chemical complexity (i.e. ions, pH, mixtures) on monolayer properties is of importance. One way to evaluate monolayer stability is in terms of ESP, the thermodynamic equilibrium between 2D (monolayer) and 3D (bulk crystalline) states.[35] In a recent review, it was pointed out that for many systems of atmospheric relevance, ESPs are not known,[138] and that some surface tension-dependent models could actually use values of ESP to better understand film-forming organics on proxy droplets and particles.[139] The study of ESP may even extend past fundamental significance to describe real aerosol particles as it has been recently shown that complex 3D self-assembled phases form in aging model aerosol particles, which would increase the complexity of systems commonly modelled as monolayers alone.[140] Another evaluation of stability, monolayer relaxation, comes from interpreting changes in molecular area or surface pressure under mechanically-controlled conditions in a Langmuir trough, which is a non-equilibrium process.[36] Rarely though, are both techniques, ESP and non-equilibrium relaxation, evaluated together for the same systems.

In this study we examine the effects of Ca^{2+} interactions with monolayers of palmitic acid at the air-aqueous interface as an idealized simple proxy system of SSA using a series of Ca^{2+} concentrations above and below 10 mM to represent calcium enrichment or depletion in the aerosol phase; Ca^{2+} enrichment in SSA may change as a function of the

aerosol size and environment based on relative humidity conditions (i.e. high humidity would lead to water uptake thereby diluting the Ca^{2+} concentration). Binding of the ion to the PA headgroup is studied with IRRAS. Additionally, we utilize surface tension techniques and BAM to investigate the effect that such binding has on the stability properties of the monolayers, in both equilibrium and non-equilibrium systems, through the determination of ESPs and constant-surface pressure NER mechanisms. IRRAS and VSFG spectroscopy are used to investigate the surface presence of PA molecules during ESP measurements at high Ca^{2+} concentration. We also discuss the cautions that must be exercised when interpreting monolayer stability in non-equilibrium systems. Through this work, the driving force of Ca^{2+} enrichment in the aerosol phase via binding, and the consequences of such enrichment on the stability of organic films at the aerosol-atmosphere interface are revealed.

5.2 Experimental Methods

5.2.1 Materials

Solid crystals of palmitic acid (PA, >99%, Sigma Aldrich) were used as received for the ESP measurements, and solutions of PA were prepared in chloroform (HPLC grade, Fisher Scientific) to a concentration of approximately 2 mM for monolayer NER experiments. Deuterated palmitic acid (d_{31}-PA, >98%, Cambridge Isotopes Laboratories) was dissolved in chloroform to prepare spreading solutions for IRRAS experiments. The $CaCl_2$ solutions were diluted from stock solutions prepared by dissolving calcium chloride dihydrate (ACS grade, Fisher Scientific) in ultrapure water (>18.0 MΩ•cm, Barnstead Nanopure Filtration System D4741). The stock solutions were purified by previously

reported methods,[121] and titrated via the Mohr technique to determine chloride concentration prior to dilution.[141] To rule out the possibility of trace metals in our $CaCl_2$ solutions, control studies were conducted to reveal that the addition of EDTA (to bind and remove possible trace metals) did not affect the deprotonation signatures of d_{31}-PA on 300 mM $CaCl_2$ solutions. Solutions were prepared and equilibrated at room temperature. All experiments were conducted at 21 ± 1°C with a relative humidity of 27 ± 9%.

5.2.2 Methods

Equilibrium Spreading Pressure

Surface pressure in the ESP experiments was measured by a filter-paper Wilhelmy plate (Whatman 41, ashless grade) in a Teflon Langmuir MiniMicro trough (Biolin Scientific, area 145 cm^2). After a thorough cleaning procedure of ethanol and nanopure water, the trough was filled with the subphase of interest. The surface was swept with two Delrin barriers to ensure cleanliness ($\Pi < 0.20$ mN/m) prior to the start of the experiment. Approximately 1-3 mg of ground PA crystals were sprinkled across the surface with a spatula, and the time evolution of the surface pressure was recorded. When possible, a finite value of ESP was taken as the surface pressure at which a change of ≤ 0.1 mN/m occurred over a period of 15 minutes.

Monolayer Non-Equilibrium Relaxation at Constant Surface Pressure

After verifying that the aqueous surface in the Langmuir trough was clean (as described previously), monolayers of PA were spread dropwise by a microliter syringe (50 µL, Hamilton) on the subphase of interest. The monolayers were compressed by symmetric compression of the trough barriers to a target surface pressure (5 mN/m or 25 mN/m), and

were maintained at that surface pressure by continuous motion of the barriers at a maximum rate of forward/backward motion of 1 mm/min. The change in relative area (A/A_0) was then analyzed as a function of time.

Infrared Reflection-Absorption Spectroscopy

A custom-built setup used for IRRAS measurements was placed in the chamber of an FTIR spectrometer (Spectrum 100, Perkin Elmer), and consists of two gold mirrors. The first mirror directs the incoming unpolarized IR beam to the sample surface at a 46° angle of incidence, relative to the surface normal. As the beam is reflected off the surface, it is directed to a liquid nitrogen-cooled MCT detector by the second gold mirror. Each spectrum is the result of coaveraging 300 scans over the full spectral range (4000-450 cm^{-1}) at a 4 cm^{-1} resolution. The spectra shown here have been baseline-subtracted by a third order polynomial and are the average of at least 3 individual spectra.

Vibrational Sum Frequency Generation Spectroscopy

The ~4 W output of a Ti:sapphire regenerative amplifier (Spitfire Ace, Spectra Physics, 75-femtosecond pulse length) was split to produce visible and tunable IR beams. To produce the IR beam, half of this output was directed to an optical parametric amplifier (TOPAS-C, Light Conversion) coupled to a non-collinear difference frequency generator (NDFG, Light Conversion). The remaining portion of the amplifier output, used as the visible beam, was directed to an etalon (SLS Optics) to create asymmetric picosecond pulses with a FWHM of 12 cm^{-1}. The IR (centered at 2900 cm^{-1}, 15 μJ, 68°) and visible (800 nm, 90 μJ, 52°) beams were incident in a co-propagating geometry and the reflected

sum frequency signal was collected by a spectrometer (Spectra Pro-500i, Princeton Instruments, 1200 grooves/mm grating) and a liquid nitrogen-cooled CCD (Spec-10:400B, 1340×400 pixels, Princeton Instruments). Spectra were measured in *ssp* and *ppp* polarization combinations with 5-minute exposure times. All spectra were background-subtracted and normalized to the non-resonant profile of a z-cut quartz crystal. In this study, VSFG spectra of the CH stretching region were used to calculate the orientation of the terminal methyl group of the hydrocarbon chains of PA, thereby determining the tilt angle of the PA molecules in the monolayer (Appendix A).

Brewster Angle Microscopy

Brewster angle microscopy was used to image the surface during monolayer NER at 25 mN/m. A HeNe laser (Model 30528, Research Electro-Optics) emits vertically-polarized light at a wavelength of 543 nm and at a maximum power of 0.5 mW. The emitted light is attenuated by a half wave plate (Ekspla) and then further filtered by a Glan prism (Ekspla) before impinging the sample surface at the Brewster angle of the subphase (i.e. $\theta_{B,water} \approx 53.1^{\circ}$). The reflected light is collected by a 10x infinity-corrected super-long working distance objective lens (CFI60 TU Plan EPI, Nikon) and then collimated by a tube lens (MXA22018, Nikon) onto a back-illuminated EM-CCD camera (DV887-BV, 512×512 active pixels, 16×16 μm pixel size, Andor). Images were cropped from their original size of 8.2×8.2 mm to show only the most resolved portion. The lateral resolution of the BAM images is 1.3 μm.

5.3 Results and Discussion

5.3.1 Binding of Ca^{2+} to the Palmitic Acid Headgroup

To investigate the binding of Ca^{2+} ions to the carboxylic acid headgroup of PA, IRRAS spectra were collected of d_{31}-PA monolayers spread to a condensed phase in a Petri dish at a mean molecular area of 20.5 $Å^2$/molecule. The resulting spectra are shown in Fig. 5.1a for Ca^{2+} concentrations of 0 to 1 mM, and Fig. 5.1b for concentrations of 10 to 300 mM. In this region, there are four vibrational modes associated with the palmitic acid headgroup. The C=O (1722 cm^{-1}) and C-OH (1280 cm^{-1}) stretches are indicative of a protonated headgroup at the interface, and the asymmetric (~1540 cm^{-1}) and symmetric (~1410 cm^{-1}) stretches ($\nu_{AS,}$ ν_S) of the CO_2^- group are markers of deprotonation. The large positive feature in the spectra at ~1650 cm^{-1} is the water bending mode from the aqueous subphase and is the result of the change in the refractive index of water in this wavelength region.[111,142] As to not obscure the signals from the headgroup, perdeuterated PA (δCD_2 1089 cm^{-1}) was chosen for these experiments to remove the CH_2 scissoring mode (~1460-1470 cm^{-1}) from the spectral region.[48]

From the spectra, it can be seen that Ca^{2+}-induced deprotonation of the carboxylic acid headgroup is observable even at the very low concentrations in Fig. 5.1a. The C=O and CO_2^- asymmetric stretch modes are the best indicators of the protonation state of the lipid headgroups. As the concentration of Ca^{2+} increases, the intensity of the C=O mode decreases, and that of the CO_2^- asymmetric stretch increases, as shown in Fig. 5.1c. While the intensities of the C=O and CO_2^- modes shed light on the protonation state of the molecules at the interface, the frequencies of the asymmetric and symmetric stretching modes of the CO_2^- group are used to reveal information on the binding motif of the Ca^{2+}

ion to the carboxylate headgroup of PA. Although we have previously studied Ca^{2+}:PA binding with VSFG,[115,132] spectra collected with IRRAS have the advantage that both the symmetric and the asymmetric modes can be observed and interpreted together. In Fig. 5.1d, the center frequencies of the asymmetric (blue squares) and symmetric (red circles) stretches of the CO_2^- group are shown for all concentrations of Ca^{2+} upon which deprotonation of PA was observed within our limits of detection.

In previous literature, the frequency difference of asymmetric and symmetric stretches ($\Delta\nu_{AS-S} = \nu_{AS} - \nu_S$) of metal-bound acetate CO_2^- modes was used to characterize the binding motif of ions to acetate groups in four main geometries: monodentate, ionic, chelating bidentate, and bridging bidentate.[143,144] For all Ca^{2+} concentrations studied here, the value of $\Delta\nu_{AS-S}$ of the d_{31}-PA monolayers stays relatively constant at ~132 cm^{-1}. This value would generally associate these systems with an ionic binding motif, however contributions due to other binding geometries are also possible within the uncertainty of the measurements, and the overlap in $\Delta\nu_{AS-S}$ assignments.[145,146] While these empirical rules have been applied to monolayer systems in the past,[114,147] they were originally stated based on data of anhydrous crystals and ill-defined solutions of aqueous acetates with transition metal ions. Since the development of these guidelines, not much has been postulated about the details on the specifics of the binding motifs.

The values of ν_{AS} range from 1534-1544 cm^{-1} and those of ν_S range from 1403-1413 cm^{-1}, with both modes blue-shifting with increasing concentration of Ca^{2+} in the subphase. The increase in frequency could be attributed to a change in the force constant of the O-C-O stretch as Ca^{2+} ions bind to the carboxylate headgroup of PA, as well as a

change in the local hydration environment of the ion bound to the carboxylate.[114,147,148] The higher frequencies of the CO_2^- stretches observed in the more concentrated Ca^{2+} regime suggest a more dehydrated binding state. This has been previously observed with high concentrations of Ca^{2+} ions and phosphate lipid headgroups.[50] So while the frequency difference between the asymmetric and symmetric stretches, derived from the empirical rules established for the bulk and crystalline phase[149-151], reveals an ionic binding motif for all concentrations, the level of hydration in that motif can vary with ion concentration as shown in Fig. 5.2.

Analysis of the CD_2 scissoring mode (δCD_2) allows for interpretation of the lattice packing structure (hexagonal, orthorhombic, triclinic) of the d_{31}-PA molecules at the interface.[124,125] Fig. 5.1a-b shows this region of the spectra (1080-1100 cm^{-1}). At all $CaCl_2$ concentrations, the δCD_2 mode is located at 1089 cm^{-1}, indicating that the PA molecules are packed in a hexagonal arrangement. This has been observed elsewhere in literature for both experimental measurements and theoretical simulations.[62,152,153] As a change in frequency of the scissoring mode is not observed, the 2D lattice packing structure of PA monolayers is not affected by its interaction with Ca^{2+} ions.

5.3.2 Stability of Palmitic Acid on $CaCl_2$ Subphases

Thermodynamic Equilibrium Spreading Pressure

Surface pressure time evolution curves of PA on subphases of $[Ca^{2+}] \leq 1$ mM are shown in Fig. 5.3a. PA crystals are sprinkled on the surface, and spontaneous spreading of molecules from the 3D bulk crystals to a 2D film causes a rise in surface pressure to values greater than 0 mN/m. The surface pressure at which there exists a plateau in the time

evolution curve represents the ESP, defined as the thermodynamic equilibrium between the 2D and 3D phases.[35] The surface pressures at which these plateaus occur are shown in Table 5.1. In this concentration regime, it can be seen (Fig, 5.3a) that up to a concentration of 1 mM, the Ca^{2+}:PA monolayer systems reach an equilibrium state, and the binding of Ca^{2+} to PA gives rise to a lower energy surface revealed by the higher ESP relative to PA on pure water.

Previous results from the literature have shown that changes to the subphase, including the addition of salts, induce changes in ESP.[62,127,128] Salts, including $CaCl_2$, have a tendency to increase the surface tension of aqueous solutions relative to pure water.[154] One theory of ESP argued that ESP was a function of the surface tension of the bare liquid, the cohesion forces of the solid crystal at the interface, and the thickness of the surface layer.[155] Through this theory, assuming the cohesion of the solid is not affected by the liquid subphase, ESP would increase with increasing surface tension of the bare liquid.

While surface pressure elevation in surface adsorption isotherms can be attributed to higher concentrations of surfactant, the observed increase in ESP of the PA systems following salt addition can more appropriately be attributed to the effects of the Ca^{2+} ions on the organization of the film, and can be divided into two primary forces. The adhesion of the surface-active molecules to the surface (force 1) would be increased upon the presence of salt due to the interaction between the polar carboxylic acid group of PA and the ions that lie just beneath the surface layer.[110,126,156] In addition to the forces between the molecules and the surface, the presence of Ca^{2+} ions in solution will also affect the forces between individual surfactant molecules at the interface (force 2). As observed in Fig. 5.1a, Ca^{2+} induces a small fraction of dissociation in the PA film at low concentrations (most

noticeably at 1 mM concentration). Although it was not detected within the limits of detection by Tang *et al.* in their study of Ca^{2+} interaction with PA,[115] such ion-induced deprotonation can cause a change in the orientation of the dissociated carboxylate groups, resulting in increased repulsive forces between the molecules and increased surface pressure.[126,129,157]

The relative impact of a salt on the ESP of a film at the interface also partly depends on the energy of hydration of the influencing ion.[126] For example, we have previously shown that the addition of 100 mM NaCl to a fully protonated PA system will raise the ESP from 7.6 to 17.8 mN/m.[62] In the current study, it only required 1 mM $CaCl_2$ for PA to reach an ESP of 14.6 mN/m (from 7.5 mN/m for PA on pure water). The greater change induced by Ca^{2+} in raising the ESP of the PA system, in the low concentration regime, can be correlated to its larger energy of hydration (-1505 kJ/mol) versus that of Na^+ (-365 kJ/mol).[158] The energy of hydration is defined as the amount of energy released when one mole of the ion is dissolved in water to form an infinitely dilute solution.[158] Additionally, according to the Laws of Matching Water Affinities, Ca^{2+} ions have been shown to be well-matched to carboxylates as they share similar hydration properties, and the complexes readily form inner sphere ion pairs.[159] Such differences between divalent and monovalent interactions have been previously documented for ESP measurements as well as spectroscopic and molecular dynamics studies of ion binding to lipid headgroups at the interface.[50,157,160-162]

Unlike the low concentration regime, at $[Ca^{2+}] \geq 10$ mM, the ESP curves do not reach similar plateaus in surface pressure and their interpretation becomes more complicated. Fig. 5.3b shows the results for 10 mM $\leq [Ca^{2+}] \leq$ 300 mM, and rather than

reaching an equilibrium state, all of these systems instead establish a metastable state followed by a surface pressure decline. The values for the metastable states and the rates of surface pressure decline (approximated by a linear fit) are shown in Table 5.2. The maximum surface pressure attained at the metastable state decreases with increasing concentration of Ca^{2+}, and the rate of surface pressure decline increases with concentration indicating that the films become less thermodynamically stable with increasing Ca^{2+} concentration.

A previous study also examined the effect of Ca^{2+} on the ESP of palmitic acid films and revealed a similar trend to the data shown in Fig. 5.3.[163] In that study, the decline of the surface pressure versus time curves for PA on higher concentrations of $CaCl_2$ was attributed to the disappearance of the monolayer with time. Trapeznikov argued that this monolayer disappearance was due to molecules of calcium palmitate re-adsorbing to the 3D PA crystals, thus removing themselves from the 2D aqueous surface.[164] To test this theory of the surface pressure decline in the ESP measurements, we applied the use of IRRAS (surface-sensitive) and VSFG (surface-specific) spectroscopies to the PA system on 300 mM $CaCl_2$ (the most extreme case of surface pressure decline). If the monolayer were to disappear from the surface, then the CH stretching modes of the PA molecules should not be observed in surface-specific VSFG spectroscopic measurements of the air-aqueous interface, although, they could still potentially be seen with IRRAS.

IRRAS measurements were conducted during the course of an ESP experiment, where the background spectrum of the 300 mM $CaCl_2$ subphase prior to the addition of solid PA crystals was used as R_0. Spectra were acquired continuously as soon as the PA crystals were deposited to the surface. For reference, the points along the ESP curve at

which the spectra were taken are shown in the inset of Fig. 5.4 as colored symbols corresponding to their IRRAS spectrum. The first spectrum, starting at one minute after crystal deposition, shows no signatures of PA at the interface.

While still at a surface pressure of 0 mN/m, the IRRAS spectrum acquired at 7.5 minutes begins to show the CH stretching modes of the PA hydrocarbon chains. There are two likely reasons why the intensity of this spectrum is much lower than that of the third spectrum (also at 0 mN/m) at 13.5 minutes. The first could be the fact that each spectrum is the average of 300 individual scans, so it is possible that the molecules had not eluted from the crystals at the start of the scan, and therefore no modes were observed. Later in the acquisition period, PA molecules could have appeared in the 2D space and contributed to the signal. The average of the 300 scans would incorporate both of these periods, thus giving rise to the less intense modes. The other explanation could be that upon elution from the crystal surface, the 2D film resembles that of a spread PA monolayer into the gas-liquid condensed phase of an isotherm which also has surface pressures of 0 mN/m. At this stage of a surface pressure-area isotherm, large islands of PA are formed, around which there exists lipid-poor regions.[49] The average spectrum of a surface comprised of lipid-rich and lipid-poor regions could also give rise to weaker intensities than that of a homogenous film. From the fourth spectrum (13 mN/m, 19 min) through the end of the experiment, the intensity of the CH modes remains nearly unchanged.

While it is surface-sensitive, IRRAS has a probing depth that can detect signals from the bulk.[165] To gain further evidence that there is still some form of a PA monolayer at the interface, surface-specific VSFG measurements were also taken during the surface pressure decline period of PA on the 300 mM $CaCl_2$ subphase. These spectra are shown in

Fig. 5.5 for both *ssp* and *ppp* polarizations. The measurements of the CH stretching region (2800-3000 cm^{-1}) were acquired at intervals of 2 mN/m from the metastable state of the surface pressure versus time curve until the surface pressure reached 0 mN/m. From the spectra, it can be seen that the CH stretching modes are still observable at a surface pressure of 0 mN/m. As VSFG is surface-specific, the spectra collected with this method confirm the IRRAS interpretation that the PA monolayer remains at the surface. There is still a surface presence of the PA molecules, even at a surface pressure of 0 mN/m. These results suggest that the previous theory of Trapeznikov is flawed; the monolayer does not disappear from the surface during the surface pressure decline.

Using the intensity ratio of the ν_{AS}-CH_3 in *ppp* polarization to the ν_S-CH_3 in *ssp* polarization, the orientation of the terminal methyl group, θ_{CH3}, can be determined.[51,61,166] The tilt angle of the hydrocarbon chains, relative to surface normal, can be calculated from the relation, $\theta_{tilt} = 37° - \theta_{CH3}$, assuming a nearly trans configuration of the C_3 axis.[167] Within experimental error (including errors related to the laser system as well as those related to configurational differences in the monolayer systems upon changes in surface coverage), the alkyl chain orientation of the PA molecules does not significantly change during the course of the surface pressure decline (Fig. 5.5a). This was expected as it has been previously shown, with VSFG, that at high concentrations of Ca^{2+} in the subphase, the conformational ordering of PA remains similar for all nonzero values of surface pressure during a pressure-area isotherm.[115] Although this is not inconsistent with the surface pressure decline, the result leaves open the possibility that changes in the orientation of the CO_2^- headgroup may contribute to the surface pressure change rather than changes in the conformational ordering of the tails.

Because we have spectroscopic evidence that the surface pressure decline of PA molecules on high concentration $CaCl_2$ subphases is not due to the disappearance of the monolayers, we must attribute this phenomenon to other mechanisms. One possible explanation is that a closely-packed condensed state at a high surface pressure is not favorable for the ionized lipid molecules of calcium palmitate. Upon reaching this metastable state, the molecules relax into a more favorable configuration. While this state can eventually produce surface pressures of 0 mN/m for greater Ca^{2+} concentrations, there is still some form of a monolayer present, as evidenced by the CH stretching modes, even though it may not be complete (similar to the gas-liquid condensed phase of PA monolayers). The formation of these monolayer islands could also contribute to the slight change and increased error in the monolayer tilt angle measurement in Fig. 5 as the PA molecules in these islands can orient in different directions.

Relaxation phenomena of monolayers to more favorable states have also been considered in constant area NER experiments where monolayers are mechanically compressed to a target surface pressure and are then allowed to relax, subsequently lowering the measured surface pressure.[168] Thermodynamically, the process observed here could be described as a result of two steps. The first is the spontaneous spreading of the surfactant at the interface to reduce the free energy and decrease the surface tension ($\Delta\gamma < 0$, $\Delta G < 0$, $\Delta H < 0$).[169] This step would represent the period from time 0 to the metastable state. Then, as Ca^{2+} induces a charge in the PA molecules of the monolayer, a closely packed negatively charged system is no longer enthalpically favorable ($\Delta H > 0$), and the surface tension rises as a result ($\Delta\gamma > 0$, where $\Delta\gamma = \gamma_{final} - \gamma_{metastable}$).[170]

An alternative theory for the surface pressure decline comes from an understanding of the various equilibria occurring during an ESP measurement. Recall that the definition of ESP is the surface pressure at which the 2D monolayer and 3D bulk crystal phases are at equilibrium. When a finite value is obtained, it suggests that the monolayer is stable against the loss of molecules to dissolution or evaporation, which are often neglected in ESP experiments.[45] The complete picture of the various equilibria during an ESP measurement includes those between the 2D monolayer, 3D crystals, aqueous bulk phase, and vapor phase. Due to the low vapor pressure of PA,[171] the evaporation of the molecules can be considered negligible. In the scenario of the $[Ca^{2+}] \geq 10$ mM subphases, where finite ESP values are not attained, the additional equilibrium between the 2D monolayer and the aqueous subphase should also be considered. At a fixed area, it has been shown that increased concentrations of calcium can increase the surface tension (decreasing surface activity) of fatty acid systems by removing the fatty acid salt from the interface.[172] Recall that surface tension and surface pressure (which we report here) are inversely related (i.e. high surface tension correlates with low surface pressure). Additionally, the removal of metal ions from fatty acid salts via titration with EDTA has shown the reverse effect. When the metal ion is removed, the surface tension decreases (increasing surface activity).[96]

The effect of additional equilibria on the measured surface pressure in the $[Ca^{2+}] \geq 10$ mM regime can be proposed to follow the consequences of Le Chatelier's principle as illustrated in the schematic of Fig. 5.6. If equilibrium is achieved at the metastable state corresponding to the maximum surface pressure, even if only for a brief amount of time, then any loss of material from the 2D monolayer into the aqueous phase via solubilization or precipitation of calcium palmitate must be counteracted by a shift in the equilibrium

from the 3D crystal phase to the 2D phase. If the rate of loss of the 2D monolayer is greater than the rate required to re-establish the 3D/2D equilibrium, then the surface pressure will not be able to be maintained. As there would be a constant replenishment of the 2D state from elution of molecules from the 3D crystals, the CH stretching modes of the monolayer would inevitably be present in the surface spectroscopies discussed earlier, which is what is observed in Fig. 5.4 and 5.5.

Non-Equilibrium Mechanically-Controlled Monolayer Relaxation

While the ESP determines the thermodynamic stability of spontaneously formed monolayers at the air-aqueous interface, other techniques have also been used to interpret monolayer stability in non-equilibrium systems at the interface. NER measurements involve compression of a spread monolayer to a target surface pressure or mean molecular area, followed by the maintenance of that target while monitoring the change in mean molecular area or surface pressure, respectively, with time. The change in the relative molecular area (A/A_0) with time has been shown to be useful in determining the relaxation mechanisms of monolayers at the air-water interface.[173-175] Here we have investigated the relative area response to constant surface pressures in systems of PA on water, 1 mM $CaCl_2$, and 300 mM $CaCl_2$ at 5 mN/m and 25 mN/m, which represent pressures above and below the ESP of the systems (when applicable). The chosen subphases represent PA systems with the lowest and highest ESP, and one with the most dramatic surface pressure decline after the establishment of a metastable state.

At a constant surface pressure of 5 mN/m, all systems exhibit minimal relative area loss (Fig. 5.7). This result was expected as 5 mN/m is below the ESP for all systems

studied. After 60 minutes, the water and 1 mM systems each exhibit only a small ~1% area loss. PA on a 300 mM $CaCl_2$ reaches a relative area of 0.98 after 60 minutes. With such minimal area losses at this surface pressure, the relaxation of all these systems is attributed to minor structural reorganization of the molecules at the interface.[156] Interestingly, the majority of the area loss in the 300 mM $CaCl_2$ system occurs within the first 2 minutes. During these experiments, when the target surface pressure is reached, the compression barriers slow down to 20% of their rate during isotherm compression. Upon this break in the compression speed,[168] the surface pressure of PA on 300 mM $CaCl_2$ drops from 5 mN/m to ~2.5 mN/m and the barriers must move further (thereby reducing the area) to accommodate for such a change in surface pressure. Once the surface pressure of 5 mN/m is recovered, the system remains very stable over time.

The same experiments were conducted at a target surface pressure of 25 mN/m, and revealed differences in the stability of PA on the three subphases. Much like the 5 mN/m scenario, the relaxation of PA on the 300 mM $CaCl_2$ subphase (Fig. 5.8c) follows a mechanism of structural rearrangement with minimal area loss (~3% at 60 minutes). Similar results have been demonstrated in the literature for stearic acid monolayers on high salt concentration solutions.[174] The largest change in area for this system can, again, be attributed to the initial drop in surface pressure upon slowing of the compression barriers. Throughout the period of relaxation, no appreciable changes are observed in the BAM images of the homogeneous monolayer film.

The rapid area loss observed for PA on water at a constant surface pressure of 25 mN/m (Fig. 5.8a) is indicative of a collapse-type relaxation mechanism, and the NER curve was fit to the Vollhardt model of nucleation and growth (eqn. (5.1)).[176] In this model, area

loss of the monolayer system is attributed to the formation (instantaneous or progressive) of nucleation centers and the geometric growth (hemispherical or cylindrical) of these centers by the uptake of insoluble monolayer material on the air side of the interface.

$$\frac{A_0 - A}{A_0 - A_\infty} = 1 - e^{-K_x t^x} \tag{5.1}$$

In this equation, A is the molecular area at a particular time (t), A_0 is the initial molecular area, A_∞ is the molecular area at infinite time, and K_x is the overall transformation rate constant. The time exponent, x, is characteristic of the nucleation mechanism and is the parameter used to identify the mechanism based on a fit of the constant surface pressure relaxation data. There are four values of x (1.5, 2, 2.5, 3) which have been specified by Vollhardt's model, each of which corresponds to a different nucleation and growth mechanism.[177]

While the values of A and A_0 are obtained directly from the experimental data, the value of A_∞ must be extrapolated from a fit of the NER curve.[178] Briefly, A/A_0 was plotted against the reciprocal of time ($1/t$) and a linear line of best fit was used to fit the initial portion of the resulting curve (Fig. 5.9). At $t \rightarrow \infty$, the y-intercept of the line of best fit represents A_∞/A_0, and from this, A_∞ can be determined. When fit to eqn. (5.1), the characteristic parameter, x, was found to be 1.9 ± 0.2. According to this value, at 25 mN/m, the relaxation of PA on a water subphase follows a mechanism of instantaneous nucleation with cylindrical edge growth ($x = 2$). This collapse-type relaxation mechanism can be visualized in the BAM images along the curve. Before the system reaches 25 mN/m during compression, small 3D aggregates are observed and can be seen in the BAM image at 0 minutes. As the system is maintained at 25 mN/m, the mechanism of nucleation and growth

can be observed by the formation of large 3D aggregates. Some of these aggregates can take up a majority of the field of view of the BAM image.

Of the three systems tested, the relaxation of PA on water exhibited the greatest variability in the NER curves. This can be attributed to several factors. The first of these possible factors is how well the mechanically controlled system is able to maintain a constant surface pressure of 25 mN/m. In some cases, material loss via nucleation and growth may occur too rapidly for the system to reestablish the 25 mN/m surface pressure by the slow rate of the barriers during the mechanical relaxation period. This can be seen in Fig. 5.10 where two extreme cases are shown; one that maintains the target surface pressure, and another during which the surface pressure starts to decrease after only about 6 minutes of control. Upon fitting, the system which is better able to maintain the target surface pressure gave a greater value of the characteristic parameter, *x*, than the system which was unable to recover from the loss of material to maintain the same surface pressure. The causes for surface pressure instability in the controlled surface pressure systems are numerous, and one may never be able to definitively assign such behavior to a single factor. Variables like small temperature and humidity fluctuations may impact the resulting stability or instability of the system.[179] Additionally, if dust particles, for example, land on the monolayer-covered surface, nucleation may be promoted more quickly than on a perfectly clean surface.

On the 1 mM $CaCl_2$ subphase, a different type of relaxation curve is observed from the other two systems (Fig. 5.8b). Here, PA experiences a relative area loss of ~10% after 100 minutes and exhibits a different shape than the relaxation curves obtained on 300 mM $CaCl_2$ or on water. The BAM images are more similar to those of the 300 mM $CaCl_2$ system

and do not change appreciably with time. The concave-up decay shape of the PA NER curve on this subphase would generally be fit to a two-step desorption mechanism (eqn. (5.2)).[180] The first step, dissolution ($K_1t^{1/2}$), describes the transfer of molecules from the monolayer into a subsurface region. After some time, this subsurface becomes saturated and molecules begin the process of diffusion (K_2t) into the bulk. K_1 and K_2 are the rate constants associated with the dissolution and diffusion processes, respectively.

$$\ln\left(\frac{A}{A_0}\right) = K_1 t^{1/2} + K_2 t \tag{5.2}$$

Due to nonlinearity in the 1 mM $CaCl_2$ data at small times plotted against $t^{1/2}$, an accurate fit to eqn. (5.2) cannot be obtained. When compared to other studies in the literature, this system exhibited minimal area loss than those experiments for which this fitting was successful.[181,182]

While the system did not exhibit significant and rapid area loss, indicating a collapse-type mechanism, such mechanisms can certainly contribute to the observed area loss because the held surface pressure (25 mN/m) is above that of the ESP of PA on 1 mM $CaCl_2$ (14.6 mN/m), at which there is an equilibrium of the 2D monolayer and 3D bulk material (i.e. collapse structures). Therefore, multiple loss mechanisms must be considered in the interpretation of the NER phenomena. To account for the possibility of monolayer collapse as a contributing factor to the observed area loss, we developed a new equation (eqn. (5.3)) to account for the possibility of both collapse and desorption.

$$\ln\left(\frac{A}{A_0}\right) = \ln\left(\left(1 - \frac{A_0 - A_\infty}{A_0}\right) + \left(\frac{A_0 - A_\infty}{A_0}\right)e^{-K_x t^x}\right) + K_1 t^{1/2} + K_2 t \tag{5.3}$$

This function is composed of the natural log of the Vollhardt equation (eqn. (5.1)), to capture loss due to collapse, and the dissolution and diffusion terms from eqn. (5.2). When applied to the NER curves of PA on 1 mM $CaCl_2$, there is excellent agreement ($R^2 > 0.99$) between the experimental data and eqn. (5.3). The values for the fitting parameters were found to be: $K_x = 0.010 \pm 0.003$ min^{-1} (overall collapse transformation rate constant; units depend on the value of x), $x = 1.1 \pm 0.1$ (nucleation and growth characteristic parameter), $K_1 = 0.0010 \pm 0.0005$ $min^{-1/2}$ (dissolution rate constant), and $K_2 = 0.000078 \pm 0.000078$ min^{-1} (diffusion rate constant). From a reasonable fit to this equation, one can say that the NER of PA on 1 mM $CaCl_2$ is likely due to a combination of collapse and desorption mechanisms occurring at surface pressures above the ESP. Recall that, as shown in the IRRAS spectra of Fig. 5.1a, at a 1 mM $CaCl_2$ concentration in the subphase, there exists both protonated and Ca^{2+}-bound deprotonated PA species in the monolayer. Such a mixed monolayer should experience a more complicated relaxation mechanism because the protonated and Ca^{2+}-bound PA molecules individually exhibit vastly different mechanisms.[183]

5.3.3 ESP vs. NER Stability

If one were to only examine monolayer NER at 25 mN/m to evaluate the stability of PA films on these three subphases, the conclusion would be that PA is the most stable on the 300 mM $CaCl_2$ subphase. However, from knowledge of the ESP measurements conducted in this work, such a statement would be misleading. One must then ask why mechanically controlled, non-equilibrium monolayer relaxation gives a differing view of

stability from ESP measurements. According to Gaines, at surface pressures above the monolayer stability limit, the surface pressure that is measured is the sum of two contributions: the thermodynamic term relating surface tensions ($\gamma_0 - \gamma_m$), and the pressure induced by the 2D compression forcing of the surfactant molecules together.[35] In a system like PA on 300 mM $CaCl_2$, this second compression force likely dominates at all points along the compression isotherm up to and including the maintained surface pressure of 25 mN/m, and the entire system can be considered metastable.[156] Unlike ESP measurements, "stability" in a non-equilibrium system, such as monolayer relaxation, refers to the expulsion of material from the monolayer (collapse aggregates or dissolution), not the achievement of the thermodynamically favorable state. Such designations are quite important as one can interpret stability very differently between ESP and NER measurements, as shown here for the example PA systems on water, 1 mM, and 300 mM $CaCl_2$.

5.4 Conclusions

In this work, the binding of Ca^{2+} ions to the carboxylic acid headgroup of PA monolayers, and the effects of such binding on monolayer stability were evaluated with surface-sensitive spectroscopies, Brewster angle microscopy, and surface tensiometry techniques. From IRRAS spectra of the spread monolayers, it was found that the extent of deprotonation via Ca^{2+} binding became more prevalent with increasing concentration, but the 2D hexagonal lattice packing of the PA monolayers was independent of Ca^{2+} concentration. While the common marker for binding motif, $\Delta\nu_{AS-S}$, remained constant at

approximately 132 cm^{-1}, indicating ionic binding, the extent of hydration within this complexation changes with concentration.

Langmuir compression monolayers are often used as proxies for the organic films at the interface of SSA to represent the various phases associated with 2D monolayer concentration. However, they are approximating different aerosol environments as both compression isotherms and relaxation measurements push molecules through non-equilibrium states. In this work, we investigated equilibrium systems with ESP measurements to model ambient conditions that are relatively constant where aerosol films may be allowed to partition and spread to favorable states. Conversely, we utilized mechanically-controlled monolayer NER methods to see how interfacial aerosol films would respond to non-equilibrium conditions, representing the possible conditions of more dynamic air masses.

The ESPs of PA exhibited two different trends in the low (≤ 1 mM) and high (≥ 10 mM) Ca^{2+} concentration regimes, representing proxies of calcium-depleted or –enriched aerosols in high and low relative humidity constant ambient environments, respectively. At Ca^{2+} concentrations below 10 mM, thermodynamic equilibrium was achieved via spontaneous monolayer formation, and the value ESP increased with Ca^{2+} concentration. At concentrations of 10 mM and greater, such an equilibrium was not obtained and upon reaching a metastable state, surface pressures decreased with time. This decrease is attributed to the relaxation of the monolayer into a more favorable state, and/or to the effects of removal of the 2D monolayer into the bulk aqueous phase. Although for the high concentration of 300 mM $CaCl_2$, the surface pressure reached 0 mN/m, spectroscopic evidence revealed that there still exists a monolayer film at the interface.

Monolayer NER experiments conducted at mechanically-controlled surface pressures above and below the measured ESP values revealed that all monolayers of PA could be considered stable against material loss at low surface pressures, but the monolayer systems exhibited different relaxation mechanisms at high surface pressures. On water, PA relaxed with significant area losses via a mechanism of nucleation and growth into large 3D collapse aggregates, but on 1 mM $CaCl_2$ the monolayer exhibited a more complex mechanism which likely contained both collapse and dissolution relaxation processes.

Interestingly, on 300 mM $CaCl_2$, PA would be considered the most stable from a NER perspective. However, the ESP data reveals that this Ca^{2+} concentration produced the least thermodynamically stable PA system. This suggests that the stability against material loss exhibited in the non-equilibrium relaxation experiments on 300 mM $CaCl_2$ is likely a consequence of the mechanical compression force on the monolayer in the Langmuir trough. Therefore, ion-bound monolayer stability phenomena should be investigated with multiple techniques, representing equilibrium and non-equilibrium states, to be better understood.

The results presented here suggest that it is reasonable to assume that Ca^{2+} enrichment in SSA is linked to organic complexation. Additionally, the aerosol-atmosphere interface will be affected by the Ca^{2+} ions bound to lipid molecules, and water accumulation or loss (resulting in concentration ranges of Ca^{2+}) leads to changes in the thermodynamic and non-equilibrium stability of the interfacial organic film in both constant and dynamic ambient environments.

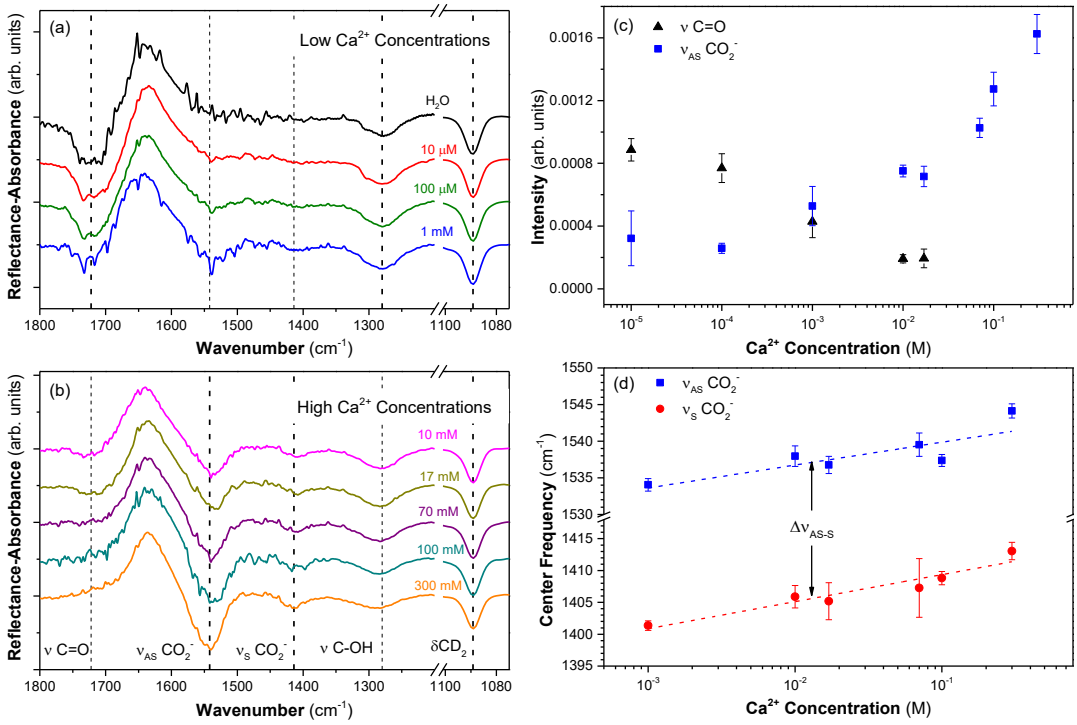

Figure 5.1. IRRAS spectra of d_{31}-PA monolayers (20.5 Å^2/molecule) on $CaCl_2$ subphases of (a) low Ca^{2+} concentration ($0 \leq [Ca^{2+}] \leq 1$ mM) and (b) high Ca^{2+} concentration ($10 \leq [Ca^{2+}] \leq 300$ mM). Dashed lines are drawn to guide the eye at 1722 cm^{-1} (ν C=O), 1542 cm^{-1} (ν_{AS} CO_2^-), 1414 cm^{-1} (ν_S CO_2^-), 1280 cm^{-1} (ν C-OH), and 1089 cm^{-1} (δ CD_2). The intensities of the C=O (black triangles) and ν_{AS} CO_2^- (blue squares) stretches as a function of Ca^{2+} concentration are shown in (c) and are indicators of the protonation state of the PA molecules in the monolayer. In (d), the center frequency of the ν_{as} CO_2^- (blue squares) and ν_s CO_2^- (red circles) stretches are shown as a function of Ca^{2+} concentration in the aqueous subphase. The splitting of the CO_2^- modes ($\Delta\nu_{AS-S}$) is determined by taking the difference of the frequencies of the asymmetric and symmetric stretches, and is relatively constant with Ca^{2+} concentration. The intensities and frequencies in (c) and (d) are determined from Gaussian fits of the individual vibrational modes.

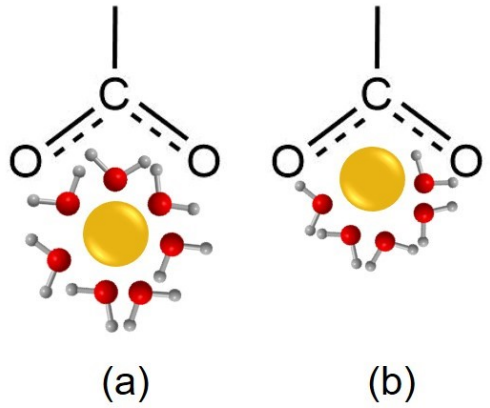

Figure 5.2. Schematic of the ionic binding motif of a Ca^{2+} ion to the carboxylic acid headgroup of PA to illustrate (a) more and (b) less hydrated environments.

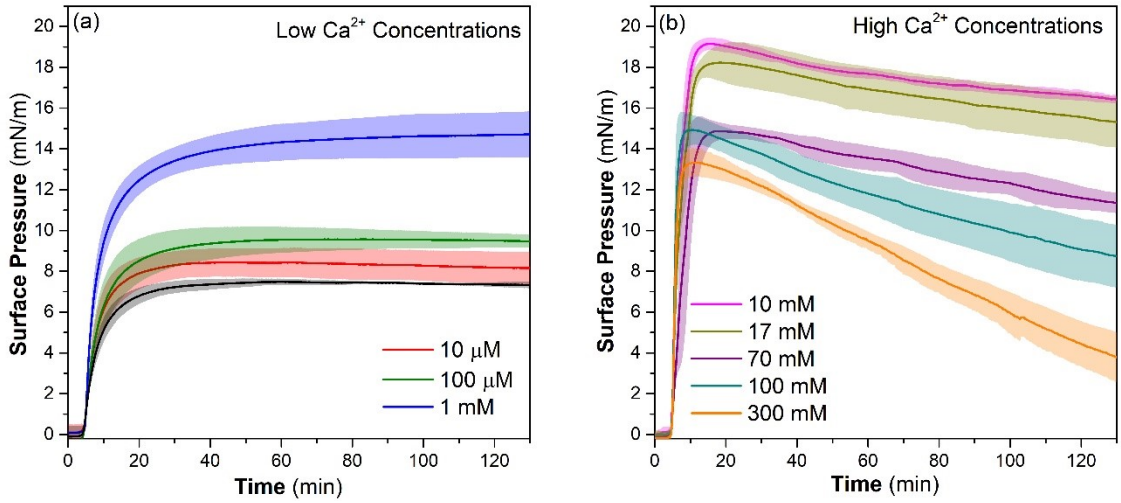

Figure 5.3. Time evolution of surface pressure ESP curves of PA on $CaCl_2$ subphases of (a) low Ca^{2+} concentration ($0 \leq [Ca^{2+}] \leq 1$ mM), and (b) high Ca^{2+} concentration ($10 \leq [Ca^{2+}] \leq 300$ mM). Recall that oceanic $[Ca^{2+}]$ in bulk seawater is 10 mM. The time axis has been scaled such that the time prior to the surface pressure rise is constant among the trials. This time is not significant to the final ESP result, varies between experiments, and may be due to variations in the amount of crystals spread on the sample surface. All curves represent the average of at least three individual trials. The shaded regions around the curves shown in (a) and (b) represent ± one standard deviation from the average.

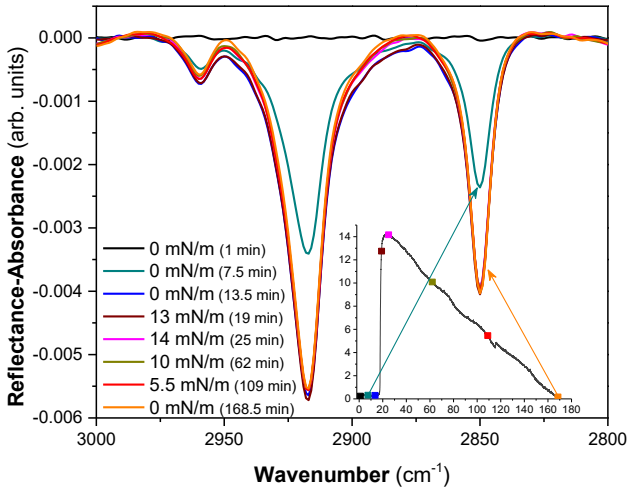

Figure 5.4. IRRAS spectra in the CH stretching region of PA on 300 mM $CaCl_2$ during the course of the surface pressure decline of an ESP measurement. The intensity of the CH stretching modes remains largely unchanged despite the surface pressure decline. The inset shows the surface pressure vs. time ESP curve associated with the spectra (markers on the curve correspond to the colored spectra).

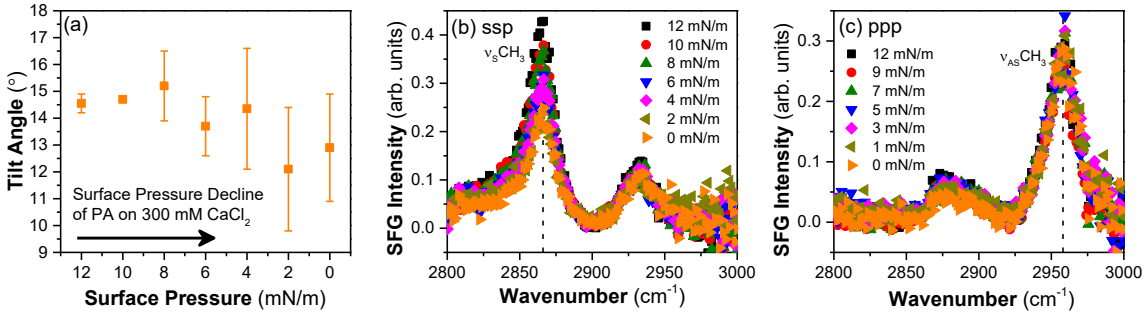

Figure 5.5. (a) Tilt angle of the PA chains as a function of surface pressure during the surface pressure decline of an ESP measurement of PA on 300 mM $CaCl_2$. The tilt angle is calculated from the intensity of the symmetric (ν_S) and asymmetric (ν_{AS}) stretching modes of the CH_3 group in (b) *ssp* and (c) *ppp* polarizations, respectively.

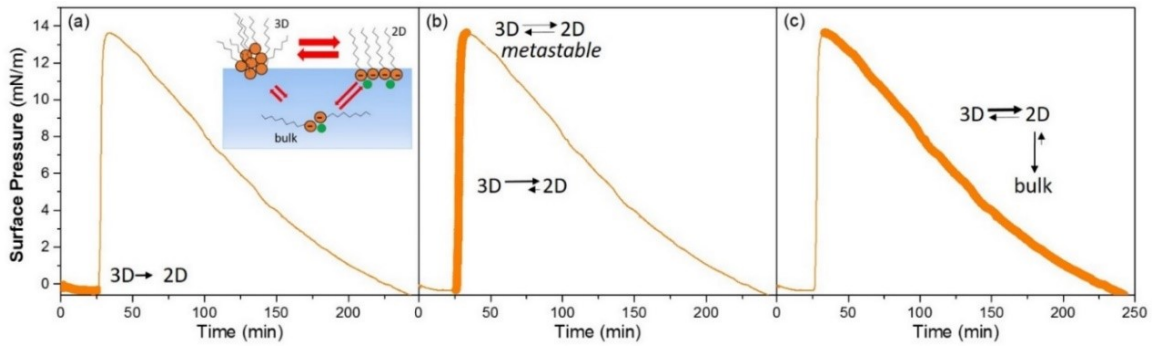

Figure 5.6. Schematic of the proposed equilibria during an ESP experiment of PA on 300 mM $CaCl_2$ (equilibria to the vapor phase is omitted). The dominant equilibria are shown in each panel: (a) elution of PA molecules from the 3D crystal into the 2D film, (b) continued elution of PA molecules from 3D to 2D film followed by a brief metastable state when equilibrium is established between the 2D and 3D states, (c) removal of the 2D calcium palmitate film into the bulk must be counteracted by a shift in the 3D/2D equilibrium toward the 2D monolayer.

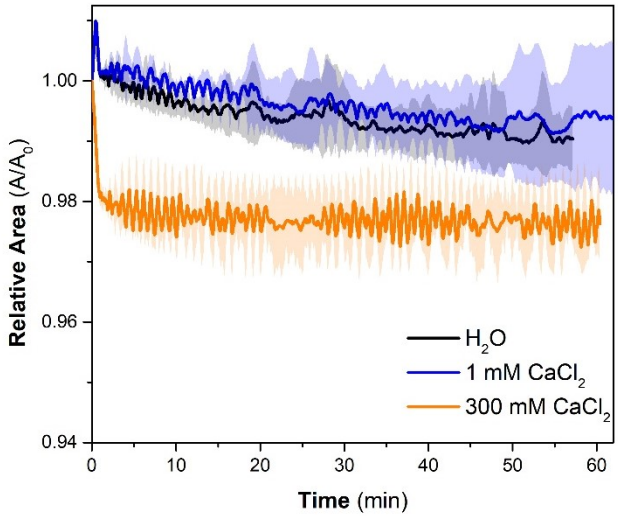

Figure 5.7. Monolayer NER curves of PA maintained at a constant surface pressure of 5 mN/m on water (black), 1 mM $CaCl_2$ (blue), and 300 mM $CaCl_2$ (orange). Curves shown are the average of at least three measurements. The shaded regions around the curves represent ± one standard deviation from the average of three trials.

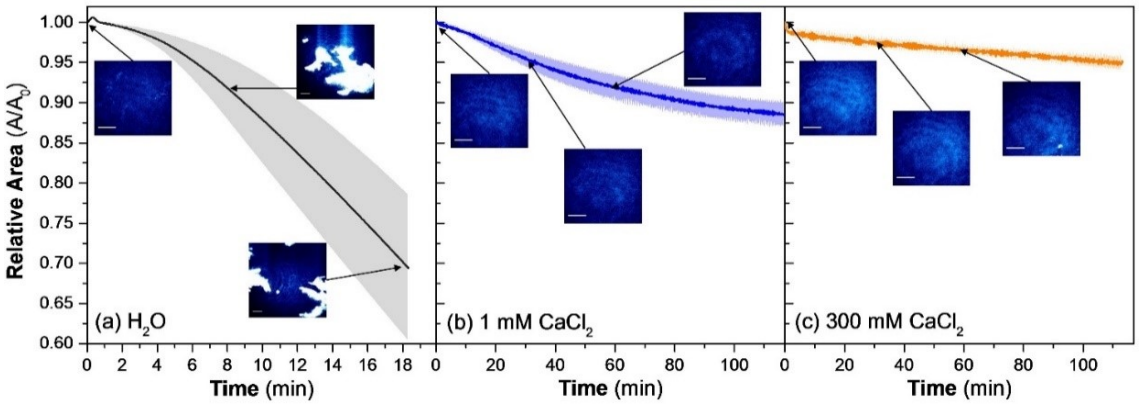

Figure 5.8. Monolayer NER curves of PA maintained at a constant surface pressure of 25 mN/m on (a) water, (b) 1 mM $CaCl_2$, and (c) 300 mM $CaCl_2$. Curves shown are the average of at least three measurements. The shaded regions around the curves represent ± one standard deviation from the average of at least three trials. BAM images are shown along the curves at the times at which they were captured during the relaxation process. All scale bars in BAM images represent a length of 100 µm. The surface morphology of PA on 1 mM and 300 mM $CaCl_2$ subphases remains homogeneous as a condensed film throughout the relaxation period. PA on water, however, exhibits a relaxation mechanism of nucleation and growth as evidenced by the large collapse structures. Because there is a limited field of view in BAM imaging, the time at which the large 3D structures are viewed for PA on water is not necessarily reproducible. The images in (a) are from multiple trials.

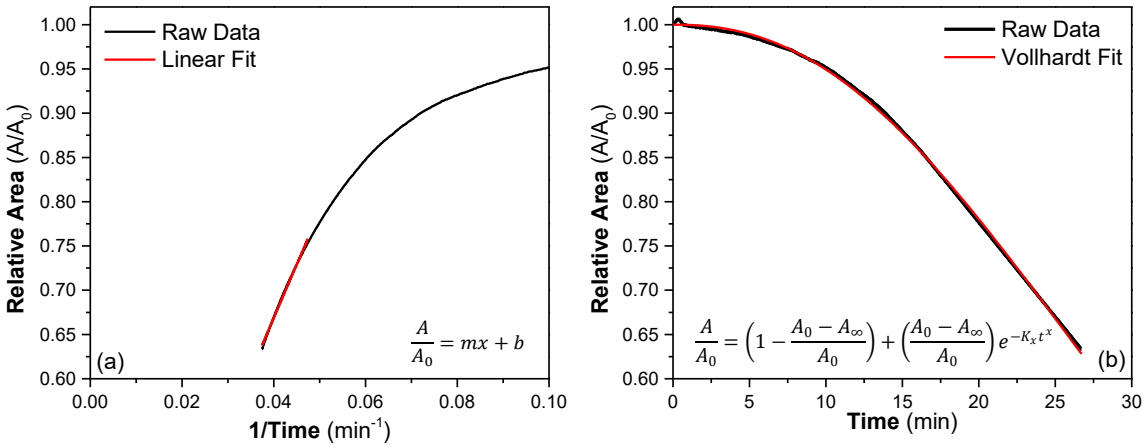

Figure 5.9. (a) Vollhardt fitting of PA monolayers at 25 mN/m on a water subphase. The linear fit of that data against the reciprocal of time in (a) is used to calculate the necessary A_∞ value for the fitting function in (b).

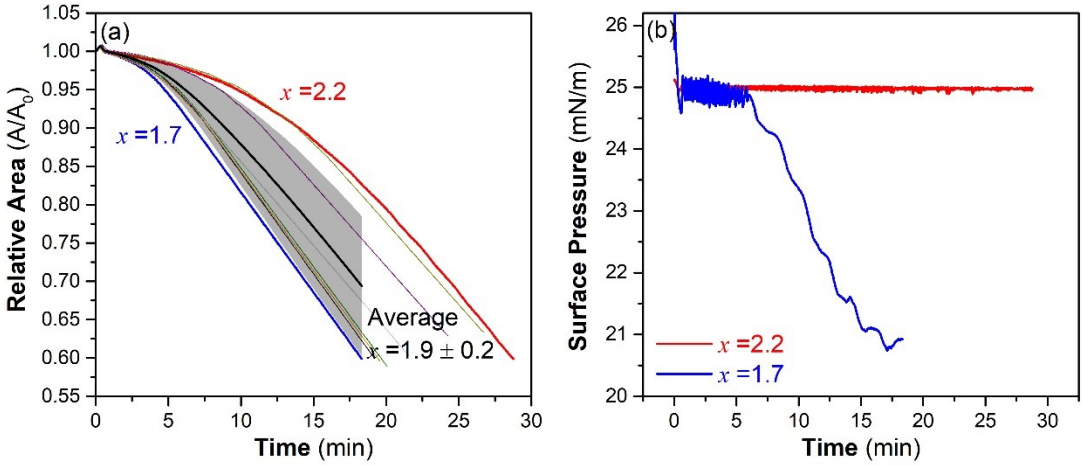

Figure 5.10. Variability in constant pressure relaxation of PA on water at 25 mN/m. The ability of the system to maintain a 25 mN/m surface pressure affects the relative area vs. time curve, and thus the characteristic parameter, *x*.

Table 5.1. Equilibrium spreading pressures of PA on $CaCl_2$ subphases up to 1 mM.

$[Ca^{2+}]$	ESP (mN/m)
0	7.5 ± 0.1
10 μM	8.4 ± 0.6
100 μM	9.6 ± 0.5
1 mM	14.6 ± 0.9

Table 5.2. Maximum surface pressure attained and the rate of surface pressure change after this metastable state during ESP measurements of PA on $CaCl_2$ subphases with concentrations of Ca^{2+} between 10 mM and 300 mM.

$[Ca^{2+}]$	Maximum Π (mN/m)	Change in Π ((mN/m)/min)
10 mM	19.2 ± 0.2	-0.013 ± 0.001
17 mM	18.4 ± 0.7	-0.014 ± 0.002
70 mM	15.0 ± 0.4	-0.030 ± 0.004
100 mM	15.0 ± 0.6	-0.040 ± 0.005
300 mM	13.4 ± 0.6	-0.069 ± 0.018

Chapter 6: Conclusions and Atmospheric Implications

The presented studies of simple fatty acid interfacial systems were motivated by the ever complex chemistry that occurs at the aerosol-atmosphere interface. It is of great interest to further understand and interpret the effects that organic films have on the properties of SSA. Here we have isolated the model systems studied to those of fatty acids, which are the most commonly identified species on SSA and in the SSML, as a necessary first step in the understanding of complex atmospheric interfaces.

Though far less studied in the aerosol community than long-chain palmitic and stearic acids, medium-chain (C_8-C_{10}) fatty acids were investigated here in part due to their semi-soluble nature. The surface-pK_a of these fatty acids were quantified with a simple surface tension titration technique and interpreted within the context of the large array of, somewhat controversial, pK_a data available in the literature. The values determined in this study differ from the bulk pK_a of the carboxylic acids, which are often used in the literature to assess speciation at the interface of atmospheric systems. The protonation state of fatty acids affects their surface activity, which can then impact the climate-relevant properties of SSA. With new, surface-specific, values of pK_a, understanding of charge and surface activity of semi-soluble organic components can be better understood within the context of aerosol chemistry.

In addition to the quantification of surface-pK_a for medium-chain fatty acids, the role of pH on the surface structure associated with PA monolayers was also investigated in this work. Under two selected pH conditions, the monolayers existed as either fully protonated PA or as a 50/50 mixture of PA and palmitate. Utilizing IRRAS and ESP measurements, it was shown that under both pH conditions, monolayers packed in hexagonal lattices and that ESP increased primarily due to electrostatic repulsions in the mixed monolayer system. VSFG spectroscopy and surface potential measurements revealed changes in the overall structure of the interfacial water associated with these monolayer systems. As SSA will undergo pH changes as they age in the atmosphere, these results extend to the understanding of the effects that such changes may have on the structure of the interface.

Finally, the associations between Ca^{2+} ions and PA monolayers was investigated utilizing primarily IRRAS, ESP, and NER methods. IRRAS measurements demonstrated that Ca^{2+}-induced deprotonation of the carboxylic acid headgroup of PA was evident even at low concentrations of Ca^{2+} in the subphase. From these results, it can be suggested that the driving force of Ca^{2+} enrichment in the aerosol phase is due to its strong association to the headgroup of fatty acids, which are selectively transferred to SSA. The effects of Ca^{2+}:PA complexation on the stability of the monolayer films was evaluated in both thermodynamic and non-equilibrium systems. While PA monolayers did not achieve thermodynamic equilibrium at $Ca^{2+} \geq 10$ mM, they exhibited high stability in the NER measurements of PA on 300 mM $CaCl_2$ subphases.

The monolayer stability measurements conducted in this work for PA monolayers not only serve to inform understanding of stability phenomena from a fundamental

perspective, but can also be extended to various aerosol environments. ESP measurements can represent SSA in relatively constant ambient conditions where fluctuations in molecular area due to the water uptake or evaporation of the aqueous core are minimal. Conversely, one could consider the monolayer behavior in NER measurements to be more related to highly dynamic air masses where perturbations of aerosol size would be prevalent. Studies of ESP and NER can provide stability parameters to be incorporated into aerosol climate models to better predict the influence of SSA on the chemistry of the atmosphere.

Overall, the results presented in this dissertation have demonstrated new developments in the understanding of various surface properties of fatty acid interfacial systems including surface-pK_a, lattice packing, water structure, surface stability, and ion-carboxylate binding. Though the systems studied represent idealized, simple proxies of SSA and the SSML, the knowledge gained and techniques utilized for their study can be extended to increasingly chemically complex proxy, and real, systems to further our understanding of atmospheric chemistry. Additionally, in recent years, global climate models have begun incorporating the properties of insoluble surfactant molecules in their descriptions of SSA. While these integrations primarily rely on simple Langmuir adsorption isotherms, it can be projected that these models will soon incorporate more molecular-level details (i.e. pK_a, surfactant orientation, ESP) to better describe the structure of these organics at the aerosol-atmosphere interface.[116,117]

REFERENCES

1. O. Boucher, D. Randall, P. Artaxo, C. Bretherton, G. Feingold, P. Forster, V.-M. Kerminen, Y. Kondo, H. Liao, U. Lohmann. Clouds and Aerosols. In: Stocker TF, Qin D, Plattner G-K, Tignor M, Allen SK, Boschung J, et al., editors. Climate Change 2013: The Physical Science Basis. Contribution of Working Group I to the Fifth Assessment Report of the Intergovernmental Panel on Climate Change. New York, NY, USA: Cambridge University Press; 2013.
2. B. J. Finlayson-Pitts, J. N. Pitts Jr., *Chemistry of the Upper and Lower Atmosphere*. Academic Press, San Diego, 2000.
3. P. S. Liss, R. A. Duce, *The sea surface and global change*. Cambridge University Press, Cambridge ; New York, 1997.
4. Z. B. Zhang, L. S. Liu, C. Y. Liu, W. J. Cai, *J. Colloid Interface Sci.*, 2003, **264**, 148-159.
5. M. Cunliffe, R. C. Upstill-Goddard, J. C. Murrell, *Fems Microbiol Rev*, 2011, **35**, 233-246.
6. M. Cunliffe, A. Engel, S. Frka, B. Gasparovic, C. Guitart, J. C. Murrell, M. Salter, C. Stolle, R. Upstill-Goddard, O. Wurl, *Prog. Oceanogr.*, 2013, **109**, 104-116.
7. B. Gasparovic, M. Plavsic, B. Cosovic, A. Saliot, *Mar. Chem.*, 2007, **105**, 1-14.
8. R. S. Tseng, J. T. Viechnicki, R. A. Skop, J. W. Brown, *J. Geophys. Res.: Oceans*, 1992, **97**, 5201-5206.
9. D. C. Blanchard, L. D. Syzdek, *J. Geophys. Res.: Oceans*, 1988, **93**, 3649-3654.
10. R. E. Cochran, T. Jayarathne, E. A. Stone, V. H. Grassian, *J. Phys. Chem. Lett.*, 2016, **7**, 1692-1696.
11. R. N. Roslan, N. M. Hanif, M. R. Othman, W. N. F. W. Azmi, X. X. Yan, M. M. Ali, C. A. R. Mohamed, M. T. Latif, *Mar. Pollut. Bull.*, 2010, **60**, 1584-1590.
12. R. E. Cochran, O. Laskina, T. Jayarathne, A. Laskin, J. Laskin, P. Lin, C. Sultana, C. Lee, K. A. Moore, C. D. Cappa, T. H. Bertram, K. A. Prather, V. H. Grassian, E. A. Stone, *Environ. Sci. Technol.*, 2016, **50**, 2477-2486.
13. G. B. Ellison, A. F. Tuck, V. Vaida, *J. Geophys. Res.: Atmos.*, 1999, **104**, 11633-11641.
14. H. Tervahattu, K. Hartonen, V. M. Kerminen, K. Kupiainen, P. Aarnio, T. Koskentalo, A. F. Tuck, V. Vaida, *J. Geophys. Res.: Atmos.*, 2002, **107**, 4053.
15. M. Mochida, Y. Kitamori, K. Kawamura, Y. Nojiri, K. Suzuki, *J. Geophys. Res.: Atmos.*, 2002, **107**, 4325.
16. R. E. Cochran, O. Laskina, J. V. Trueblood, A. D. Estillore, H. S. Morris, T. Jayarathne, C. M. Sultana, C. Lee, P. Lin, J. Laskin, A. Laskin, J. A. Dowling, Z. Qin, C. D. Cappa, T. H. Bertram, A. V. Tivanski, E. A. Stone, K. A. Prather, V. H. Grassian, *Chem*, 2017, **2**, 655-667.
17. D. J. Donaldson, C. George, *Environ. Sci. Technol.*, 2012, **46**, 10385-10389.
18. D. J. Donaldson, V. Vaida, *Chem. Rev.*, 2006, **106**, 1445-1461.
19. A. Rouviere, M. Ammann, *Atmospheric Chemistry and Physics*, 2010, **10**, 11489-11500.

20. O. S. Ryder, N. R. Campbell, M. Shaloski, H. Al-Mashat, G. M. Nathanson, T. H. Bertram, *J. Phys. Chem. A*, 2015, **119**, 8519-8526.
21. M. A. Shaloski, T. B. Sobyra, G. M. Nathanson, *J. Phys. Chem. A*, 2015, **119**, 12357-12366.
22. D. J. Losey, R. G. Parker, M. A. Freedman, *J. Phys. Chem. Lett.*, 2016, **7**, 3861-3865.
23. C. R. Ruehl, J. F. Davies, K. R. Wilson, *Science*, 2016, **351**, 1447-1450.
24. J. F. Davies, R. E. H. Miles, A. E. Haddrell, J. P. Reid, *Proc. Natl. Acad. Sci. U. S. A.*, 2013, **110**, 8807-8812.
25. A. A. Frossard, W. Li, V. Gérard, B. Nozière, R. C. Cohen, *Aerosol Sci. Technol.*, 2018, 1-11.
26. R. M. Garland, M. E. Wise, M. R. Beaver, H. L. DeWitt, A. C. Aiken, J. L. Jimenez, M. A. Tolbert, *Atmospheric Chemistry and Physics*, 2005, **5**, 1951-1961.
27. C. S. McCluskey, T. C. J. Hill, F. Malfatti, C. M. Sultana, C. Lee, M. V. Santander, C. M. Beall, K. A. Moore, G. C. Cornwell, D. B. Collins, K. A. Prather, T. Jayarathne, E. A. Stone, F. Azam, S. M. Kreidenweis, P. J. DeMott, *J. Atmos. Sci.*, 2017, **74**, 151-166.
28. Y. Q. Qiu, N. Odendahl, A. Hudait, R. Mason, A. K. Bertram, F. Paesani, P. J. DeMott, V. Molinero, *J. Am. Chem. Soc.*, 2017, **139**, 3052-3064.
29. F. J. Millero, *Chemical Oceanography*, 3rd ed. CRC Press, Boca Raton, 2006.
30. A. M. Fridlind, M. Z. Jacobson, *J. Geophys. Res.: Atmos.*, 2000, **105**, 17325-17340.
31. W. C. Keene, A. A. P. Pszenny, J. R. Maben, E. Stevenson, A. Wall, *J. Geophys. Res.: Atmos.*, 2004, **109**, D23307.
32. W. C. Keene, R. Sander, A. A. P. Pszenny, R. Vogt, P. J. Crutzen, J. N. Galloway, *J. Aerosol Sci.*, 1998, **29**, 339-356.
33. T. Jayarathne, C. M. Sultana, C. Lee, F. Malfatti, J. L. Cox, M. A. Pendergraft, K. A. Moore, F. Azam, A. V. Tivanski, C. D. Cappa, T. H. Bertram, V. H. Grassian, K. A. Prather, E. A. Stone, *Environ. Sci. Technol.*, 2016, **50**, 11511-11520.
34. M. E. Salter, E. Hamacher-Barth, C. Leck, J. Werner, C. M. Johnson, I. Riipinen, E. D. Nilsson, P. Zieger, *Geophys. Res. Lett.*, 2016, **43**, 8277-8285.
35. G. L. Gaines, *Insoluble monolayers at liquid-gas interfaces*. Interscience Publishers, 1966.
36. R. D. Smith, J. C. Berg, *J. Colloid Interface Sci.*, 1980, **74**, 273-286.
37. A. Marchand, J. H. Weijs, J. H. Snoeijer, B. Andreotti, *American Journal of Physics*, 2011, **79**, 999-1008.
38. H.-J. Butt, K. Graf, M. Kappl, *Physics and Chemistry of Interfaces*. Wiley-VCH, Weinheim, 2013.
39. G. Barnes, I. Gentle, *Interfacial science : an introduction*, 2nd ed. Oxford University Press, Oxford ; New York, 2011.
40. K. Holmberg, D. O. Shah, M. J. Schwuger, *Handbook of Applied Surface and Colloid Chemistry*. Wiley, New York, 2002.
41. M. C. Petty, *Langmuir-Blodgett films : an introduction*. Cambridge University Press, Cambridge ; New York, 1996.
42. B. A. Wellen, E. A. Lach, H. C. Allen, *Phys. Chem. Chem. Phys.*, 2017, **19**, 26551-26558.

43. M. Iwahashi, N. Maehara, Y. Kaneko, T. Seimiya, S. R. Middleton, N. R. Pallas, B. A. Pethica, *J. Chem. Soc., Faraday Trans.*, 1985, **81**, 973-981.
44. J. M. R. Patino, R. M. M. Martinez, *J. Colloid Interface Sci.*, 1994, **167**, 150-158.
45. A. W. Snow, G. G. Jernigan, M. G. Ancona, *Thin Solid Films*, 2014, **556**, 475-484.
46. M. N. Tsuji, H.; Moroi, Y.; Shibata, O., *J. Colloid Interface Sci.*, 2008, **318**, 322-330.
47. V. G. Bordo, H. G. Rubahn, *Optics and spectroscopy at surfaces and interfaces*. Wiley-VCH, Weinheim, 2005.
48. R. Mendelsohn, J. W. Brauner, A. Gericke, *Annu. Rev. Phys. Chem.*, 1995, **46**, 305-334.
49. E. M. Adams, H. C. Allen, *Atmosphere*, 2013, **4**, 315-336.
50. E. M. Adams, C. B. Casper, H. C. Allen, *J. Colloid Interface Sci.*, 2016, **478**, 353-364.
51. E. M. Adams, D. Verreault, T. Jayarathne, R. E. Cochran, E. A. Stone, H. C. Allen, *Phys. Chem. Chem. Phys.*, 2016, **18**, 32345-32357.
52. C. B. Casper, D. Verreault, E. M. Adams, W. Hua, H. C. Allen, *J. Phys. Chem. B*, 2016, **120**, 2043-2052.
53. R. Mendelsohn, C. R. Flach. Infrared Reflection – Absorption Spectrometry of Monolayer Films at the Air – Water Interface. Handbook of Vibrational Spectroscopy: John Wiley & Sons, Ltd; 2006.
54. C. R. Flach, A. Gericke, R. Mendelsohn, *J. Phys. Chem. B*, 1997, **101**, 58-65.
55. R. Mendelsohn, G. R. Mao, C. R. Flach, *Biochim. Biophys. Acta, Biomembr.*, 2010, **1798**, 788-800.
56. A. Gericke, A. V. Michailov, H. Huhnerfuss, *Vib. Spectrosc.*, 1993, **4**, 335-348.
57. A. G. Lambert, P. B. Davies, D. J. Neivandt, *Appl. Spectrosc. Rev.*, 2005, **40**, 103-145.
58. R. W. Boyd, *Nonlinear optics*, 3rd ed. Academic Press, Amsterdam ; Boston, 2008.
59. A. M. Jubb, W. Hua, H. C. Allen, *Annual Review of Physical Chemistry, Vol 63*, 2012, **63**, 107-130.
60. D. Verreault, W. Hua, H. C. Allen, *The Journal of Physical Chemistry Letters*, 2012, **3**, 3012-3028.
61. H. F. Wang, W. Gan, R. Lu, Y. Rao, B. H. Wu, *Int. Rev. Phys. Chem.*, 2005, **24**, 191-256.
62. E. M. Adams, B. A. Wellen, R. Thiraux, S. K. Reddy, A. S. Vidalis, F. Paesani, H. C. Allen, *Phys. Chem. Chem. Phys.*, 2017, **19**, 10481-10490.
63. S. K. Reddy, R. Thiraux, B. A. Wellen Rudd, L. Lin, T. Adel, F. M. Geiger, H. C. Allen, A. Morita, F. Paesani, *Chem*, 2018, submitted.
64. K. B. Eisenthal, *Chem. Rev.*, 1996, **96**, 1343-1360.
65. J. R. Kanicky, A. F. Poniatowski, N. R. Mehta, D. O. Shah, *Langmuir*, 2000, **16**, 172-177.
66. E. C. Griffith, V. Vaida, *J. Am. Chem. Soc.*, 2013, **135**, 710-716.
67. H. F. Wang, X. L. Zhao, K. B. Eisenthal, *J. Phys. Chem. B*, 2000, **104**, 8855-8861.
68. X. L. Zhao, S. W. Ong, H. F. Wang, K. B. Eisenthal, *Chem. Phys. Lett.*, 1993, **214**, 203-207.
69. M. P. Andersson, M. H. M. Olsson, S. L. S. Stipp, *Langmuir*, 2014, **30**, 6437-6445.

70. D. P. Cistola, J. A. Hamilton, D. Jackson, D. M. Small, *Biochemistry*, 1988, **27**, 1881-1888.
71. C. J. Drummond, F. Grieser, T. W. Healy, *J. Chem. Soc., Faraday Trans.*, 1989, **85**, 521-535.
72. C. R. Whiddon, C. A. Bunton, O. Soderman, *J. Phys. Chem. B*, 2003, **107**, 1001-1005.
73. D. S. McLean, D. Vercoe, K. R. Stack, D. Richardson, *Appita J.*, 2005, **58**, 362-366.
74. R. Ciuraru, L. Fine, M. van Pinxteren, B. D'Anna, H. Herrmann, C. George, *Sci. Rep.*, 2015, **5**, 12741.
75. W. M. Haynes, D. R. Lide, *CRC handbook of chemistry and physics : a ready-reference book of chemical and physical data*. CRC Press, Boca Raton, 2011.
76. A. W. Ralston, C. W. Hoerr, *J. Org. Chem.*, 1942, **7**, 546-555.
77. P. Mukerjee, K. J. Mysels, *Critical Micelle Concentrations in Aqueous Surfactant Systems*. National Bureau of Standards, NSRDS-NBS 36, Washington, D. C., 1971.
78. F. Kamp, H. V. Westerhoff, J. A. Hamilton, *Biochemistry*, 1993, **32**, 11074-11086.
79. R. Schmidt, U. Meier, M. Yabut-Perez, D. Walmrath, F. Grimminger, W. Seeger, A. Gunther, *Am. J. Resp. Crit. Care*, 2001, **163**, 95-100.
80. E. Sparr, L. Eriksson, J. A. Bouwstra, K. Ekelund, *Langmuir*, 2001, **17**, 164-172.
81. R. C. Guimaraes, A. C. Araujo, A. E. C. Peres, *Miner. Eng.*, 2005, **18**, 199-204.
82. K. H. Rao, K. S. E. Forssberg, *Miner. Eng.*, 1991, **4**, 879-890.
83. D. J. McClements, E. A. Decker, *J. Food. Sci.*, 2000, **65**, 1270-1282.
84. H. T. Osborn, C. C. Akoh, *Food Chem.*, 2004, **84**, 451-456.
85. T. Waraho, D. J. McClements, E. A. Decker, *Food Chem.*, 2011, **129**, 854-859.
86. E. Gonzalez-Labrada, R. Schmidt, C. E. DeWolf, *Phys. Chem. Chem. Phys.*, 2007, **9**, 5814-5821.
87. M. D. King, A. R. Rennie, K. C. Thompson, F. N. Fisher, C. C. Dong, R. K. Thomas, C. Pfrang, A. V. Hughes, *Phys. Chem. Chem. Phys.*, 2009, **11**, 7699-7707.
88. A. K. Y. Lee, C. K. Chan, *Atmos. Environ.*, 2007, **41**, 4611-4621.
89. L. F. Voss, M. F. Bazerbashi, C. P. Beekman, C. M. Hadad, H. C. Allen, *J. Geophys. Res.: Atmos.*, 2007, **112**, D06209.
90. K. Stemmler, A. Vlasenko, C. Guimbaud, M. Ammann, *Atmospheric Chemistry and Physics*, 2008, **8**, 5127-5141.
91. W. D. Garrett, *J. Atmos. Sci.*, 1971, **28**, 816-819.
92. C. Pilinis, S. N. Pandis, J. H. Seinfeld, *J. Geophys. Res.: Atmos.*, 1995, **100**, 18739-18754.
93. C. A. Randles, L. M. Russell, V. Ramaswamy, *Geophys. Res. Lett.*, 2004, **31**, L16108.
94. M. Bilde, B. Svenningsson, *Tellus B.*, 2004, **56**, 128-134.
95. B. N. Dickhaus, R. Priefer, *Colloids Surf., A*, 2016, **488**, 15-19.
96. M. Sugawara, K. Isazawa, T. Kambara, *Fresenius Z. Anal. Chem.*, 1981, **308**, 17-20.
97. K. D. Danov, P. A. Kralchevsky, K. P. Ananthapadmanabblan, A. Lips, *J. Colloid Interface Sci.*, 2006, **300**, 809-813.
98. P. D. Cratin, *J. Disper. Sci. Technol.*, 1993, **14**, 559-602.

99. M. Egret-Charlier, A. Sanson, M. Ptak, O. Bouloussa, *Febs Lett.*, 1978, **89**, 313-316.
100. N. L. Prisle, N. Ottosson, G. Öhrwall, J. Söderström, M. Dal Maso, O. Björneholm, *Atmospheric Chemistry and Physics*, 2012, **12**, 12227-12242.
101. R. Aveyard, B. P. Binks, N. Carr, A. W. Cross, *Thin Solid Films*, 1990, **188**, 361-373.
102. J. Glazer, M. Z. Dogan, *Trans. Faraday Soc.*, 1953, **49**, 448-455.
103. D. C. Harris, *Quantitative Chemical Analysis*, 3rd ed. W. H. Freeman and Company, New York, 1991.
104. J. R. Kanicky, D. O. Shah, *Langmuir*, 2003, **19**, 2034-2038.
105. A. Atrafi, M. Pawlik, *Miner. Eng.*, 2016, **85**, 138-147.
106. F. H. B. DeCastro, A. G. Borrego, *J. Colloid Interface Sci.*, 1995, **173**, 8-15.
107. R. Pugh, P. Stenius, *Int. J. Miner. Process.*, 1985, **15**, 193-218.
108. J. R. Kanicky, D. O. Shah, *J. Colloid Interface Sci.*, 2002, **256**, 201-207.
109. J. Rudin, D. T. Wasan, *Colloid Surface*, 1992, **68**, 81-94.
110. J. N. Israelachvili, *Intermolecular and Surface Forces*. Academic Press, 2011.
111. E. Le Calvez, D. Blaudez, T. Buffeteau, B. Desbat, *Langmuir*, 2001, **17**, 670-674.
112. K. Spildo, H. Høiland, *J. Colloid Interface Sci.*, 1999, **209**, 99-108.
113. E. J. Robertson, D. K. Beaman, G. L. Richmond, *Langmuir*, 2013, **29**, 15511-15520.
114. J. Simon-Kutscher, A. Gericke, H. Hühnerfuss, *Langmuir*, 1996, **12**, 1027-1034.
115. C. Y. Tang, Z. Huang, H. C. Allen, *J. Phys. Chem. B*, 2010, **114**, 17068-17076.
116. S. M. Burrows, O. Ogunro, A. A. Frossard, L. M. Russell, P. J. Rasch, S. M. Elliott, *Atmospheric Chemistry and Physics*, 2014, **14**, 13601-13629.
117. S. M. Burrows, E. Gobrogge, L. Fu, K. Link, S. M. Elliott, H. F. Wang, R. Walker, *Geophys. Res. Lett.*, 2016, **43**, 8306-8313.
118. X. Chen, W. Hua, Z. Huang, H. C. Allen, *J. Am. Chem. Soc.*, 2010, **132**, 11336-11342.
119. E. M. Adams. Spectroscopic Studies of Atmospherically- and Biologically-Relevant Interfaces: Lipids, Ions, and Interfacial Water Structure: The Ohio State University; 2016.
120. H. Nakahara, O. Shibata, M. Rusdi, Y. Moroi, *J. Phys. Chem. C*, 2008, **112**, 6398-6403.
121. W. Hua, D. Verreault, E. M. Adams, Z. S. Huang, H. C. Allen, *J. Phys. Chem. C*, 2013, **117**, 19577-19585.
122. Z. S. Huang, W. Hua, D. Verreault, H. C. Allen, *J. Phys. Chem. A*, 2013, **117**, 13412-13418.
123. T. Adel. Design, Contruction, and Implementation of Ionization Method Surface Potential Instrument for Studies of Charged Surfactants and Inorganic Electrolytes at the Air/Water Interface: The Ohio State University; 2017.
124. M. Boncheva, F. Damien, V. Normand, *Biochim. Biophys. Acta, Biomembr.*, 2008, **1778**, 1344-1355.
125. D. M. Small, *J. Lipid Res.*, 1984, **25**, 1490-1500.
126. J. A. Donnison, E. Heymann, *Trans. Faraday Soc.*, 1946, **42**, 1-5.
127. D. A. Knopf, S. M. Forrester, *J. Phys. Chem. A*, 2011, **115**, 5579-5591.

128. B. J. Cheek, A. B. Steel, C. J. Miller, *Langmuir*, 2000, **16**, 10334-10339.
129. T. Zhang, S. L. Brantley, D. Verreault, R. Dhankani, S. A. Corcelli, H. C. Allen, *Langmuir*, 2018, **34**, 530-539.
130. P. B. Petersen, R. J. Saykally, *Annu. Rev. Phys. Chem.*, 2006, **57**, 333-364.
131. P. B. Miranda, Q. Du, Y. R. Shen, *Chem. Phys. Lett.*, 1998, **286**, 1-8.
132. C. Y. Tang, Z. S. Huang, H. C. Allen, *J. Phys. Chem. B*, 2011, **115**, 34-40.
133. Y. R. Shen, *Annu. Rev. Phys. Chem.*, 1989, **40**, 327-350.
134. S. Gopalakrishnan, D. F. Liu, H. C. Allen, M. Kuo, M. J. Shultz, *Chem. Rev.*, 2006, **106**, 1155-1175.
135. J. Lobau, K. Wolfrum, *J Opt Soc Am B*, 1997, **14**, 2505-2512.
136. R. R. Feng, Y. Guo, R. Lu, L. Velarde, H. F. Wang, *J. Phys. Chem. A*, 2011, **115**, 6015-6027.
137. H. Nakahara, O. Shibata, Y. Moroi, *J. Phys. Chem. B*, 2011, **115**, 9077-9086.
138. V. F. McNeill, N. Sareen, A. N. Schwier, *Top. Curr. Chem.*, 2014, **339**, 201-259.
139. W. Seidl, *Atmos. Environ.*, 2000, **34**, 4917-4932.
140. C. Pfrang, K. Rastogi, E. R. Cabrera-Martinez, A. M. Seddon, C. Dicko, A. Labrador, T. S. Plivelic, N. Cowieson, A. M. Squires, *Nat. Commun.*, 2017, **8**, 1724.
141. A. C. Finlayson, *J. Chem. Educ.*, 1992, **69**, 559-559.
142. G. M. Hale, M. R. Querry, *Appl. Opt.*, 1973, **12**, 555-563.
143. G. B. Deacon, R. J. Phillips, *Coord. Chem. Rev.*, 1980, **33**, 227-250.
144. K. Nakamoto, J. Fujita, S. Tanaka, M. Kobayashi, *J. Am. Chem. Soc.*, 1957, **79**, 4904-4908.
145. J. E. Tackett, *Appl. Spectrosc.*, 1989, **43**, 483-489.
146. R. C. Mehrotra, R. Bohra, *Metal Carboxylates*. Academic Press, 1983.
147. A. Gericke, H. Huhnerfuss, *Thin Solid Films*, 1994, **245**, 74-82.
148. D. J. Floisand, S. A. Corcelli, *J. Phys. Chem. Lett.*, 2015, **6**, 4012-4017.
149. J. W. DePalma, P. J. Kelleher, L. C. Tavares, M. A. Johnson, *J. Phys. Chem. Lett.*, 2017, **8**, 484-488.
150. D. A. Edwards, R. N. Hayward, *Can. J. Chem.*, 1968, **46**, 3443-3446.
151. P. N. Nelson, R. A. Taylor, *Appl. Petrochem. Res.*, 2014, **4**, 253-285.
152. A. Gericke, R. Mendelsohn, *Langmuir*, 1996, **12**, 758-762.
153. W. Lin, A. J. Clark, F. Paesani, *Langmuir*, 2015, **31**, 2147-2156.
154. P. K. Weissenborn, R. J. Pugh, *J. Colloid Interface Sci.*, 1996, **184**, 550-563.
155. J. J. Bikerman, *Kolloid Z. Z. Polym.*, 1963, **191**, 33-35.
156. E. Pezron, P. M. Claesson, J. M. Berg, D. Vollhardt, *J. Colloid Interface Sci.*, 1990, **138**, 245-254.
157. N. N. Casillas-Ituarte, X. Chen, H. Castada, H. C. Allen, *J. Phys. Chem. B*, 2010, **114**, 9485-9495.
158. Y. Marcus, *Biophys. Chem.*, 1994, **51**, 111-127.
159. K. D. Collins, *Biophys. Chem.*, 2006, **119**, 271-281.
160. A. Gilby, E. Heymann, *Aust. J. Chem.*, 1952, **5**, 160-172.
161. Y. Mao, Y. Du, X. Cang, J. Wang, Z. Chen, H. Yang, H. Jiang, *J. Phys. Chem. B*, 2013, **117**, 850-858.
162. T. Zhang, M. G. Cathcart, A. S. Vidalis, H. C. Allen, *Chem. Phys. Lipids*, 2016, **200**, 24-31.

163. A. A. Trapeznikov, *Proc. 2nd Intern. Congr. Surface Activity, London*, 1957, **1**, 109-120.
164. N. Pilpel, *Adv. Colloid. Interface Sci.*, 1969, **2**, 262-296.
165. E. C. Griffith, V. Vaida, *Proc. Natl. Acad. Sci. U. S. A.*, 2012, **109**, 15697-15701.
166. W. Gan, B.-h. Wu, Z. Zhang, Y. Guo, H.-f. Wang, *J. Phys. Chem. C*, 2007, **111**, 8716-8725.
167. T. Nguyen, A. V. Nguyen, *Soft Matter*, 2014, **10**, 6556-6563.
168. M. I. Viseu, A. M. G. da Silva, S. M. B. Costa, *Langmuir*, 2001, **17**, 1529-1537.
169. A. M. Prpich, Y. B. Sheng, W. Wang, M. E. Biswas, P. Chen, *PLoS One*, 2009, **4**, e8281.
170. D. Hu, K. C. Chou, *J. Am. Chem. Soc.*, 2014, **136**, 15114-15117.
171. S. Chattopadhyay, P. J. Ziemann, *Aerosol Sci. Technol.*, 2005, **39**, 1085-1100.
172. D. Beneventi, B. Carre, A. Gandini, *J. Colloid Interface Sci.*, 2001, **237**, 142-144.
173. L. V. N. Avila, S. M. Saraiva, J. F. Oliveira, *Colloids Surf., A*, 1999, **154**, 209-217.
174. A. M. Brzozowska, M. H. G. Duits, F. Mugele, *Colloids Surf., A*, 2012, **407**, 38-48.
175. Y. L. Lee, J. Y. Lin, S. Lee, *Langmuir*, 2007, **23**, 2042-2051.
176. D. Vollhardt, U. Retter, S. Siegel, *Thin Solid Films*, 1991, **199**, 189-199.
177. D. Vollhardt, *Adv. Colloid. Interface Sci.*, 2006, **123**, 173-188.
178. Y. L. Lee, K. L. Liu, *Langmuir*, 2004, **20**, 3180-3187.
179. Z. Bilkadi, R. D. Neuman, *J. Colloid Interface Sci.*, 1981, **82**, 480-489.
180. L. Ter Minassian-Saraga, *J. Colloid Sci.*, 1956, **11**, 398-418.
181. J. M. R. Patino, M. R. R. Nino, *Colloids Surf., B*, 1999, **15**, 235-252.
182. C. C. Sanchez, M. R. Nino, J. M. R. Patino, *Colloids Surf., B*, 1999, **12**, 175-192.
183. P. Joos, M. Vanuffelen, *J. Colloid Interface Sci.*, 1993, **155**, 271-282.
184. H. F. Wang, L. Velarde, W. Gan, L. Fu, *Annu. Rev. Phys. Chem.*, 2015, **66**, 189-216.
185. N. Watanabe, H. Yamamoto, A. Wada, K. Domen, C. Hirose, T. Ohtake, N. Mino, *Spectrochim. Acta, Part A*, 1994, **50**, 1529-1537.
186. D. Zhang, J. Gutow, K. B. Eisenthal, *J. Phys. Chem.*, 1994, **98**, 13729-13734.
187. P. Desmeules, S. E. Penney, B. Desbat, C. Salesse, *Biophys. J.*, 2007, **93**, 2069-2082.
188. A. K. Covington, M. Paabo, R. A. Robinson, R. G. Bates, *Anal. Chem.*, 1968, **40**, 700-706.
189. Y. L. Lee, J. Y. Lin, C. H. Chang, *J. Colloid Interface Sci.*, 2006, **296**, 647-654.
190. L. C. Salay, M. Ferreira, O. N. Oliveira, C. R. Nakaie, S. Schreier, *Colloids Surf., B*, 2012, **100**, 95-102.
191. E. Rudolphi-Skorska, M. Zembala, M. Filek, *J. Membrane Biol.*, 2014, **247**, 81-92.
192. P. Luckham, J. Wood, S. Froggatt, R. Swart, *J. Colloid Interface Sci.*, 1992, **153**, 368-377.
193. S. Y. Zaitsev, V. P. Zubov, D. Mobius, *Colloids Surf., A*, 1995, **94**, 75-83.
194. S. R. Kim, S. A. Choi, J. D. Kim, *Korean J. Chem. Eng.*, 1996, **13**, 46-53.
195. J. Minones, J. M. R. Patino, J. Minones, P. Dynarowicz-Latka, C. Carrera, *J. Colloid Interface Sci.*, 2002, **249**, 388-397.
196. I. Estrela-Lopis, G. Brezesinski, H. Mohwald, *Chem. Phys. Lipids*, 2004, **131**, 71-80.

197. D. Risovic, S. Frka, Z. Kozarac, *J. Colloid Interface Sci.*, 2012, **373**, 116-121.

Appendix A: Calculation of Fresnel Factors in the CH and OH Stretching Regions

Two workbooks have been made in Microsoft Excel to calculate the Fresnel factors for SFG data in the CH (2800-3000 cm^{-1}) and OH (3000-3800 cm^{-1}) stretching regions. These user-friendly workbooks allow for more detailed calculations of the Fresnel factors which, as a function of frequency, can vary across a spectral region due to changes in the refractive index of the aqueous medium. These workbooks can be found in two locations with the file names "Fresnel Factors Rigorous Workbook_HFWang" and "Fresnel Factors Rigorous Workbook_HFWang_CH Region."; 1) Allen Group Drive > FRESNEL FACTORS, 2) USB drive in NW 3105.

A.1. OH Stretching Region

SFG spectra in the OH stretching region are typically collected in the *ssp* polarization combination. The effective $\chi^{(2)}$ in this polarization combination is expressed as

$$\chi^{(2)}_{eff,ssp} = L_{yy}(\omega_{SFG})L_{yy}(\omega_{vis})L_{zz}(\omega_{IR})\sin\beta_{IR}\chi^{(2)}_{yyz}. \quad \text{(A.1)}$$

The Fresnel factors (L_{ii}) are functions of refractive index and experimental geometry (i.e. angles of the beams).

$$L_{xx}(\omega_i) = \frac{2n_1(\omega_i)\cos\gamma_i}{n_1(\omega_i)\cos\gamma_i + n_2(\omega_i)\cos\beta_i} \quad \text{(A.2a)}$$

$$L_{yy}(\omega_i) = \frac{2n_1(\omega_i)\cos\beta_i}{n_1(\omega_i)\cos\beta_i + n_2(\omega_i)\cos\gamma_i} \tag{A.2b}$$

$$L_{zz}(\omega_i) = \frac{2n_2(\omega_i)\cos\beta_i}{n_1(\omega_i)\cos\gamma_i + n_2(\omega_i)\cos\beta_i}\left(\frac{n_1(\omega_i)}{n'(\omega_i)}\right)^2 \tag{A.2c}$$

As the SFG setup used here uses a broadband IR beam, one must account for changes of the refractive index (n_2) with frequency. The changes of the refractive index of water are shown in Fig. A.2.[142] This data was fit to a function which best captured the shape of the curve. The equation of fit was implemented in the Excel workbook in column "I", where the refractive index of water is calculated as a function of the IR wavelength (n2(IR)) (Fig. A.3). For the wavelengths of the SFG beam, however, the refractive index of water remains fairly constant (Fig. A.4). The refractive index data in this region was fit to a linear function, and this equation was used to correct for n_2 for the SFG beam (column "M", Fig, A.5).

In the equations for the Fresnel factors, the refracted angle of the beams are also parameters. Using the wavelength-evaluated refractive indices, Snell's law was used to calculate the refracted angle of the beams at each wavelength (Fig. A.6).

$$n_1 \sin\theta_1 = n_2(\lambda)\sin\theta_2 \tag{A.3}$$

Once the refractive indices and refracted angles are calculated within the workbook, the Fresnel factors L_{yy}(SFG), L_{yy}(vis), and L_{zz}(IR) can be calculated at each wavelength (Fig. A.7). As the intensity of the SFG beam is proportional to the square of the $\chi^{(2)}_{eff}$, the square

of the calculated $\chi_{eff}^{(2)}$ from the Fresnel factors (eqn. (A.1)) is taken for all wavelengths (Fig. A.8). The SFG intensity is then divided by these values to get the Fresnel-corrected $\chi_{yyz}^{(2)}$ term. This workbook uses the Fresnel factor formulas used in the work of Hong-Fei Wang (eqns. (A.2a-c)).[61,136] The equations used by Shultz *et al* and Wolfrum *et al* produced different results (See Chapter 4).[134,135] Similar differences between various formalisms were shown in Wang's 2011 paper in the Journal of Physical Chemistry A.[136]

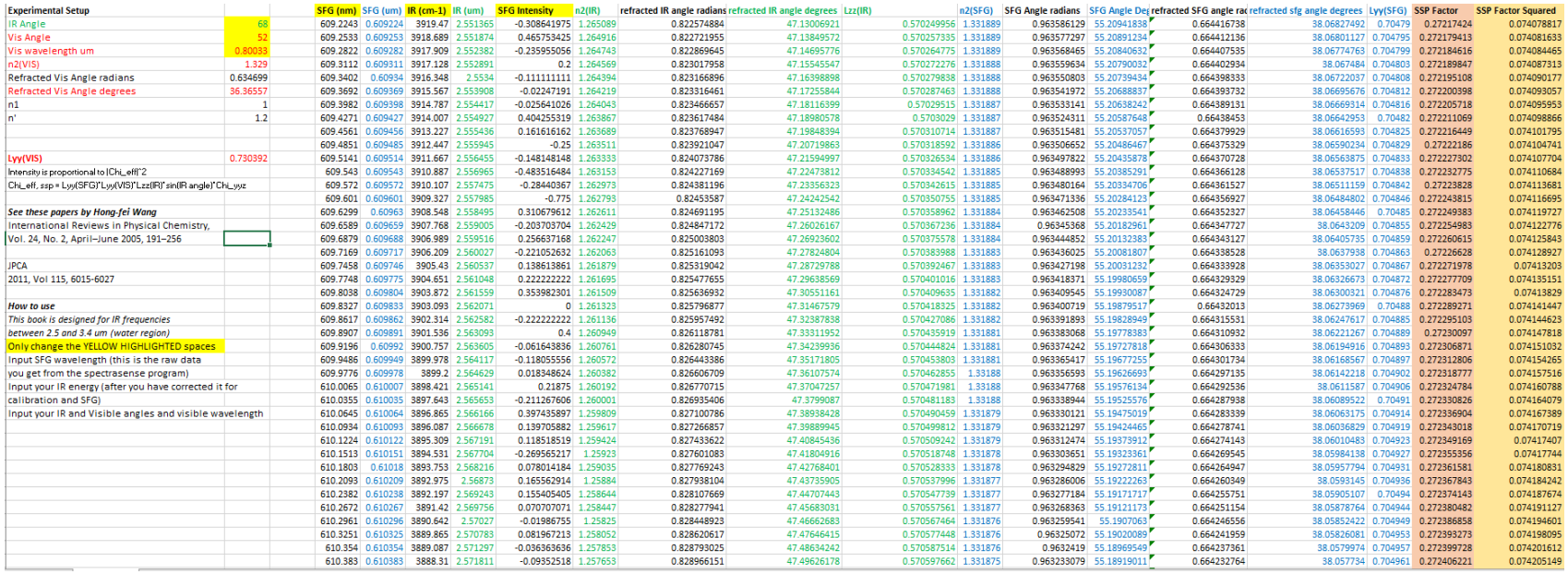

Experimental Setup			SFG (nm)	SFG (um)	IR (cm-1)	IR (um)	SFG Intensity	n2(IR)	refracted IR angle radians	refracted IR angle degrees	Lzz(IR)	n2(SFG)	SFG Angle radians	SFG Angle Deg	refracted SFG angle rac	refracted sfg angle degrees	Lyy(SFG)	SSP Factor	SSP Factor Squared
IR Angle	68		609.2243	0.609224	3919.47	2.551365	-0.308641975	1.265089	0.822574884	47.13006921	0.570249956	1.331889	0.963586129	55.20941838	0.664416738	38.06827492	0.70479	0.27217424	0.074078817
Vis Angle	52		609.2533	0.609253	3918.689	2.551874	0.465753425	1.264916	0.822721955	47.13849572	0.570257335	1.331889	0.963577297	55.20891234	0.664412136	38.06801127	0.704795	0.272179413	0.074081633
Vis wavelength um	0.80033		609.2822	0.609282	3917.909	2.552382	-0.235955056	1.264743	0.822869645	47.14695776	0.570264775	1.331889	0.963568465	55.20840632	0.664407535	38.06774763	0.704799	0.272184616	0.074084465
n2(VIS)	1.329		609.3112	0.609311	3917.128	2.552891	0.2	1.264569	0.823017958	47.15545547	0.570272276	1.331888	0.963559634	55.20790032	0.664402934	38.067484	0.704803	0.272189847	0.074087313
Refracted Vis Angle radians	0.634699		609.3402	0.60934	3916.348	2.5534	-0.111111111	1.264394	0.823166896	47.16398898	0.570279838	1.331888	0.963550803	55.20739434	0.664398333	38.06722037	0.704808	0.272195108	0.074090177
Refracted Vis Angle degrees	36.36557		609.3692	0.609369	3915.567	2.553908	-0.02247191	1.264219	0.823316461	47.17255844	0.570287463	1.331888	0.963541972	55.20688837	0.664393732	38.06695676	0.704812	0.272200398	0.074093057
n1	1		609.3982	0.609398	3914.787	2.554417	-0.025641026	1.264043	0.823466657	47.18116399	0.57029515	1.331887	0.963533141	55.20638242	0.664389131	38.06669314	0.704816	0.272205718	0.074095953
n'	1.2		609.4271	0.609427	3914.007	2.554927	0.404255319	1.263867	0.823617484	47.18980578	0.5703029	1.331887	0.963524311	55.20587648	0.66438453	38.06642953	0.70482	0.272211069	0.074098866
			609.4561	0.609456	3913.227	2.555436	0.161616162	1.263689	0.823768947	47.19848394	0.570310714	1.331887	0.963515481	55.20537057	0.664379929	38.06616593	0.704825	0.272216449	0.074101795
			609.4851	0.609485	3912.447	2.555945	-0.25	1.263511	0.823921047	47.20719863	0.570318592	1.331886	0.963506652	55.20486467	0.664375329	38.06590234	0.704829	0.27222186	0.074104741
Lyy(VIS)	0.730392		609.5141	0.609514	3911.667	2.556455	-0.148148148	1.263333	0.824073786	47.21594997	0.570326534	1.331886	0.963497822	55.20435878	0.664370728	38.06563875	0.704833	0.272227302	0.074107704
Intensity is proportional to |Chi_eff|^2			609.543	0.609543	3910.887	2.556965	-0.483516484	1.263153	0.824227169	47.22473812	0.570334542	1.331885	0.963488993	55.20385291	0.664366128	38.06537517	0.704838	0.272232775	0.074110684
Chi_eff, ssp = Lyy(SFG)*Lyy(VIS)*Lzz(IR)*sin(IR angle)*Chi_yyz			609.572	0.609572	3910.107	2.557475	-0.28440367	1.262973	0.824381196	47.23356323	0.570342615	1.331885	0.963480164	55.20334706	0.664361527	38.06511159	0.704842	0.27223828	0.074113681
			609.601	0.609601	3909.327	2.557985	-0.775	1.262793	0.82453587	47.24242542	0.570350755	1.331885	0.963471336	55.20284123	0.664356927	38.06484802	0.704846	0.272243815	0.074116695
See these papers by Hong-fei Wang			609.6299	0.60963	3908.548	2.558495	0.310679612	1.262611	0.824691195	47.25132486	0.570358962	1.331884	0.963462508	55.20233541	0.664352327	38.06458446	0.70485	0.272249383	0.074119727
International Reviews in Physical Chemistry,			609.6589	0.609659	3907.768	2.559005	-0.203703704	1.262429	0.824847172	47.26026167	0.570367236	1.331884	0.96345368	55.20182961	0.664347727	38.0643209	0.704855	0.272254983	0.074122776
Vol. 24, No. 2, April–June 2005, 191–256			609.6879	0.609688	3906.989	2.559516	0.256637168	1.262247	0.825003803	47.26923602	0.570375578	1.331884	0.963444852	55.20132383	0.664343127	38.06405735	0.704859	0.272260615	0.074125843
			609.7169	0.609717	3906.209	2.560027	-0.221052632	1.262063	0.825161093	47.27824804	0.570383988	1.331883	0.963436025	55.20081807	0.664338528	38.0637938	0.704863	0.27226628	0.074128927
JPCA			609.7458	0.609746	3905.43	2.560537	0.138613861	1.261879	0.825319042	47.28729788	0.570392467	1.331883	0.963427198	55.20031232	0.664333928	38.06353027	0.704867	0.272271978	0.07413203
2011, Vol 115, 6015-6027			609.7748	0.609775	3904.651	2.561048	0.222222222	1.261695	0.825477655	47.29638569	0.570401016	1.331883	0.963418371	55.19980659	0.664329329	38.06326673	0.704872	0.272277709	0.074135151
			609.8038	0.609804	3903.872	2.561559	0.353982301	1.261509	0.825636932	47.30551161	0.570409635	1.331882	0.963409545	55.19930087	0.664324729	38.06300321	0.704876	0.272283473	0.07413829
How to use			609.8327	0.609833	3903.093	2.562071	0	1.261323	0.825796877	47.31467579	0.570418325	1.331882	0.963400719	55.19879517	0.66432013	38.06273969	0.70488	0.272289271	0.074141447
This book is designed for IR frequencies			609.8617	0.609862	3902.314	2.562582	-0.222222222	1.261136	0.825957492	47.32387838	0.570427086	1.331882	0.963391893	55.19828949	0.664315531	38.06247617	0.704885	0.272295103	0.074144623
between 2.5 and 3.4 um (water region)			609.8907	0.609891	3901.536	2.563093	0.4	1.260949	0.826118781	47.33311952	0.570435919	1.331881	0.963383068	55.19778383	0.664310932	38.06221267	0.704889	0.2730097	0.074147818
Only change the YELLOW HIGHLIGHTED spaces			609.9196	0.60992	3900.757	2.563605	-0.061643836	1.260761	0.826280745	47.34239936	0.570444824	1.331881	0.963374242	55.19727818	0.664306333	38.06194916	0.704893	0.272306871	0.074151032
Input SFG wavelength (this is the raw data			609.9486	0.609949	3899.978	2.564117	-0.118055556	1.260572	0.826443386	47.35171805	0.570453803	1.331881	0.963365417	55.19677255	0.664301734	38.06168567	0.704897	0.272312806	0.074154265
you get from the spectrasense program)			609.9776	0.609978	3899.2	2.564629	0.018348624	1.260382	0.826606709	47.36107574	0.570462855	1.33188	0.963356593	55.19626693	0.664297135	38.06142218	0.704902	0.272318777	0.074157516
Input your IR energy (after you have corrected it for			610.0065	0.610007	3898.421	2.565141	0.21875	1.260192	0.826770715	47.37047257	0.570471981	1.33188	0.963347768	55.19576134	0.664292536	38.0611587	0.704906	0.272324784	0.074160788
calibration and SFG)			610.0355	0.610035	3897.643	2.565653	-0.211267606	1.260001	0.826935406	47.3799087	0.570481183	1.33188	0.963338944	55.19525576	0.664287938	38.06089522	0.70491	0.272330826	0.074164079
Input your IR and Visible angles and visible wavelength			610.0645	0.610064	3896.865	2.566166	0.397435897	1.259809	0.827100786	47.38938428	0.570490459	1.331879	0.963330121	55.19475019	0.664283339	38.06063175	0.704914	0.272336904	0.074167389
			610.0934	0.610093	3896.087	2.566678	0.139705882	1.259617	0.827266857	47.39889945	0.570499812	1.331879	0.963321297	55.19424465	0.664278741	38.06036829	0.704919	0.272343018	0.074170719
			610.1224	0.610122	3895.309	2.567191	0.118518519	1.259424	0.827433622	47.40845436	0.570509242	1.331879	0.963312474	55.19373912	0.664274143	38.06010483	0.704923	0.272349169	0.07417407
			610.1513	0.610151	3894.531	2.567704	-0.269565217	1.25923	0.827601083	47.41804916	0.570518748	1.331878	0.963303651	55.19323361	0.664269545	38.05984138	0.704927	0.272355356	0.07417744
			610.1803	0.61018	3893.753	2.568216	0.078014184	1.259035	0.827769243	47.42768401	0.570528333	1.331878	0.963294829	55.19272811	0.664264947	38.05957794	0.704931	0.272361581	0.074180831
			610.2093	0.610209	3892.975	2.56873	0.165562914	1.25884	0.827938104	47.43735905	0.570537996	1.331877	0.963286006	55.19222263	0.664260349	38.0593145	0.704936	0.272367843	0.074184242
			610.2382	0.610238	3892.197	2.569243	0.155405405	1.258644	0.828107669	47.44707443	0.570547739	1.331877	0.963277184	55.19171717	0.664255751	38.05905107	0.70494	0.272374143	0.074187674
			610.2672	0.610267	3891.42	2.569756	0.070707071	1.258447	0.828277941	47.45688031	0.570557561	1.331877	0.963268363	55.19121173	0.664251154	38.05878764	0.704944	0.272380482	0.074191127
			610.2961	0.610296	3890.642	2.57027	-0.01986755	1.25825	0.828448923	47.46662683	0.570567464	1.331876	0.963259541	55.1907063	0.664246556	38.05852422	0.704949	0.272386858	0.074194601
			610.3251	0.610325	3889.865	2.570783	0.081967213	1.258052	0.828620617	47.47646415	0.570577448	1.331876	0.96325072	55.19020089	0.664241959	38.05826081	0.704953	0.272393273	0.074198095
			610.354	0.610354	3889.087	2.571297	-0.036363636	1.257853	0.828793025	47.48634242	0.570587514	1.331876	0.9632419	55.18969549	0.664237361	38.0579974	0.704957	0.272399728	0.074201612
			610.383	0.610383	3888.31	2.571811	-0.09352518	1.257653	0.828966151	47.49626178	0.570597662	1.331875	0.963233079	55.18919011	0.664232764	38.057734	0.704961	0.272406221	0.074205149

Figure A.1. Screenshot of the Fresnel factor Microsoft Excel workbook for *ssp* polarization in the OH stretching region.

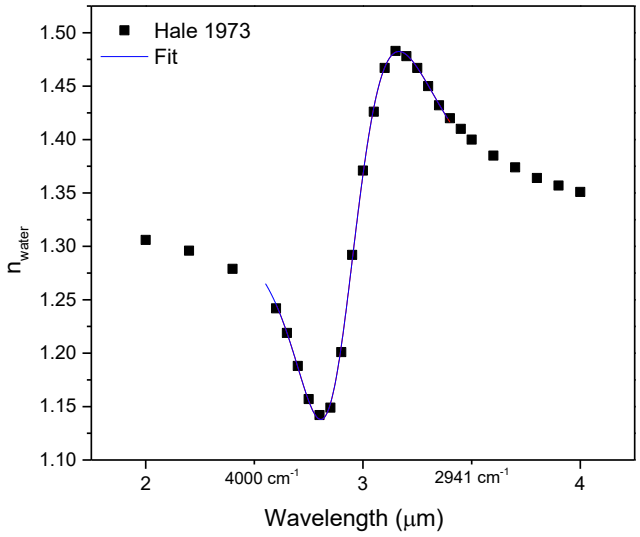

Figure A.2. Refractive index of water as a function of wavelength in the region corresponding to OH stretching modes.[142]

=1.29622543002551+(2*0.47212915840317/PI())*(0.70247760178385/(4*(G2-3.02038220859375)^2+0.70247760178385^2))+(2*(-0.36343034061136)/PI())*(0.47218411683764/(4*(G2-2.85466849717895)^2+0.47218411683764^2))

B	C	D	E	F	G	H	I
		SFG (nm)	SFG (um)	IR (cm-1)	IR (um)	SFG Intensity	n2(IR)
68		609.2243	0.609224	3919.47	2.551365	-0.308641975	1.265089
52		609.2533	0.609253	3918.689	2.551874	0.465753425	1.264916
0.80033		609.2822	0.609282	3917.909	2.552382	-0.235955056	1.264743
1.329		609.3112	0.609311	3917.128	2.552891	0.2	1.264569
0.634699		609.3402	0.60934	3916.348	2.5534	-0.111111111	1.264394
36.36557		609.3692	0.609369	3915.567	2.553908	-0.02247191	1.264219
1		609.3982	0.609398	3914.787	2.554417	-0.025641026	1.264043

Figure A.3. Implementation of the fitting equation for the change in refractive index as a function of IR wavelength.

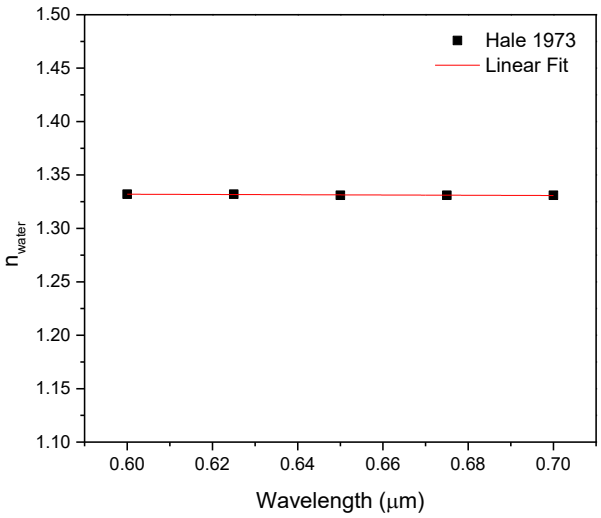

Figure A.4. The change in the refractive index of water at wavelengths associated with those of the SFG beam.[142]

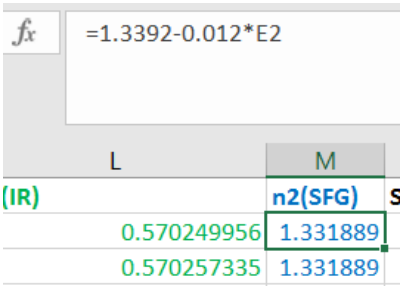

Figure A.5. Implementation of the fitting equation for the change in refractive index as a function of SFG wavelength.

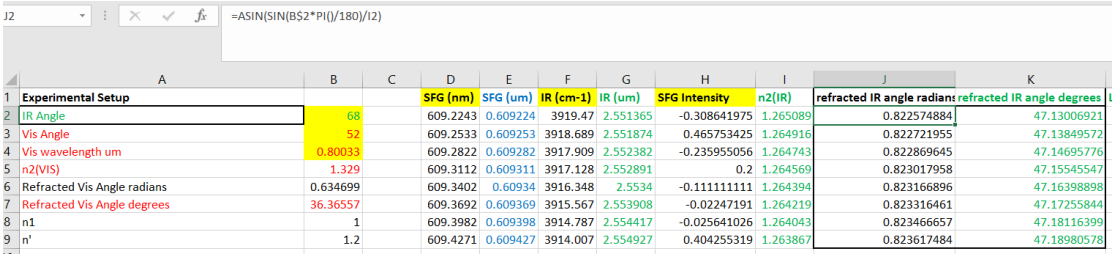

	A	B	C	D	E	F	G	H	I	J	K
1	Experimental Setup			SFG (nm)	SFG (um)	IR (cm-1)	IR (um)	SFG Intensity	n2(IR)	refracted IR angle radians	refracted IR angle degrees
2	IR Angle	68		609.2243	0.609224	3919.47	2.551365	-0.308641975	1.265089	0.822574884	47.13006921
3	Vis Angle	52		609.2533	0.609253	3918.689	2.551874	0.465753425	1.264916	0.822721955	47.13849572
4	Vis wavelength um	0.80033		609.2822	0.609282	3917.909	2.552382	-0.235955056	1.264743	0.822869645	47.14695776
5	n2(VIS)	1.329		609.3112	0.609311	3917.128	2.552891	0.2	1.264569	0.823017958	47.15545547
6	Refracted Vis Angle radians	0.634699		609.3402	0.60934	3916.348	2.5534	-0.111111111	1.264394	0.823166896	47.16398898
7	Refracted Vis Angle degrees	36.36557		609.3692	0.609369	3915.567	2.553908	-0.02247191	1.264219	0.823316461	47.17255844
8	n1	1		609.3982	0.609398	3914.787	2.554417	-0.025641026	1.264043	0.823466657	47.18116399
9	n'	1.2		609.4271	0.609427	3914.007	2.554927	0.404255319	1.263867	0.823617484	47.18980578

Figure A.6. Calculation of refracted angle of the IR beam. Similar calculations are also performed within the workbook for the SFG and visible beams.

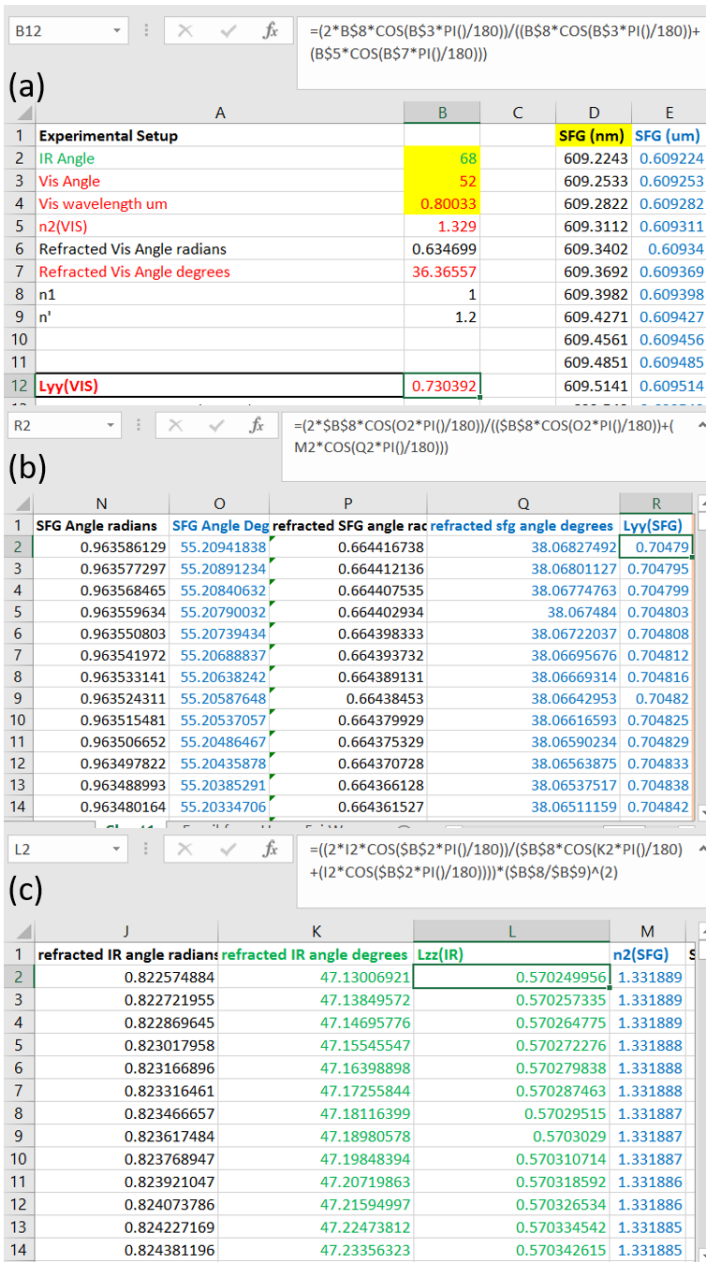

(a)

B12 =(2*B$8*COS(B$3*PI()/180))/((B$8*COS(B$3*PI()/180))+(B$5*COS(B$7*PI()/180)))

	A	B	C	D	E
1	**Experimental Setup**			**SFG (nm)**	**SFG (um)**
2	IR Angle	68		609.2243	0.609224
3	Vis Angle	52		609.2533	0.609253
4	Vis wavelength um	0.80033		609.2822	0.609282
5	n2(VIS)	1.329		609.3112	0.609311
6	Refracted Vis Angle radians	0.634699		609.3402	0.60934
7	Refracted Vis Angle degrees	36.36557		609.3692	0.609369
8	n1	1		609.3982	0.609398
9	n'	1.2		609.4271	0.609427
10				609.4561	0.609456
11				609.4851	0.609485
12	**Lyy(VIS)**	0.730392		609.5141	0.609514

(b)

R2 =(2*$B$8*COS(O2*PI()/180))/(($B$8*COS(O2*PI()/180))+(M2*COS(Q2*PI()/180)))

	N	O	P	Q	R
1	**SFG Angle radians**	**SFG Angle Deg**	**refracted SFG angle rac**	**refracted sfg angle degrees**	**Lyy(SFG)**
2	0.963586129	55.20941838	0.664416738	38.06827492	0.70479
3	0.963577297	55.20891234	0.664412136	38.06801127	0.704795
4	0.963568465	55.20840632	0.664407535	38.06774763	0.704799
5	0.963559634	55.20790032	0.664402934	38.067484	0.704803
6	0.963550803	55.20739434	0.664398333	38.06722037	0.704808
7	0.963541972	55.20688837	0.664393732	38.06695676	0.704812
8	0.963533141	55.20638242	0.664389131	38.06669314	0.704816
9	0.963524311	55.20587648	0.66438453	38.06642953	0.70482
10	0.963515481	55.20537057	0.664379929	38.06616593	0.704825
11	0.963506652	55.20486467	0.664375329	38.06590234	0.704829
12	0.963497822	55.20435878	0.664370728	38.06563875	0.704833
13	0.963488993	55.20385291	0.664366128	38.06537517	0.704838
14	0.963480164	55.20334706	0.664361527	38.06511159	0.704842

(c)

L2 =((2*I2*COS($B$2*PI()/180))/($B$8*COS(K2*PI()/180)+(I2*COS($B$2*PI()/180))))*($B$8/$B$9)^(2)

	J	K	L	M
1	**refracted IR angle radians**	**refracted IR angle degrees**	**Lzz(IR)**	**n2(SFG)**
2	0.822574884	47.13006921	0.570249956	1.331889
3	0.822721955	47.13849572	0.570257335	1.331889
4	0.822869645	47.14695776	0.570264775	1.331889
5	0.823017958	47.15545547	0.570272276	1.331888
6	0.823166896	47.16398898	0.570279838	1.331888
7	0.823316461	47.17255844	0.570287463	1.331888
8	0.823466657	47.18116399	0.57029515	1.331887
9	0.823617484	47.18980578	0.5703029	1.331887
10	0.823768947	47.19848394	0.570310714	1.331887
11	0.823921047	47.20719863	0.570318592	1.331886
12	0.824073786	47.21594997	0.570326534	1.331886
13	0.824227169	47.22473812	0.570334542	1.331885
14	0.824381196	47.23356323	0.570342615	1.331885

Figure A.7. Calculation of (a) L_{yy}(vis), (b) L_{yy}(SFG), and (c) L_{zz}(IR) within the Fresnel factor workbook.

S2 | =$B$12*L2*R2*SIN(B$2*PI()/180)

	Q	R	S	T	U
1	refracted sfg angle degrees	Lyy(SFG)	SSP Factor	SSP Factor Squared	
2	38.06827492	0.70479	0.27217424	0.074078817	
3	38.06801127	0.704795	0.272179413	0.074081633	
4	38.06774763	0.704799	0.272184616	0.074084465	
5	38.067484	0.704803	0.272189847	0.074087313	
6	38.06722037	0.704808	0.272195108	0.074090177	
7	38.06695676	0.704812	0.272200398	0.074093057	
8	38.06669314	0.704816	0.272205718	0.074095953	
9	38.06642953	0.70482	0.272211069	0.074098866	
10	38.06616593	0.704825	0.272216449	0.074101795	

Figure A.8. Calculation of the Fresnel factor term in eqn. (A.1) in column "S" and the square of that term in column "T."

A.2. CH Stretching Region: Orientation Analysis Workbook for C_{3v} Symmetry

In the CH stretching region, one can use the intensities of the CH_3 asymmetric and symmetric stretches in the *ppp* and *ssp* polarization combinations, respectively, to determine the oreintation of the alkyl chain at the interface. The *ssp* $\chi^{(2)}_{eff}$ term is calculated in the same manner as in section A.1, but in the CH stretching region where the refractive index of water does not change as drastically with wavelength, and is calculated from the fit in Fig. A.3. The $\chi^{(2)}_{eff,ppp}$ function, however is more complicated and consists of four terms.[184]

$$\chi^{(2)}_{eff,ppp} = -L_{xx}(\omega_{SFG})L_{xx}(\omega_{vis})L_{zz}(\omega_{IR})\cos\beta_{SFG}\cos\beta_{vis}\sin\beta_{IR}\chi^{(2)}_{xxz} \quad \text{(A.4)}$$

$$-L_{xx}(\omega_{SFG})L_{zz}(\omega_{vis})L_{xx}(\omega_{IR})\cos\beta_{SFG}\sin\beta_{vis}\cos\beta_{IR}\,\chi^{(2)}_{xzx}$$

$$+L_{zz}(\omega_{SFG})L_{xx}(\omega_{vis})L_{xx}(\omega_{IR})\sin\beta_{SFG}\cos\beta_{vis}\cos\beta_{IR}\,\chi^{(2)}_{zxx}$$

$$+ L_{zz}(\omega_{SFG})L_{zz}(\omega_{vis})L_{zz}(\omega_{IR}) \sin\beta_{SFG} \sin\beta_{vis} \sin\beta_{IR}\, \chi^{(2)}_{zzz}$$

The Fresnel factor portions of the *ssp* and *ppp* terms are calculated one at a time, without the $\chi^{(2)}_{ijk}$ factors, which have an angular orientation dependence (Fig. A.9).

Because there are so many terms in the *ppp* polarization combination, to continue with the analysis, we select only the calculated Fresnel factors for the frequencies at which the CH_3 asymmetric and symmetric stretches occur for the system of interest (Fig. A.10).

For a C_{3v} methyl group, the orientation dependence on $\chi^{(2)}_{eff}$ comes from the dependence of the $\chi^{(2)}_{ijk}$ elements on θ_{CH3}. For the *ssp* polarization, $\chi^{(2)}_{yyz}$ for the symmetric stretch of the CH_3 group is

$$\chi^{(2)}_{yyz,ss} = \frac{1}{2} N_s \beta_{ccc}[(1+R)\langle\cos\theta_{CH3}\rangle - (1-R)\langle\cos^3\theta_{CH3}\rangle]. \quad \text{(A.5)}$$

The $\chi^{(2)}_{ijk}$ elements for the *ppp* polarization are as follows in eqns. (A.6-A.8).

$$\chi^{(2)}_{yyz,as} = \chi^{(2)}_{xxz,as} = -N_s \beta_{aca}[\langle\cos\theta_{CH3}\rangle - \langle\cos^3\theta_{CH3}\rangle] \quad \text{(A.6)}$$

$$\chi^{(2)}_{yzy,as} = \chi^{(2)}_{xzx,as} = \chi^{(2)}_{zxx,as} = \chi^{(2)}_{zyy,as} = N_s \beta_{aca}\langle\cos^3\theta_{CH3}\rangle \quad \text{(A.7)}$$

$$\chi^{(2)}_{zzz,as} = 2N_s \beta_{aca}[\langle\cos\theta_{CH3}\rangle - \langle\cos^3\theta_{CH3}\rangle] \quad \text{(A.8)}$$

In these equations, R is the hyperpolarizability ratio defined as β_{aac}/β_{ccc} and is set as 2.3, and the ratio of β_{aca}/β_{aac} is 4.2, and can be used to find β_{aca}.[185,186]

In the workbook, $\cos\theta_{CH3}$ and $\cos^3\theta_{CH3}$ are calculated at increments of 0.1°. From this, the orientation dependence (eqns. (A.5-A.8)) can be added into the calculation of $\chi_{eff}^{(2)}$ for both the *ssp* and *ppp* polarization combinations, and will produce the graph shown in Fig. A.11a.

Once the ratio of the $\chi_{ppp,as}^{(2)}$ to $\chi_{ssp,ss}^{(2)}$ elements as a function of methyl group orientation is determined, one can use the square root of the intensities of the asymmetric and symmetric stretch of the CH_3 mode in the *ppp* and *ssp* polarization combinations to find this ratio in the experimental data on the y-axis of Fig. A.11b to determine the methyl group orientation at that point on the x-axis. For a single chain molecule, assumed to be in an all trans configuration, the tilt angle of the hydrocarbon chain relative to the surface normal can be determined from the relation shown in eqn. (A.9).[167]

$$\theta_{tilt} = 37° - \theta_{CH3} \tag{A.9}$$

V	W	X	Y	Z
ssp, sym CH3 Fresnel Part	ppp, asym CH3 Fresnel Part 1	ppp, asym CH3 Fresnel Part 2	ppp, asym CH3 Fresnel Part 3	ppp, asym CH3 Fresnel Part 4
0.27605212	-0.190722237	-0.126992268	0.15005006	0.146559016
0.276048451	-0.190720139	-0.126994984	0.150051783	0.146555951
0.276044839	-0.190718072	-0.126997662	0.150053481	0.146552932
0.276041229	-0.190716008	-0.127000338	0.150055178	0.146549913
0.276037622	-0.190713944	-0.127003014	0.150056873	0.146546896
0.276033962	-0.190711852	-0.127005729	0.150058593	0.146543836
0.276030358	-0.190709791	-0.127008404	0.150060288	0.146540821
0.276026756	-0.190707732	-0.127011078	0.150061981	0.146537807
0.276023156	-0.190705675	-0.127013752	0.150063673	0.146534793
0.276019559	-0.190703619	-0.127016425	0.150065365	0.146531781
0.27601591	-0.190701534	-0.127019137	0.150067081	0.146528726
0.276012316	-0.190699481	-0.127021809	0.15006877	0.146525716

*ssp, sym CH3 Fresnel Part=$B$12*T2*M2*SIN($B$2*PI()/180)*

ppp, asym CH3 Fresnel Part 1=

*-S2*$B$13*M2*COS(P2*PI()/180)*COS($B$3*PI()/180)*SIN($B$2*PI()/180)*

ppp, asym CH3 Fresnel Part 2 =

*-S2*$B$14*L2*COS(P2*PI()/180)*SIN($B$3*PI()/180)*COS($B$2*PI()/180)*

ppp, asym CH3 Fresnel Part 3 =
*U2*$B$13*L2*SIN(P2*PI()/180)*COS($B$3*PI()/180)*COS($B$2*PI()/180)*

ppp, asym CH3 Fresnel Part 4 =
*U2*$B$14*M2*SIN(P2*PI()/180)*SIN($B$3*PI()/180)*SIN($B$2*PI()/180)*

Figure A.9. Calculation of each Fresnel factor term in the $\chi_{eff}^{(2)}$ expressions and the equations built in to the workbook for each column.

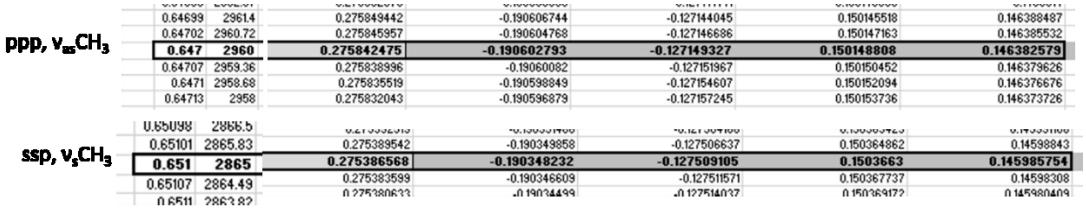

Figure A.10. Selection of the Fresnel factors at the frequencies used in the rest of the analysis.

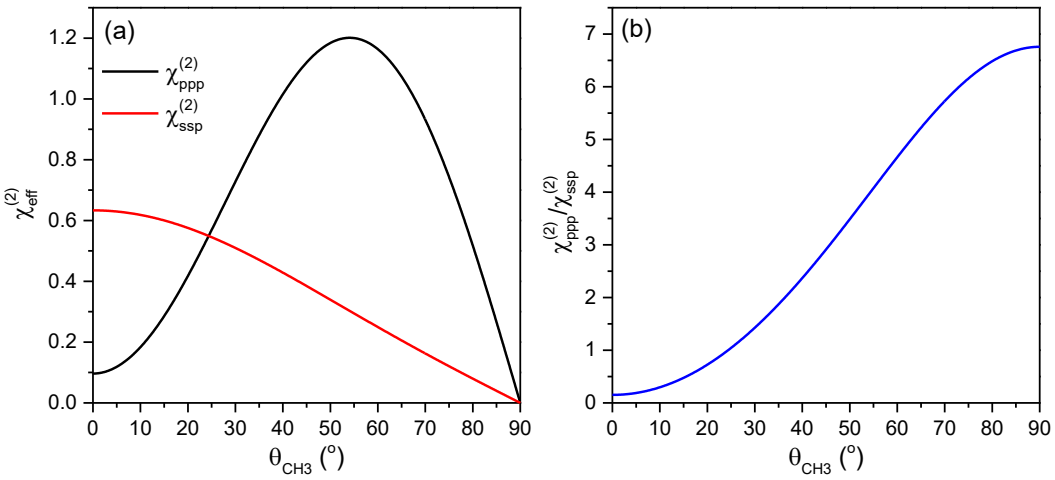

Figure A.11. (a) $\chi^{(2)}_{eff}$ calculated for the *ppp* asymmetric stretch and the *ssp* symmetric stretch as a function of methyl group orientation; (b) the ratio of the $\chi^{(2)}_{ppp,as}$ to $\chi^{(2)}_{ssp,ss}$ as a function of methyl group orientation.

Appendix B: IRRAS Spectra of Ion-Carboxylate Binding in D_2O

To further elucidate the ion-induced deprotonation of PA monolayer headgroups by Ca^{2+}, analogous IRRAS experiments to those presented in Section 5.3.1 were conducted with 300 mM $CaCl_2$ solutions prepared in D_2O (99%, Sigma Aldrich, 7789-20-0). This work is part of an ongoing collaboration with the Mark Johnson group at Yale University to reevaluate binding motifs of various ions at the interface.

The use of D_2O in surface-sensitive IRRAS studies of carboxylic acids can be beneficial because the water bending mode at ~1650 cm^{-1} is shifted to lower wavenumbers in the spectra (~1200 cm^{-1}). This allows for more clear observation of the ν_{AS} CO_2^- mode at ~1550 cm^{-1}. While D_2O has its advantages, additional precautions need to be exercised during its use to obtain practical spectra.

Traditionally, divalent chloride salts are purified via filtration through activated carbon filters and then diluted from a stock solution whose concentration has been determined with the Mohr titration.[121,122,141] Such treatment is simply not feasible for D_2O solutions. As such, the desired concentration of salt solution is prepared by direct massing and dissolution of as-received salts. To test for trace metal contamination in these salts, it is recommended to compare the IRRAS spectrum of the monolayer on subphases containing, and in the absence of, the trace metal chelating agent EDTA (99.995% Trace

Metal Basis, Sigma). As EDTA is acidic in its most pure form available for purchase, the solution without EDTA should be pH-adjusted to make a direct comparison. In Fig. B.1, this control experiment was conducted for $CaCl_2$ (>99%, ACS Certified, Fisher Scientific, CAS 10035-4-8) and $MgCl_2$ (>99%, ACS Certified, Fisher Scientific, CAS 7791-18-6) salt solutions in H_2O. As the spectra are comparable, it can be stated that any ion-induced deprotonation is not caused by trace metal contaminants.

As a surface-sensitive spectroscopic probe, IRRAS measurements with D_2O subphases will be sensitive to the condensation of atmospheric water vapor on the aqueous surface. This will result in the observance of strong HOD modes in the spectra. An example of an IRRAS spectrum containing HOD interference is presented in Fig. B.2. The strong feature between 1500 cm^{-1} and 1200 cm^{-1} is attributed to HOD and has been observed elsewhere for IRRAS measurements on D_2O-containing subphases.[187] To prevent these interferences in the spectra, the chamber of the FTIR spectrometer must be purged with a constant flow of N_2. It is also advisable to conduct these experiments in laboratory environments with low relative humidity. To achieve a relatively isolated environment with low H_2O vapor, plastic was used to seal the chamber of the FTIR (Fig. B.3). Plastic was necessary here because the breadboard containing the IRRAS mirrors (set to a 45° angle of incidence)[54] prevented the typical housing chamber to close completely.

In this work, the following procedure produced spectra with minimal H_2O and HOD interference while N_2 flowed continuously to the FTIR chamber: 1) pour subphase into Petri dish, 2) close and seal FTIR chamber, 3) allow the N_2 stream to purge the chamber for 8 minutes, 4) collect R_0 background spectrum, 5) open chamber to spread monolayer

on aqueous surface (~1 minute), 6) reseal the chamber and allow chloroform to evaporate during N_2 purge for 10 minutes, 7) collect spectrum (*R*) of the monolayer-covered surface.

A comparison of the spectra of d_{31}-PA on 300 mM $CaCl_2$ in H_2O and D_2O is presented in Fig. B.4. D_2O effectively removes the water bending mode at ~1650 cm^{-1}. It is quite interesting to note that the intensity of the ν_{AS} CO_2^- mode at ~1550 cm^{-1} is much stronger on the D_2O-containing subphase than the H_2O-containing subphase. Similar phenomena have been reported by other authors in the literature, though no explanation of this change has been provided.[54]

These D_2O IRRAS experiments were conducted as part of a collaboration with the Johnson lab at Yale to reevaluate the empirical rules for ion-carboxylate binding.[143-146] These rules were originally established to interpret the vibrational signatures of transition metal acetates in aqueous solution. From Fig. B.5, it can be seen that the deprotonation signature of Ca^{2+}-bound PA is only slightly different than that of a bare carboxylate mode on a basic subphase. The D_2O solutions were adjusted to basic conditions with NaOD (>99%, Acros Organics, 14014-06-3). The measured pH of the solution was 10.1, but is corrected to pD 10.5 following guidelines in the literature.[188] Here, d_{35}-stearic acid (d_{35}-SA, >98%, Cambridge Isotopes Laboratories) was used as it will not desorb into the subphase. The Ca^{2+}-induced signature of the ν_{AS} CO_2^- mode has a fraction which extends to lower frequencies.

To see if this ν_{AS} CO_2^- signature was unique to Ca^{2+}, the spectra of d_{31}-PA monolayers on D_2O subphases of 300 mM $MgCl_2$ and $ZnCl_2$ (>98%, Acros Organics, CAS

7646-85-7) were also measured (Fig. B.6). The spectrum of d_{31}-PA on the $MgCl_2$ subphase more closely resembles that of the bare carboxylate mode, indicating an ionic binding mechanism mediated by the large hydration shell of the Mg^{2+} ion. The 300 mM $ZnCl_2$ subphase exhibits a sharp mode for the ν_{AS} CO_2^-. This feature, and frequency, associates the binding of Zn^{2+} ions to the carboxylate as a chelating bidentate motif.[114] The lower frequency regime exhibited in the Ca^{2+} spectrum overlays with the ν_{AS} CO_2^- mode observed in 300 mM $ZnCl_2$ subphases. Therefore, we conclude that there exists a fraction of Ca^{2+} ions that bind to d_{31}-PA in a direct, chelating motif. The remaining fraction binds in a hydrated ionic motif. Upon peak-fitting analysis of the complexed Ca^{2+}:d_{31}-PA spectrum, we can approximate the fraction of Ca^{2+} ions bound to the carboxylate group in a direct binding motif as ~35% (Fig. B.7). This percentage can be thought of as an upper limit because the various binding motifs will exhibit different transition dipole moment strengths. As the transition dipole moment strength of the chelating bidentate motif should be greater than that of the ionic motif, a ratio of the relative area of the peak can only produce an upper limit approximation to the fraction.

The Johnson lab (Yale) is conducting gas-phase cluster experiments to identify the binding motif of these ions to the carboxylate groups of shorter-chain fatty acids under varying levels of hydration. Their methodology (IR photodissociation spectroscopy) allows for measurement of infrared spectra of gas-phase clusters. The addition of individual water molecules to the cluster will eventually converge to the bulk limit and can be compared to the IRRAS spectra we collect of the interface.

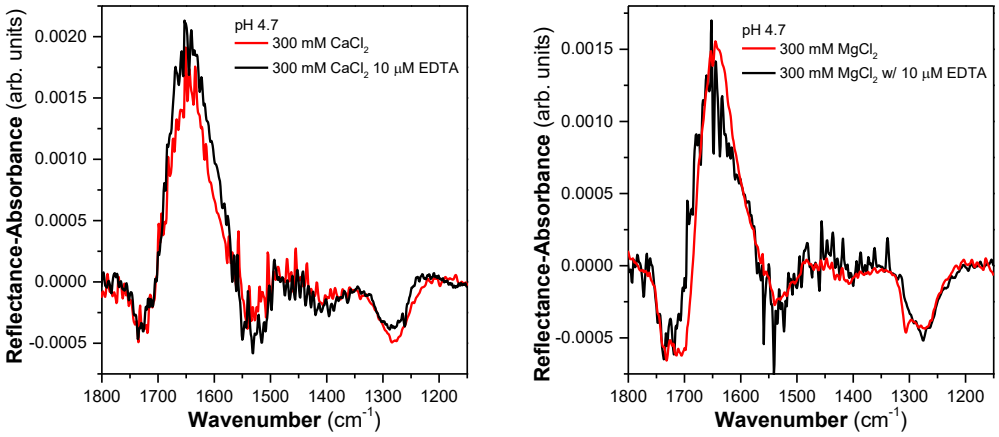

Figure B.1. IRRAS spectra of d_{31}-PA monolayers on 300 mM $CaCl_2$ and $MgCl_2$ subphases with and without the addition of EDTA.

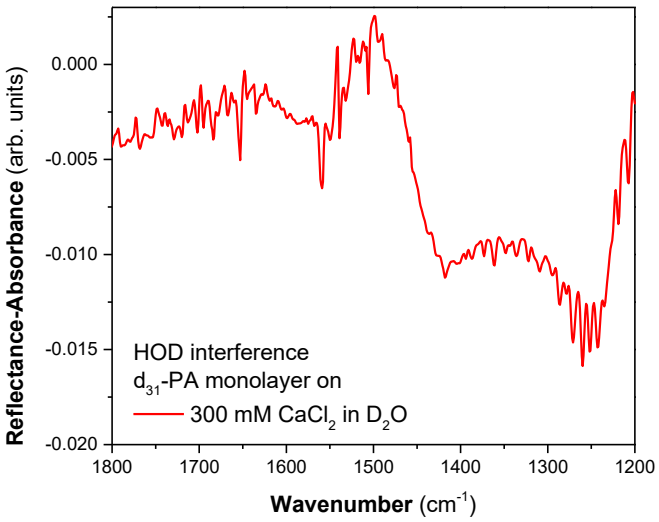

Figure B.2. HOD interference in an IRRAS spectrum.

Figure B.3. IRRAS setup used in D_2O experiments. Plastic seals are necessary to prevent atmospheric H_2O condensation onto the aqueous surface.

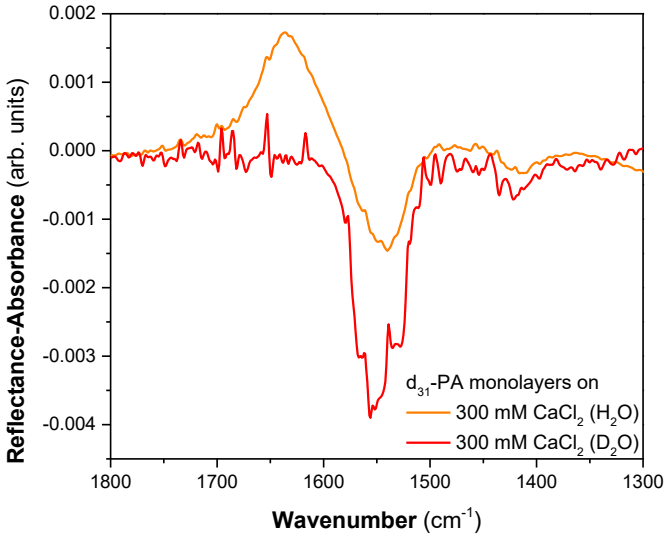

Figure B.4. Comparison of IRRAS spectra of d_{31}-PA monolayers on 300 mM $CaCl_2$ subphases in H_2O and D_2O.

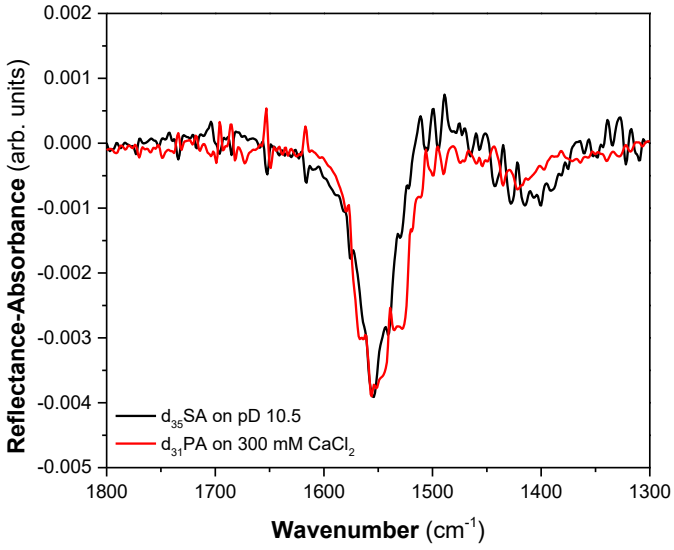

Figure B.5. IRRAS spectra of d_{31}-PA monolayers on 300 mM $CaCl_2$ (D_2O) and d_{35}-SA monolayers on pD 10.5 subphases.

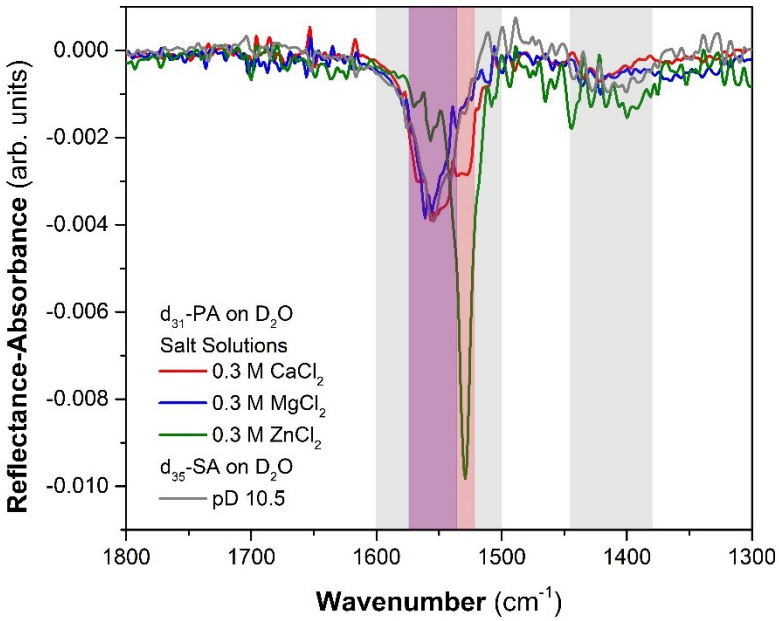

Figure B.6. IRRAS spectra of d_{31}-PA monolayers on 300 mM $CaCl_2$, $MgCl_2$, $ZnCl_2$, and d_{35}-SA monolayers on pD 10.5 subphases.

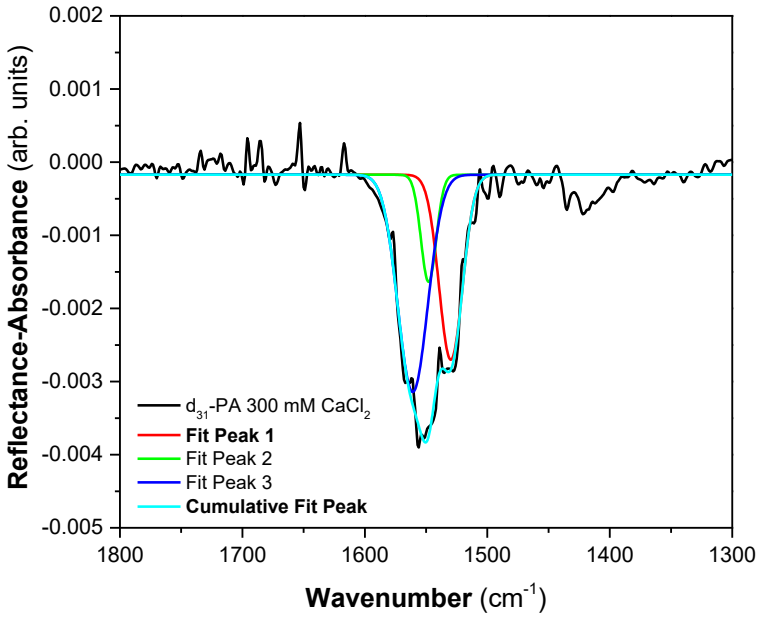

Figure B.7. Gaussian fits of the d_{31}-PA ν_{AS} CO_2^- mode on 300 mM $CaCl_2$ to approximate the relative fraction of chelating bidentate binding species.

Appendix C: IRRAS Data Processing and Controls

C.1. Data Processing

The IRRAS spectra presented in this dissertation are the average of at least three trials. Each trial has been baseline-corrected by third order polynomials prior to averaging. An example of the determination of the baseline is shown in Fig. C.1 where the data points associated with the vibrational modes are removed and a third-order polynomial is fit through the remaining data points. This function is then subtracted from the RA values of that trial in the region of interest to produce the baseline-corrected spectrum.

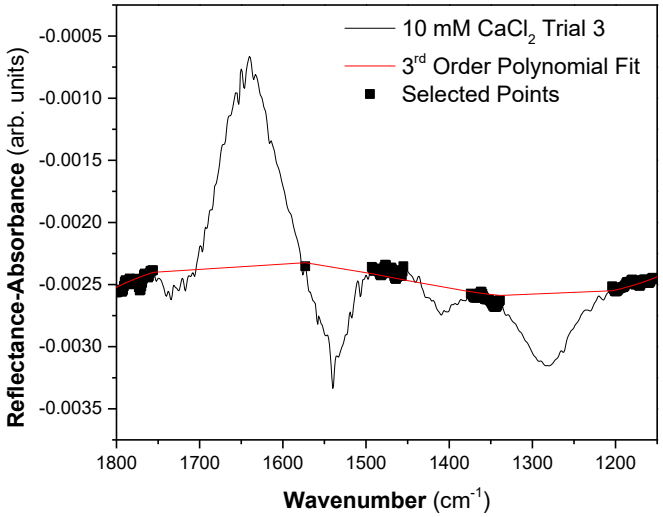

Figure C.1. Fit of a third-order polynomial to select data points to form a baseline in the carboxylic acid headgroup region of a d_{31}-PA monolayer on a 10 mM $CaCl_2$ subphase.

In Section 5.3.1, the intensities and the center frequencies of the C=O, and CO_2^- modes were determined to d_{31}-PA monolayers on $CaCl_2$ subphases. These values were determined by fitting the modes to individual Gaussian curves, as shown in Fig. C.2. The water bending mode was removed from the data as to not obscure the fits.

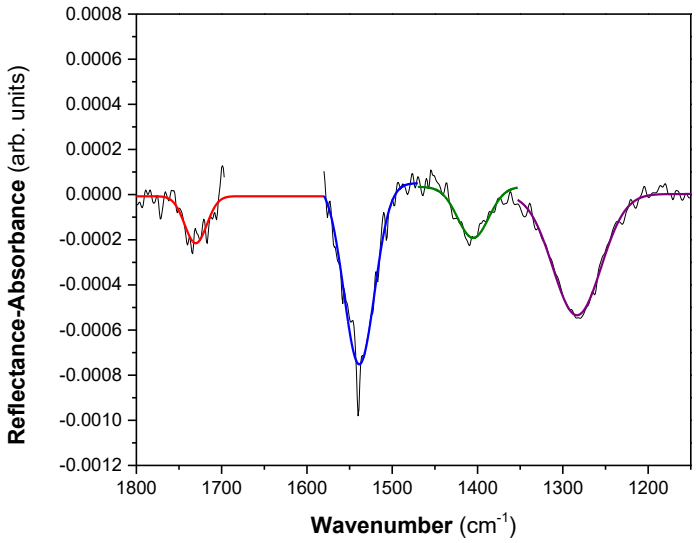

Figure C.2. Gaussian fits of the various modes in the headgroup region of a d_{31}-PA monolayer on a 10 mM $CaCl_2$ subphase.

C.2. Control Experiments

To rule out the possibility that ion-driven deprotonation of d_{31}-PA was caused by trace metal contaminants in the salt solutions, control experiments with EDTA were conducted. Two solutions were prepared, with and without 10 μM EDTA, at the same pH. EDTA is acidic and decreases the pH of the aqueous solution. Spectra are collected of monolayers spread on each subphase and are compared to see if any differences are

observed. In our experiments with $CaCl_2$ subphases, no changes are observed in the spectra, so the aqueous $CaCl_2$ solutions were deemed free of trace metal contamination.

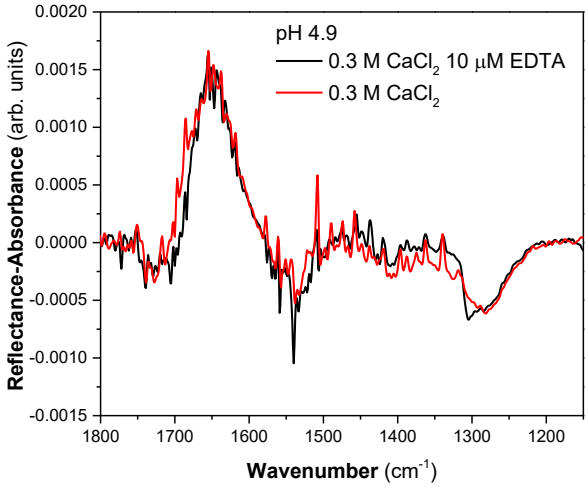

Figure C.3. Control of EDTA-doped $CaCl_2$ subphases to test for trace metal contamination. No changes are observed in the spectra of d_{31}-PA monolayers spread to 20.5 $Å^2$/molecule, so the solution is deemed free of trace metals.

Another control test was conducted for IRRAS, VSFG, and surface potential measurements that were performed in Petri dishes. In these systems, monolayers are spread to a target MMA, but surface pressure is not maintained through mechanical means (i.e. Langmuir trough barriers). Because monolayer compression in an isotherm is a metastable process,[35] the surface pressure measured at a particular MMA in an isotherm may not compare to the surface pressure exerted by a spread monolayer on a Petri dish. To determine the surface pressure associated with the systems measured in Petri dishes, surface pressure was measured for spread monolayers in Petri dishes to 1) ensure monolayers are present, 2) test the surface pressure stability with time, and 3) approximate the phase of the monolayer under the spread MMA conditions.

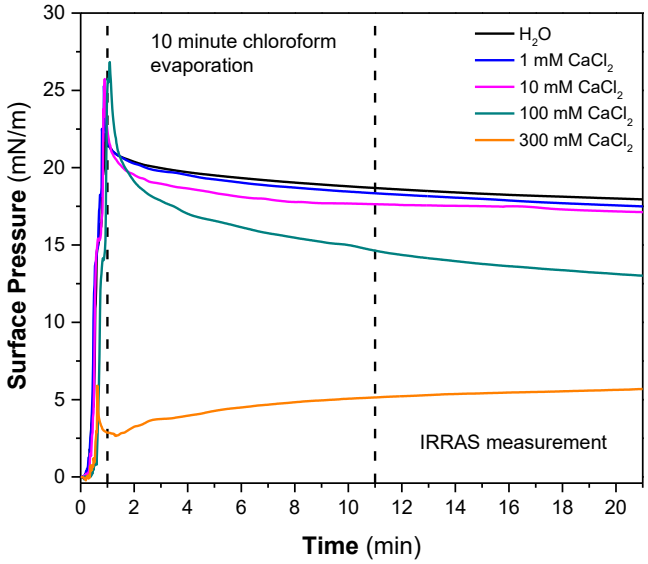

Figure C.4. Measure of surface pressure in d_{31}-PA monolayer systems spread to a mean molecular area of 20.5 $Å^2$/molecule on various $CaCl_2$ subphases. In all systems, surface pressure remains fairly stable after chloroform evaporation, and have measured surface pressures which differ from the surface pressure in an isotherm.

Appendix D: Solubility of DPPA in Various Solvents Reported in the Literature

There is an assortment of solvents reported in the literature for dissolving diplamitoyl phosphatidic acid (DPPA) as a lipid spreading solution. In order to determine the best solvent and supplier of DPPA (Avanti Polar Lipids or Sigma), visual tests on solubility were conducted. DPPA solutions were created to attempt to recreate those described in the table below. If a mixed solvent ratio (volume:volume) was reported, it is reflected in the table.

Table D.1. Literature summary of DPPA solutions for monolayer studies. The abbreviation "NR" is used when that information is not reported in the paper. (Ch: chloroform, Me: methanol, Et: ethanol)

Company	Solvent	Concentration	Reference
Avanti Polar Lipids	9:1 Ch:Me	0.5 mg/mL	Lee, 2006[189]
Avanti Polar Lipids	9:1 Ch: Me	0.5 mg/mL	Lee, 2007[175]
Avanti Polar Lipids	NR Ch: Me	1 mM	Chen, 2010[118]
Avanti Polar Lipids	Ch, Me	NR	Salay, 2012[190]
Avanti Polar Lipids	Ch, Me	NR	Rudolphi-Skorska, 2014[191]
Sigma Aldrich	Ch	1.0 mg/mL	Luckham, 1992[192]
Sigma Aldrich	Ch	1.0 mM	Zaitsev, 1995[193]
Sigma Aldrich	4:1 Ch:Me	NR	Kim, 1996[194]
Sigma Aldrich	4:1 Ch:Et	0.46 mg/mL	Minones, 2002[195]

Sigma Aldrich	Ch	NR	Estrela-Lopis, 2004[196]
Sigma Aldrich	NR	1.0 mM	Risovic, 2012[197]

DPPA solutions were prepared by measuring out a mass of solid DPPA into a 10 mL volumetric flask on an analytical balance (Denver Instruments, SI-224). The solvents used to test the solubility of DPPA provided by Avanti Polar Lipids were 9:1 Ch:Me, 4:1 Ch:Me, 4:1 Ch:Et, and 1:1 Ch:Me. The visual results from these tests are shown in Fig. D.1. DPPA was not soluble in the 9:1 Ch:Me and 4:1 Ch:Et solvents, and formed a cloudy, gel-like solution. The 4:1 Ch:Me and 1:1 Ch:Me solvents proved to be more appropriate. DPPA was mostly dissolved in these solvents, although some solid appeared to collect at the bottom of the vial.

Figure D.1. DPPA (Avanti Polar Lipids) solutions in various solvents. From left to right: 0.0068 g DPPA in 9:1 Ch:Me; 0.0066 g DPPA in 4:1 Ch:Et; 0.0053 g DPPA in 4:1 Ch:Me; 0.0029 g DPPA in 1:1 Ch:Me.

DPPA purchased from Sigma was tested in chloroform and 4:1 Ch:Me solvents. Solutions made with these solvents are shown in Fig. D.2. DPPA was insoluble in chloroform, and residue remained in the volumetric flask as well as in the vial after transfer of the solution. DPPA was fully dissolved in 4:1 Ch:Me after approximately 30 seconds of

sonication in the volumetric flask. No solid DPPA could be seen by eye in either the volumetric flask or the vial after transfer. From these tests, it was determined that DPPA, purchased from Sigma, in 4:1 Ch:Me was the most appropriate solution.

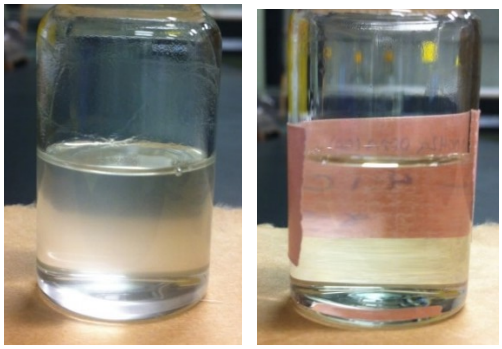

Figure D.2. DPPA (Sigma) in chloroform (left, 0.0042 g DPPA) and 4:1 Ch:Me (right, 0.0041 g DPPA).

It is important to note that DPPA purchased from Sigma does not come as a monosodium salt, therefore the concentration of DPPA is dependent on the sodium content, which varies between batches and is listed in the certificate of analysis. The calculation for molecular weight is the free acid weight divided by the decimal equivalent of 1 minus the sodium content.

$$MW_{DPPA} = \frac{648.9\ g/mol}{1 - 0.XXX} \tag{D.1}$$

Appendix E: Permissions

Chapter 3 was reproduced in part with permission from the PCCP Owner Societies: B. A. Wellen, E. A. Lach, and H. C. Allen "Surface pK_a of octanoic, nonanoic, and decanoic fatty acids at the air-water interface: Applications to atmospheric aerosol chemistry" *Phys. Chem. Chem. Phys.*, 2017, 19, 26551-26558.

Chapter 4 was reproduced in part with permission from the PCCP Owner Societies: E. M. Adams, B. A. Wellen, R. Thiraux, S. K. Reddy, A. S. Vidalis, F. Paesani, H. C. Allen "Sodium–carboxylate contact ion pair formation induces stabilization of palmitic acid monolayers at high pH" *Phys. Chem. Chem. Phys.,* 2017, 19, 10481-10490.

Chapter 5 was reproduced in part with permission from the PCCP Owner Societies: B. A. Wellen Rudd, A. S. Vidalis, and H. C. Allen "Thermodynamic versus Non-Equilibrium Stability of Palmitic Acid Monolayers in Calcium-Enriched Sea Spray Aerosol Proxy Systems" *Phys. Chem. Chem. Phys.,* 2018, DOI: 10.1039/C8CP01188E.